Title

Node-Pore Sensing: A Robust, High Dynamic Range Method for Multi-Parametric Screening of Biological Samples

Author

Balakrishnan, Karthik Ratna

Publication Date

2014

Node-Pore Sensing: A Robust, High Dynamic Range Method for Multi-Parametric Screening of Biological Samples

By

Karthik Ratna Balakrishnan

A dissertation submitted in partial satisfaction of the

requirements for the degree of

Doctor of Philosophy

in

Engineering – Mechanical Engineering

in the

Graduate Division

of the

University of California, Berkeley

A Dissertation Submitted for Partial Satisfaction

Committee in charge:

Professor Lydia L. Sohn, Chair

Professor Amy E. Herr

Professor Dorian Liepmann

Fall 2014

Node-Pore Sensing: A Robust, High Dynamic Range Method for Multi-Parametric Screening of Biological Samples

By

Karthik Ratna Balakrishnan

Abstract

Node-Pore Sensing: A Robust, High Dynamic Range Method for Multi-Parametric Screening of Biological Samples

by

Karthik Ratna Balakrishnan

Doctor of Philosophy in Engineering - Mechanical Engineering

University of California, Berkeley
Professor Lydia L. Sohn, Chair

Resistive-pulse sensing is a technique that allows for measurements of particles in a solution. The underlying principle relies on measuring the electrical resistance across a small pore connecting two reservoirs filled with fluid. As an insulating particle enters the pore, the particle displaces the conducting fluid, leading to an increase in the resistance measured. Pulse magnitude and width reveal information about the particle in transit. The size of the pulse magnitude corresponds to the size of the particle, while the width of the pulse represents the length of time the particle takes to transit the pore.

We show that resistive pulse sensing can be used in combination with protein functionalization to achieve surface marker screening of small sample sizes. We analyze single satellite cells from muscle fibers of mice. We also present unique channel geometries that offer advancements to traditional resistive-pulse sensing. This new technique, node-pore sensing, provides unique signal detection benefits and essentially provides particle tracking, allowing us to determine specifically when a particle transits a specific region of a pore. Ultimately, node-pore sensing provides unprecedented sensitivity, which we show can be used to detect human immunodeficiency virus in human plasma. The particle tracking aspect of this technique affords us the capability of probing particle interactions in different regions of the pore, ultimately allowing us to perform single-cell screening of multiple biomarkers in a single device. We demonstrate multi-marker screening on cultured leukemia cells and bone marrow from leukemia patients. These studies showcase the promise of our platform for broad screening and diagnostic applications.

Contents

List of Figures

List of Tables

Acknowledgments

I would like to thank the numerous people who have contributed toward this thesis, in the form of advice, assistance, support, and friendship over the years.

I dedicate this thesis to my family for their encouraging words, and my parents for providing a constant source of inspiration and support throughout my whole life.

In particular, I would like to thank Matthew Chapman, Jeremy Whang, Trong Nguyen, Richard Hwang, Jimmy Hack, Anand Kesavaraju, Eugene Chao, George Anwar, Ju Li, Haiyan Huang, and Eric Jabart for the incredible work and support they have contributed.

I must thank my advisor, Lydia Sohn, for her constant mentoring, guidance, support, and care throughout each of the last several years – her dedication has been truly inspirational.

Lastly, I really appreciate all of the friends I've made throughout this journey that have been with me through the good times and the bad.

CHAPTER 1

Introduction

In this thesis, we outline the work we have done to advance the capabilities of microfluidic resistive-pulse sensing (RPS), a label-free method for detecting and screening biological samples. RPS, or the Coulter-counter technique [1] of particle sizing, has long been used to determine the size of particles. Given its simplicity, this technique has been extensively used in cell biology and medicine as the use of RPS enables accurate cell-size distributions [2-6], the measurement of cellular response to stimuli [7, 8], and the ability to detect viruses [9-11].

Particle sizing with RPS involves measuring the current or resistance across a pore that is connected to two reservoirs (Fig. 1.1). As an insulating or dielectric particle traverses a pore, the particle partially blocks the flow of current across the pore, leading to a temporary decrease in the measured current [2-11] . Fig. 1.1 shows the top and side view of a typical RPS device. Particles (red) enter the device through the inlet via pressure-driven flow (electrophoretic flow can also be used), at which point the current remains at a baseline value as in Fig. 1.1B. As shown in Fig. 1.1C, when the particle enters the pore, a drop in the overall current is recorded. Once the particle exits the pore (Fig. 1.1D), the current across the pore returns to the baseline value. Thus, a current pulse, corresponding to a particle transiting the pore, is produced and measured.

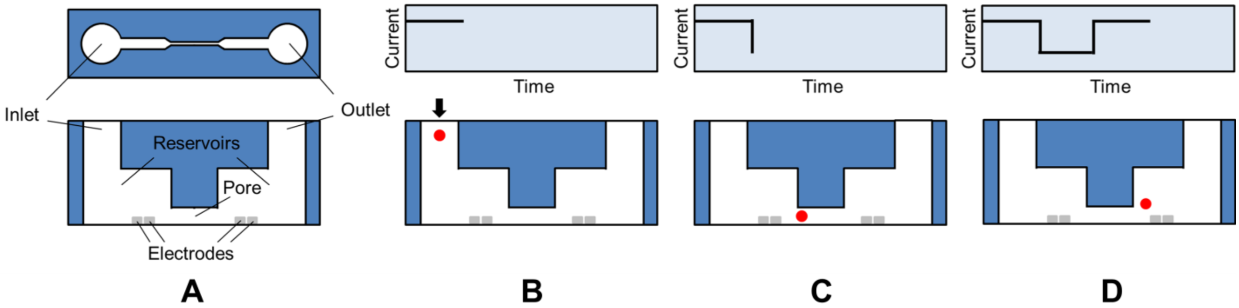

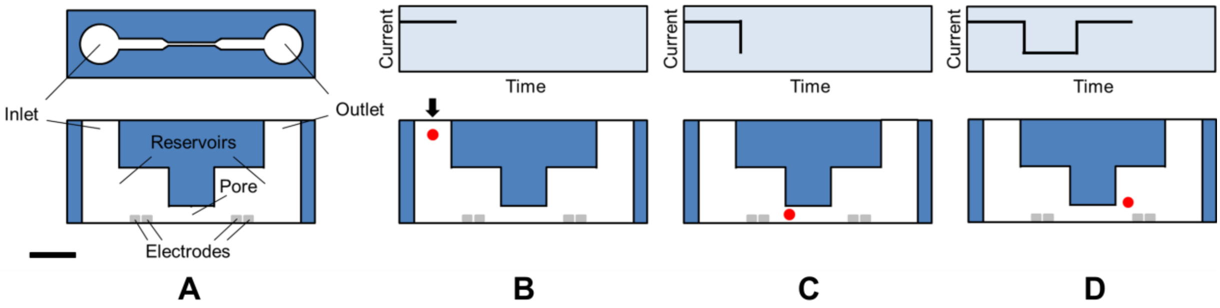

Fig. 1.1: Resistive-pulse sensor schematic. (A) Top view (top) and side view (bottom) of the RPS device. (B) Particles enter through the inlet of the device, at which point the current remains at the baseline value. (C) As a particle enters the pore, it causes a drop in the current measured across the pore. (D) After the particle exits the pore, the current returns to the baseline value. Scale bar (black) corresponds to sizes of RPS sensors highlighted in this thesis (e.g. 800 µm).

The current pulse caused by a particle transiting the pore provides multi-parametric information. For example, the magnitude of the current pulse relates to the size of a particle in transit, and the width of the current pulse indicates the transit time of the particle across the pore. Finally, the frequency at which pulses occur is related to the particle concentration in the measured sample.

This thesis describes the major advances we have made to traditional RPS devices. Using simple design changes to the pore geometry, we are capable of greatly enhancing the capabilities of pore sensing. Specifically, we have created segmented pores, hereafter referred to as node-pores, that offer multiple advantages to basic RPS. Node-pores produce unique electronic signatures that offer benefits in terms of signal processing and sample detection. These pores also allow one to determine when a particle transits a particular part of the node-pore, which provides benefits for probing different particle-pore interactions within a single measurement.

In Chapter 2, I discuss RPS theory as it applies to traditional pores and node-pores. In Chapter 3, I outline the device fabrication techniques and platform design that we have developed for effective and efficient sample testing. In Chapter 4, I detail our work to screen mouse muscle satellite stem cells for cell-surface marker expression and heterogeneity. In Chapter 5, I explain our efforts to advance traditional RPS using node-pores, and in Chapter 6 and 7, I illustrate specific NPS applications. Finally, in Chapter 8, I summarize this thesis work and suggest future directions of research.

Chapter 2

Theoretical Considerations

In this chapter, I detail the theory of RPS using traditional pores and node-pores. I analyze the resistance change caused when a particle enters a pore. I also discuss the fluid flow regime at which the RPS and NPS measurements in this thesis were performed. Furthermore, I describe the particle-pore interactions that result in transit-time differences and introduce the effects of unique node-pore geometries, demonstrating how these novel pores change the fluid flow and the current pulses generated as particles transit through.

2. 1 Resistive-Pulse Sensing Parameters

2.1.1 Resistance increase and particle sizing

To understand the particle sizing aspect of RPS, we analyze the resistance change caused by an insulating particle transiting a pore. The resistance measured across a pore increases by δR_{pore} when a particle enters the pore and displaces an equivalent volume of fluid of resistivity ρ, as shown in Fig. 2.1. The resistance of the pore, R_{pore}, is given by

$$R_{\text{pore}} = \rho \int \frac{dz}{A_{\text{conducting}}(z)} \tag{2.1}$$

where $A_{\text{conducting}}(z)$, the cross-sectional area of conducting fluid, is equal to $A_{\text{pore}}(z)$, the cross-sectional area of the pore along the pore axis, z, when no particle is present [11]. The increase in resistance as a particle enters the pore is

$$\delta R_{\text{pore}} = \rho \int \frac{dz}{A_{\text{pore}}(z) - A_{\text{particle}}(z)} - \rho \int \frac{dz}{A_{\text{pore}}(z)} \tag{2.2}$$

where $A_{\text{particle}}(z)$ is the cross-sectional area of the particle along the pore axis. The particle size can thus be calculated using $\delta R_{pore} / R_{pore}$. Because R_{pore} is the dominant resistance in our measurements, relative changes in the current magnitude are approximately equal to relative resistance changes, i.e. $|\Delta I/I| \sim |\Delta R/R|$.

Gregg and Steidley defined $R_{\text{pore}} = 4\rho L/\pi D^2$ in the limit of the particle size being comparable to that of the pore diameter, D. Here L is the length of the pore, and

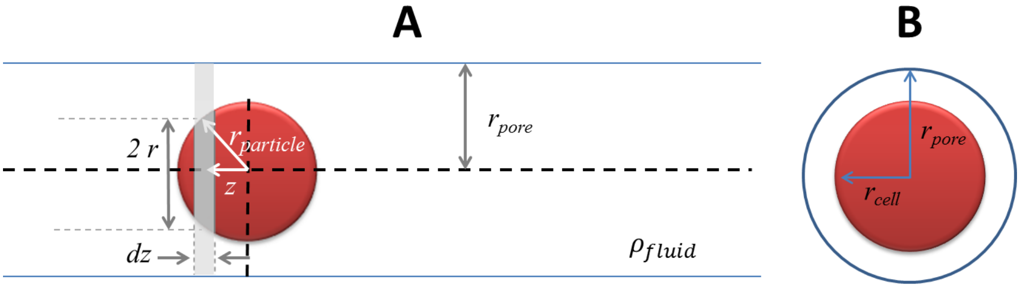

Fig. 2.1: Particle in a pore schematic. A spherical, non-conducting particle (red) with radius, r_{particle}, centered in a pore with radius, r_{pore}. dx and r correspond to the thickness and radius of a cross-sectional slice where z is along the flow direction axis.

When a spherical particle enters the pore, the volume of the pore containing conducting fluid has different values in a given cross-sectional slice depending on whether or not the particle occupies that slice. The cross-sectional area without the particle is $A_{\mathrm{conducting}}(z) = \pi D^2/4$ and the cross-sectional area with the particle is $A_{\mathrm{conducting}}(z) = \frac{\pi}{4}(D^2-d^2+4z^2)$, where D is the diameter of the pore, d is the diameter of the particle, and z is taken along the flow direction axis as shown in Fig. 2.1. Evaluating Eq. 2.1 across the length of the pore, L, results in the following in the limit where $d \sim D$,

$$\delta R_{pore}/R_{pore} = \frac{D}{L}\left[\frac{\arcsin\left(\frac{d}{D}\right)}{\left(1-\left(\frac{d}{D}\right)^2\right)^{\frac{1}{2}}} - \frac{d}{D}\right] \tag{2.3}$$

Deblois and Bean [11] developed a relationship (Eq. 2.4) using a different approach. They considered an insulating sphere in a uniform electric field, which they then applied a solution of Laplace's equation that satisfies the boundary condition that the field normal to the insulating sphere is nonexistent at the surface, as shown in Fig. 2.2. The current streamlines bulge out around the sphere.

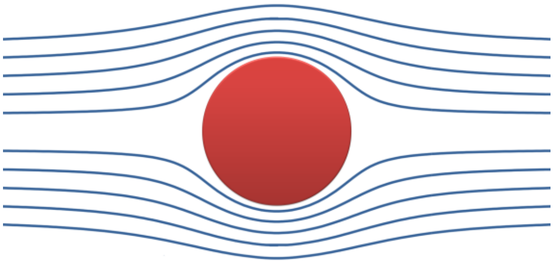

Fig. 2.2: Current streamlines around a sphere. The current streamlines (blue) bulge around the sphere (red).

Using this approach, Deblois and Bean obtained the following in the limit of $d << D$,

$$\delta R_{pore}/R_{pore} = \frac{d^3}{D^2 L}\left[\frac{D^2}{2L^2} + \frac{1}{\sqrt{1+\left(\frac{D}{L}\right)^2}}\right] F\left(\frac{d^3}{D^3}\right) \tag{2.4}$$

Here, $F(x)$ is a numerical correction factor based on values determined experimentally by Deblois and Bean and fit by Saleh [13],

$$F(x)=1+1.265x+1.347x^2+0.648x^3+4.167x^4 \tag{2.5}$$

The two solutions described above (Eqs. 2.3 and 2.4) address the change in resistance across the pore in the small and large particle-to-pore ratio limits. Deblois et al. then derived a single equation [14] to describe the full range of particle sizes based on the experimental work of Smythe [15, 16],

$$\delta R_{pore}/R_{pore} = \frac{d^3}{D^2 L}\left[\frac{1}{1-0.8\,(d/D)^3}\right] \tag{2.6}$$

Thus, the size of the particle can be determined using the normalized resistance change caused by that particle transiting the pore, as shown in Fig. 2.3.

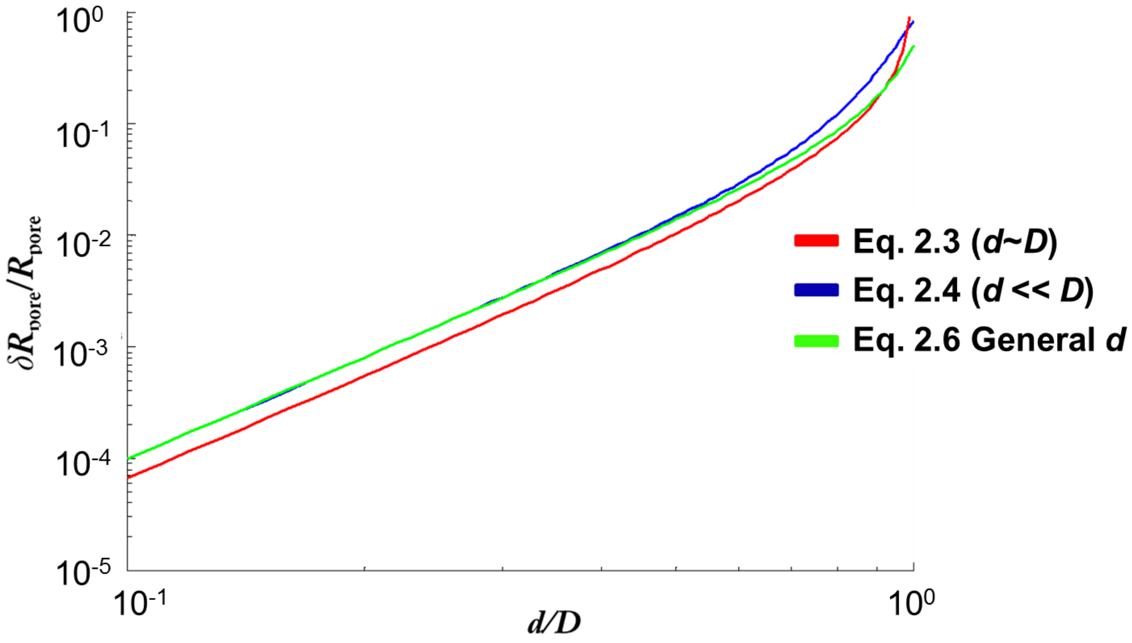

Fig. 2.3: Normalized resistance changes for different particle-to-pore ratios. Equation 2.6 is applicable for the full range of particle-to-pore sizes, fitting closely to Equation 2.3 when d~D and closely to Equation 2.4 when $d << D$.

2.1.2 Fluid flow through a pore

The current pulses measured with RPS indicate not only particle size, but also the length of time for a particle to transit the pore. We use pressure-driven flow to drive particles through our RPS devices. As a particle transits the pore, the force applied to the particle is balanced with the drag force retarding motion through the fluid.

To understand the transit time of a particle fully, we determine the Reynolds number, $Re=\rho UL/\mu$, where ρ is the density of the fluid, U is the velocity, L is the characteristic length scale, and μ is the dynamic viscosity. The Reynolds number, *Re*, is the ratio of inertial to viscous forces. In microfluidic systems such as ours, the channel dimensions are small (e.g. 18 µm x 18 µm, W x H), and $Re < 1$, indicating that the flow is laminar. This low *Re* has implications on the time the flow takes to stabilize in our pores and determines whether we need to take into account of "entrance effects", i.e. how the particle enters the pore. The entrance length parameter allows us to determine how far into the pore the flow develops into its stable velocity profile. For a pipe of diameter *D*, the dimensionless entrance length parameter is proportional to diameter and *Re* [13]. Therefore, at the extremely low Reynolds numbers that exist for our system, the flow stabilizes almost immediately after entering our pore, and we can ignore entrance effects on particle velocity. In other words, the flow takes on a parabolic shape almost immediately after entering the pore (Fig. 2.4).

The low Reynold's number regime also simplifies our analysis of the Navier-Stokes equation to describe the flow involved in our RPS measurements. The Navier-Stokes equation is given by

$$\rho\left[\frac{\partial \boldsymbol{U}}{\partial t}+(\boldsymbol{U}\cdot\nabla)\boldsymbol{U}\right]=-\nabla p+\mu\nabla^2\boldsymbol{U}+\mathbf{f} \tag{2.7}$$

Where ρ is the fluid density, p is the pressure, $\boldsymbol{U}$ is the fluid velocity, t is time, μ is the fluid viscosity, and $\mathbf{f}$ is the body forces per unit volume. The Reynolds number of our system allows us to neglect inertial forces, and thus we arrive at the simplified version of the equation:

$$\nabla p=\mu\nabla^2\boldsymbol{U} \tag{2.8}$$

Another specification of our system is given by the continuity equation,

$$\nabla\cdot\boldsymbol{U}=0 \tag{2.9}$$

The flow is of parabolic profile shape, as shown in Fig. 2.4.

As this parabolic fluid flow drives a particle through a pore, the force applied to the particle is balanced by the drag force that retards the motion of the particle through the fluid. According to Stokes law, the drag force experienced by a particle is given by

$$F_{\mathrm{drag}}=6\,\pi\,\mu\,(d/2)\,u_{\mathrm{particle}} \tag{2.10}$$

Where u_{particle} is the velocity of the particle. In this thesis, the flow conditions (e.g. a 15 µm cell transiting a channel filled with phosphate buffered saline at 1500 µm/s), result in minor drag forces on the cells, $F_{\mathrm{drag}} < 1$ pN. As we show in the next section, protein patterning in our device results in another force that retards the motion of cells interacting with these proteins.

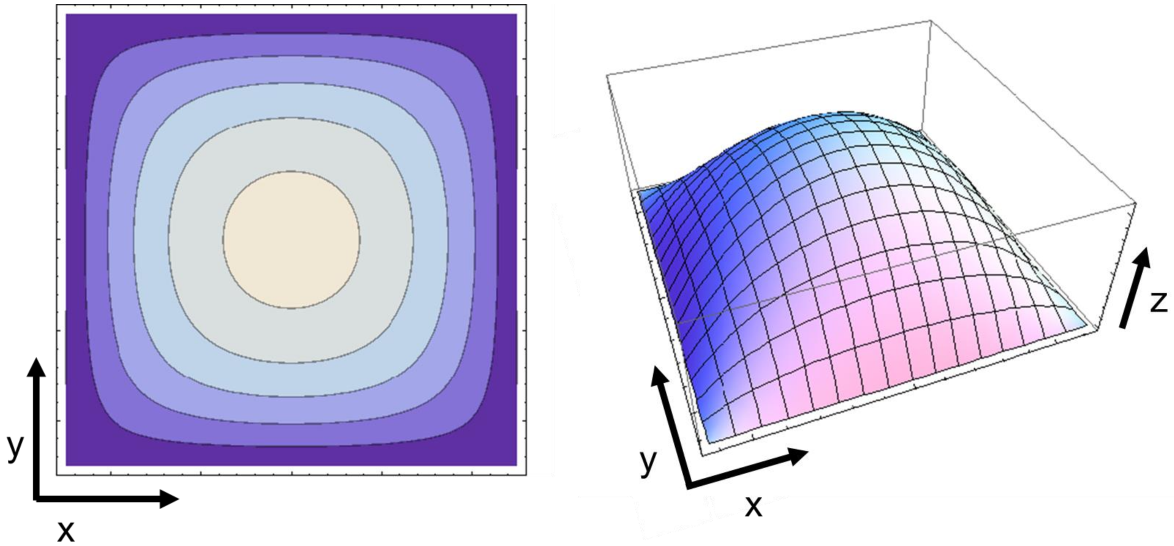

Fig. 2.4: The parabolic flow profile shape in our microfluidic pores is shown in the schematics. The flow is at maximum velocity at the center of the pore (white) and at its lowest values near the wall (purple).

2.1.3 Particle-pore interactions

While pores have been used extensively for detecting, sizing, and counting particles, chemically modification of pores was introduced [17, 18] to enhance the capabilities of RPS sensing. Recent work demonstrated that interactions in a pore due to pore functionalization with metal, oxide, or organic coatings can result in slower translocation rates, thereby realizing "smart-pore" sensors that could provide insight into the properties of the particles that are transiting the pore. Similarly, by employing chemically functionalized pores, we and others have demonstrated that RPS could provide sensitive, label-free method for characterizing surface-marker expression on individual cells [18]. In this particular case, the functionalization can result in specific interactions between cell surface-markers and the functionalized surface. These interactions result in additional forces against the motion of cells through the fluid, resulting in cells taking a longer time to travel through the pore. Therefore, the width of the detected current pulse is larger than if there was no pore functionalization (a blank pore). Thus, RPS can be used to determine the expression of particular surface-markers on cells.

To accomplish surface-marker screening with RPS, the pore is functionalized with antibody and specific interactions between the cell-surface receptors and the proteins in the pore retard the cell motion, as shown in Fig. 2.5. Depending on the fluid-flow velocity and the effective binding interaction strength, cells engage in free motion, rolling adhesion, or firm adhesion to functionalized surfaces, as demonstrated in other devices designed for cell capture [19-21]. Using their 100 µm X 1 mm X 30 mm (H x W x L) single microchannel device for cell capture, Zheng et al. measured these regimes as <1.3 µl/min (firm adhesion), 1.3-2.8 µl/min (rolling adhesion), and >2.9 µl/min (free motion) within their device. For RPS, the interactions between cells and the functionalized proteins result in formation of transient ligand-receptor interactions (rolling adhesion), as described by Myung et al [22]. In rolling adhesion, although the interaction between the cell and the functionalized substrate is still significant, the adhesion force between the two does not overcome the hydrodynamic force. Consequently, instead of cells being captured onto the substrate, cells undergo rolling adhesive interaction where new bonds are continuously formed as the cell moves along the pore and old bonds dissociate; the density of receptors on the surface of the cell influences the number of interactions that take place.

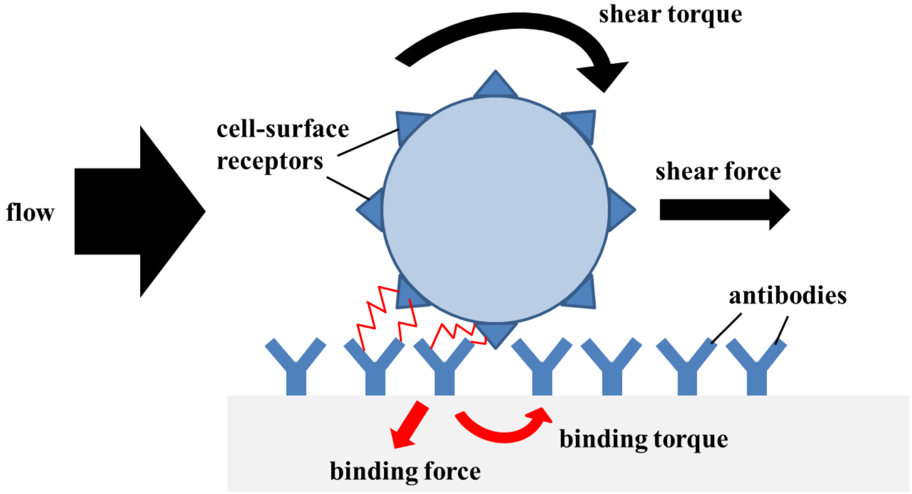

Fig. 2.5: Schematic of cell binding with antibodies functionalized on the device substrate. Cell-surface receptors bind with the antibodies, resulting in forces retarding the cell motion through the fluid.

Hammer and Lauffenburger [23] explained that the adhesion dynamics depend on the fluid mechanical forces acting on the cell, the density of ligand molecules, the number of cell surface receptors, the speed at which the receptors bind with ligands, the affinity of receptors for the ligand, and the mobility of receptors. They derived an estimate for the force per receptor-ligand interaction based on the total force acting on the bonds, F_t, the bond density, N_b, and the radius of the "contact area" , a, between the cell and the functionalized surface,

$$F_b = \frac{F_t}{\pi a^2 N_b} \tag{2.11}$$

To calculate this force, Hammer and Lauffenburger assumed that the adhesive bonds counter the force of torque that the passing fluid applies to the cell. The action of the bonds balances the translational force due to shear, imparting a torque on the cell. Thus, there are two additive torques that the bonds must resist – one from the passing fluid and one from the bonding force. Using the forces and torques acting on the cell in a viscous shear field, they estimated the total force as

$$F_{\mathrm{t}}=\frac{3}{2}\pi\mu d^2 SR\sqrt{\left(1+\frac{2S}{d}\right)^2 F^{\mathrm{s}^2}\left(1+\frac{9d^2\pi^2}{64a^2}\right)^2+\left(1+\frac{2S}{d}\right)F^{\mathrm{s}}\tau^{\mathrm{s}}\frac{3\pi^2 d^2}{16a^2}+\frac{\pi^2 d^2}{128a^2}\tau^{\mathrm{s}^2}} \tag{2.12}$$

where *SR* is the shear rate, *S* is the separation distance, τ denotes torque, F_{t} denotes force, and the superscript s denotes shear, *d* is the diameter of the cell.

These bond forces result in cell-antibody interactions slowing down cells that express surface markers that transiently bind with the proteins in the pore. A cell's transit time through a functionalized pore (Fig. 2.6B and C) would be greater than that through a blank or unfunctionalized pore (Fig. 2.6A). Further, if the interactions between a cell and the functionalized proteins result in specific interactions due to complementary antibody-antigen binding (Fig. 2.6C), the cell would have a significantly longer transit time than if the interactions were non-specific (Fig. 2.6B).

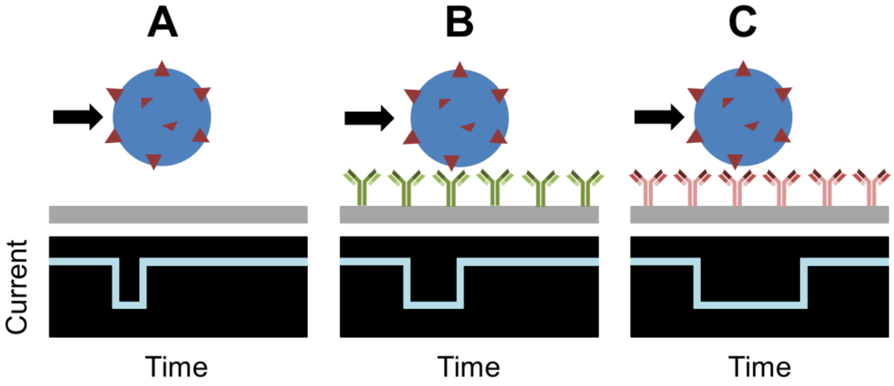

Fig. 2.6: Cell interactions in a pore. (A) A cell travelling through a blank pore does not experience significant retarding forces. (B) A pore functionalized with antibodies that exhibit nonspecific interactions with cell-surface receptors leads to a slightly longer transit time. (C) A pore functionalized with antibodies that exhibit specific interactions with cell-surface receptors leads to a significantly longer transit time.

Using previous work by Cozens-Roberts et al. [24], the estimated antibody density on the functionalized surface can be determined. Assuming only 70% of the antibodies actually bind to the surface, the resulting expression in terms of antibody concentration, [*Ab*], volume of the functionalized region, V, Avogadro's number, N_A, the area of the substrate, A, and the molecular weight of the antibody, M, is given by

$$C = \frac{0.7\,[Ab]\,V\,N_\mathrm{A}}{(A\,M)} \tag{2.13}$$

Using this, we can estimate the antibody density on our substrates. For the testing in this thesis (e.g. Sca-1 antibody for stem cell testing in Chapter 4), the antibody densities are ~1 x 10^5 Ab μm^{-2}.

2.1.4 Variable pore geometries

While greatly enhancing its utility, functionalizing a pore with only one type of species limits the broader applicability of pores for biosensing. We have addressed this limitation by developing a variable cross-section pore that creates unique electronic signatures for reliable detection and data analysis. By using common lithography techniques to define a single pore into separate sections (Fig. 2.7), we are able to use RPS to determine precisely when a cell passes through a given pore segment. Overall, variable cross-section pores offer specific advantages: 1) the ability to functionalize each portion of the pore specifically with a different antibody that corresponds to different cell-surface receptors, which in turn enables label-free multi-marker detection in a single run; and 2) a unique electronic signature that allows for both an additional level of precision to testing. These pores consist of a sequence of nodes of larger area than the rest of the pore (Fig. 2.7), and hence we refer to them as node-pores. As particles transit through node-pores, the variable cross-sectional design results in current signals that are segmented based on node placement. The unique measurement signals that node-pores generate can be understood by analyzing the resistivity changes as a particle transits through a node-pore sensor.

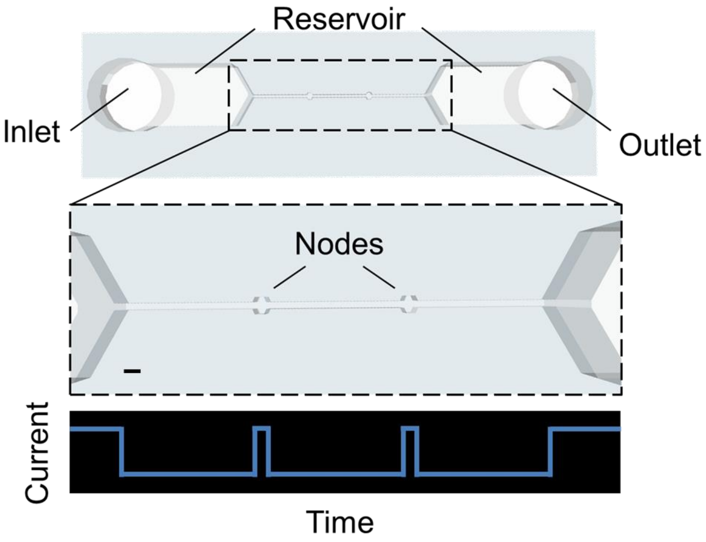

Fig. 2.7: Node-pore schematic. Diagram showing the segmented design of node-pores and the electrical current from a particle transiting through the node-pore shown. The node-pore

shown contains two nodes, as shown in the inset. The current measurement shape reflects the geometry of the node-pore. Scale bar is 100 μm.

To understand the resistance change caused by a particle transiting the node-pore, we again analyze a non-conducting particle and a pore with radius r_{particle} and r_{pore}, respectively. The resistance, dR, of a cross-sectional slice of thickness dx is [1]

$$dR = \frac{\rho dx}{\Delta A} \tag{2.14}$$

where ρ is the fluid resistivity and ΔA is the difference between the pore cross-sectional area, A_{pore}, and the particle cross-sectional area, A_{particle} (Fig. 2.8A and B). We can express the total increase in resistance measured across the pore due to the presence of a particle as

$$R = \int_{-r_{\text{particle}}}^{r_{\text{particle}}} \frac{\rho dx}{\Delta A(x)} - \int_{-r_{\text{particle}}}^{r_{\text{particle}}} \frac{\rho dx}{A_{\text{pore}}(x)} \tag{2.15}$$

where x is the flow direction axis. The above analysis assumes a cylindrical pore; however, the planar lithography process we employ (discussed in the next chapter) results in rectangular cross-sections with width, W, and height, H. Thus, the cross-sectional area difference of a node-pore slice is

$$\Delta A_{\text{rectangular}}(x) = WH - r(x)^2 \tag{2.16}$$

where $r(x)$ is the particle slice radius (Fig. 2.8C). In a node region of the pore, the increased cross-sectional area difference of a pore slice is

$$\Delta A_{\text{node}}(x) = W_{\text{node}}H - r(x)^2 \tag{2.17}$$

where W_{node} is the width of the node region (Fig. 2.8D). Thus, when a particle transits a node region with width $W_{\text{node}} > W$, ΔA is larger than that in the constant cross-section region, and in turn, the change in resistance, ΔR, drops while the particle is within the node. Ultimately, if a pore has a constant cross-sectional area, the measured change in resistance caused by the particle transiting the pore is constant (Eq. 2.15). If the cross-sectional area of the pore changes, then the resistance will also change as the particle transits the pore. Since the resistance depends on r of each cross-sectional slice of width dx (at any given time), we can specifically tailor the shape of the pore to provide a desired resistance value (and thus current) measurement.

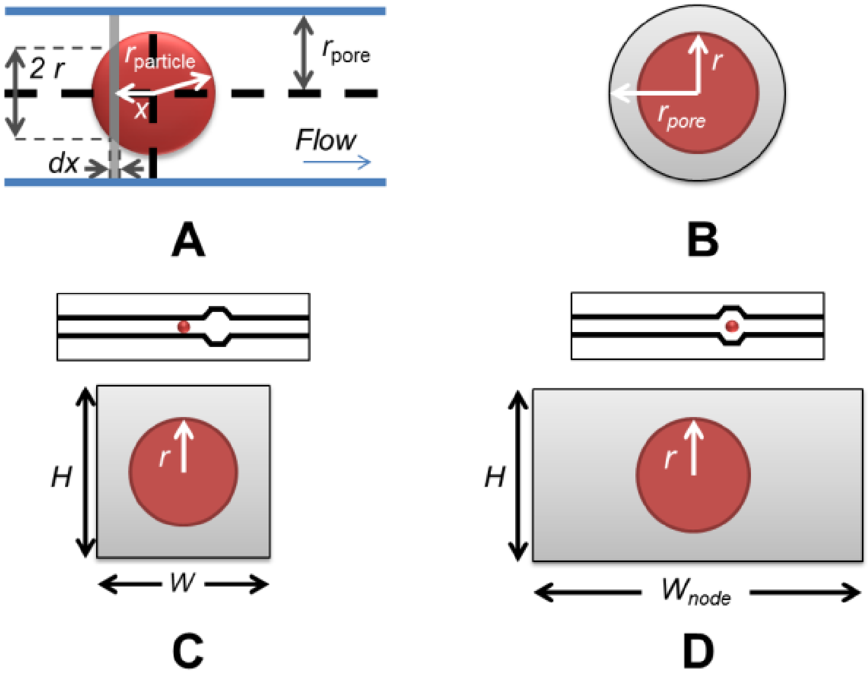

Fig. 2.8: NPS theory. (A) Schematic showing a spherical, non-conducting particle (red) with radius, r_{particle}, centered in a pore with radius, r_{pore}. dx and r correspond to the thickness and radius of a cross-sectional slice where x is the flow direction axis. (B) View of a cross-sectional slice of the entire pore. Red and gray represent the particle cross-section and the cross-sectional area between the pore and the particle, respectively. (C) Cross-sectional slice of a particle within a rectangular pore of height H and width W. (D) Cross-sectional slice of a particle within a rectangular node region of height H and width $W_{node} > W$.

With MATLAB, we modeled different node-pore geometries to show how node-pore design can be used to create different current pulse measurements. Specifically, we analyzed resistive slices across the node-pore when a transiting insulating particle was at a specific position along the node-pore. The simulation analyzed the resistance of each one-micron thick cross-sectional slice along the node-pore (no conductance in the volume occupied by the particle). At any given time when the particle is in a given location, the resistive slices are added together to obtain the overall resistance calculation. These values are compared to the resistance of the node-pore when there is no particle present. The resulting normalized resistance value is plotted. Fig. 2.10 shows the normalized resistance pulses produced when a 15-µm particle transits four node-pores of different geometries but of all the same overall length. As shown, the nodes were created using a gradual increase and decrease in pore area instead of immediate cross-sectional changes (perpendicular) to better simulate fabrication conditions. As shown, the node-pore architecture heavily influences the electrical measurements generated across the node-pore as a particle transits. In the pore with no nodes, the normalized resistance increases as the particle enters, and remains at a constant value until the particle exits the pore, where the value returns to its baseline level. As the particle enters the pores with nodes, the resistance measured increases, as expected. When the particle enters a node, however, the normalized resistance drops, only to rise again once the particle exits the node. This rise and fall in resistance occurs for all nodes. Finally, when the particle exits the node-pore, the normalized resistance returns to the baseline value.

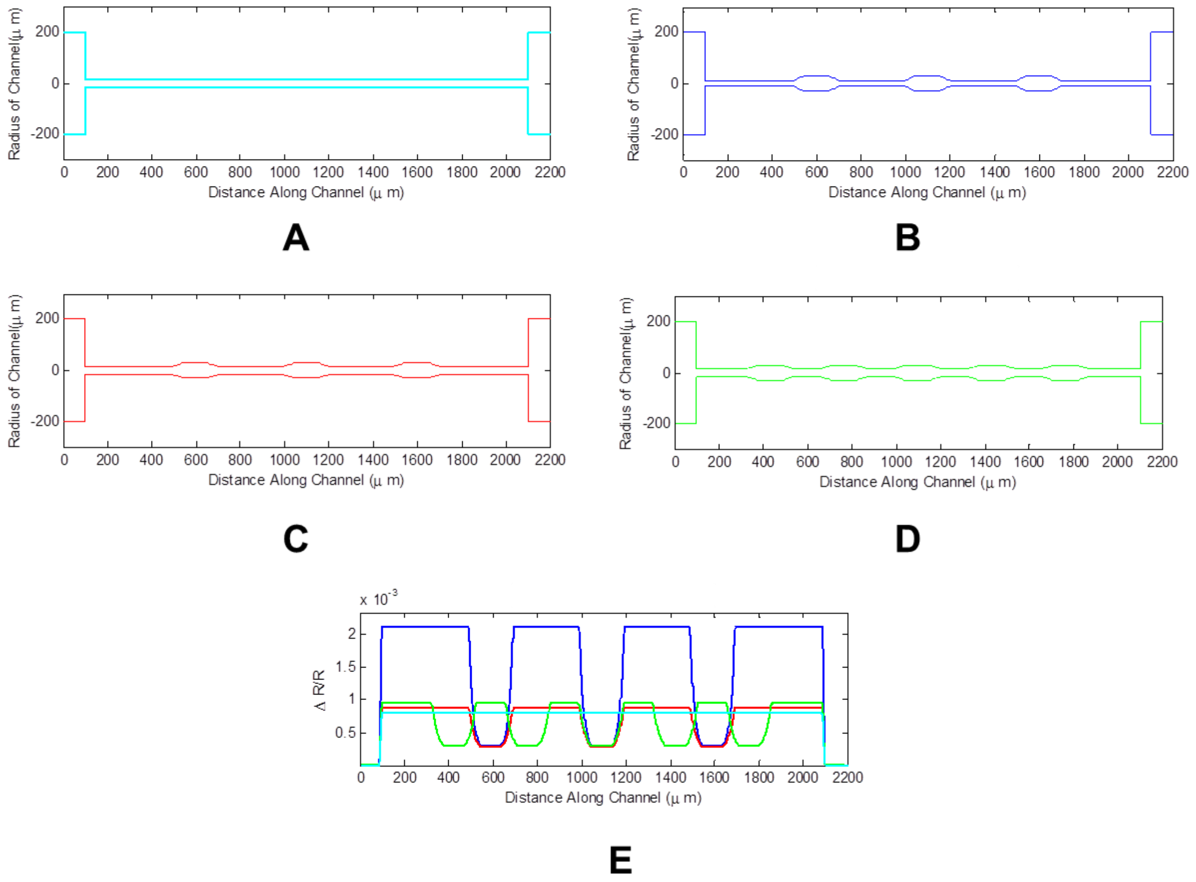

Fig. 2.9: NPS model. A MATLAB simulation was used to study node-pore measurement signals for different parameters. Four different geometries are shown (A-D). The teal geometry (A) consists of a 35 by 35 µm (H x W) with no nodes, the blue geometry (B) consists of 25 by 25 µm pores (H x W) segmented by three nodes, the red geometry (C) consists of 35 by 35 µm (H x W) pores segmented by three nodes, and the green geometry (D) consists of 35 by 35 µm (H x W) pores segmented by five nodes. The measurement signals generated from a particle transiting the node-pores (E) are determined by the geometry designs.

2.1.5 Particle size determination with node-pores

Similar to traditional pore measurements, the normalized current change, node-pores also provide information on the size of the particle passing through them. To account for the influence of nodes in the pore, an effective diameter for the node-pore can be determined using colloids of known size, which can be used to calibrate for particle size determination. By measuring normalized current values caused by particles of known size transiting a node-pore, Eq. 2.6 can be used to determine the effective diameter of the pore, as shown in Fig. 2.10.

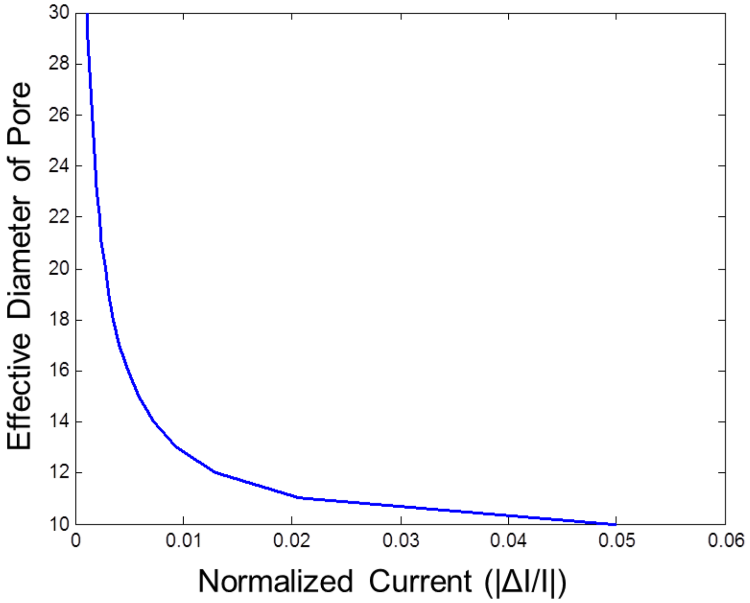

Fig. 2.10: Determining effective diameter of a pore. By measuring normalized current changes from particles of known size, Eq. 2.6 can be used to determine the effective diameter of a pore. The plot shown is for a pore of length 1000 µm and particle size 10 µm.

2.1.6 Multi-marker screening using node-pores

As mentioned earlier, traditional RPS pores are limited by their single-marker screening capability. A major advantage of the signal generated from node-pores is the ability to functionalize different regions of the node-pores with different chemical modifications (Fig. 2.11), such that multiple different particle-pore interactions can be probed in a single electronic measurement. For example, if a cell expresses a surface antigen that can interact specifically with the functionalized antibody in a particular segment of a node-pore, transient interactions will retard the cell motion through that segment. Assuming the nodes are equally spaced, these specific interactions result in a longer sub-pulse duration as compared to that recorded when the cell transits the isotype-control segment of the node-pore (Fig. 2.11).

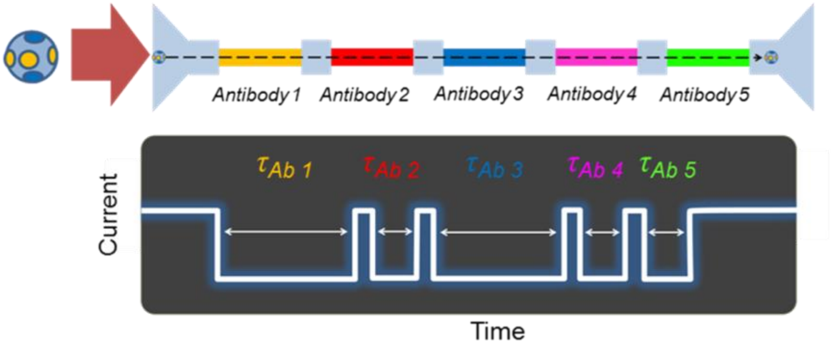

Fig. 2.11: Multiple antibody NPS measurement. As a cell transits a node-pore functionalized with five antibodies (top), the modulated current pulse produced (bottom) reflects the interactions between cell surface-markers and the functionalized segments. For the schematic shown, the cell expresses two markers that specifically interact with Antibodies 1 and 3, leading to longer transit times, τ_{Ab1} and τ_{Ab3}, in these segments as compared to the transit times, τ_{Ab2}, τ_{Ab4}, and τ_{Ab5}, recorded when the cell traverses through the other segments of the node-pore.

Antibody arrangement or placement of the isotype-control segment does not influence transit times, as a cell slows down significantly in the nodes between every measurement region, as we verified by fluid-dynamic simulation. We used a COMSOL Multiphysics simulation (Fig. 2.12) to understand how the fluid velocity through a node-pore is influenced by the presence of nodes.

The device modelled had pore dimensions 18 µm x 18 µm (H x W) with five 1150 µm long segments separated by four nodes, each 58 µm wide and 50 µm long. We used an input pressure of 0.3 kPa and flow was modelled as water at room temperature (25 C). The fluid density used was 999.6 kg/m^3 and the dynamic viscosity was 100 x 10^{-5} Pa s, corresponding to Re ~ 0.025 in the pore and Re ~ 0.016 in the node. The maximum mesh element size was 4.5 µm, and the mesh used two boundary layers with thickness 1.125 µm and 1.350 µm. As shown, the flow velocity, and thus particle velocity, through the node-pore significantly decreases through each node, effectively "resetting" the velocity of each particle before each pore segment region. This resetting allows us to pattern different regions of the node-pore with different antibodies and take independent transit-time measurements. By functionalizing each segment of a node-pore with a different antibody that corresponds to a different cell-surface marker, and by comparing the duration of the sub-pulses to that of the isotype control, we achieve label-free multi-marker screening, as we will show in Chapters 6 and 7.

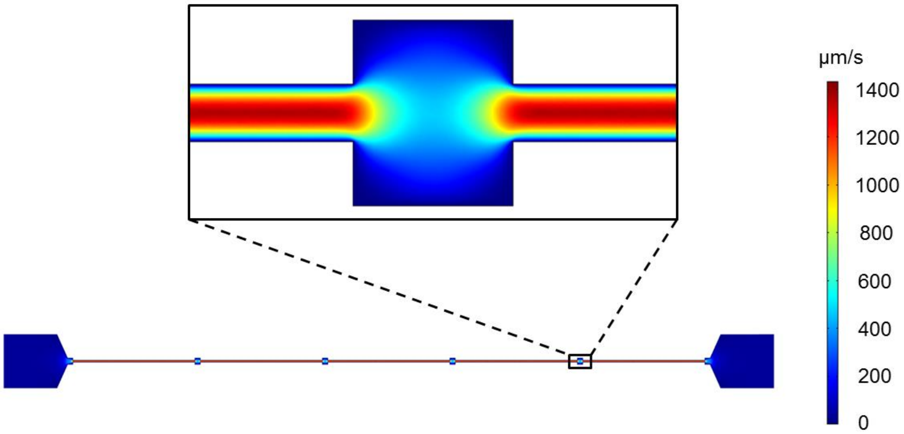

Fig. 2.12: Model of fluid flow through a node-pore device. Fluid flow slows down significantly in each node, allowing for cell velocities to "reset" in between each measurement region, independent of antibody interaction or lack of interaction in the region before each node. The colored scale indicates the values for the velocity profile simulated.

2.2 Conclusion

As discussed in this chapter, the resistance changes detected in RPS and NPS measurements as cells transit pores can reveal insight into cell characterization. In particular, these techniques provide a means for determining cell size as well as cell surface marker profiles by measuring protein-protein interactions between specific cell-surface markers and antibodies on device substrates. In the next chapter, I will describe in detail the manufacturing processes that are used to fabricate the pore devices that are used for experiments throughout this thesis.

Chapter 3

Device Fabrication and Measurement

In this chapter, I outline the manufacturing steps required to fabricate the RPS single-pores and the node-pores described throughout this thesis.[1]

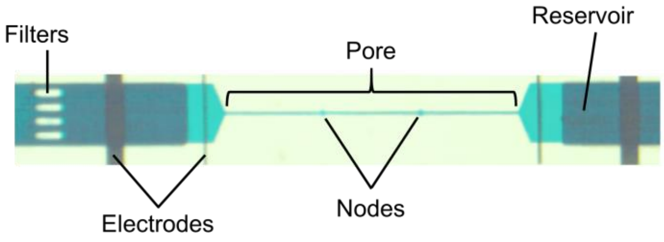

Fig. 3.1: A node-pore device. A node-pore with two nodes equally spaced along the length of the pore is shown. Each component of the device is labeled accordingly. Filters remove cellular debris and clumps. Four electrodes are used, the inner two controlling the voltage, and the outer two carrying the electrical current.

Fabrication of pore devices involves preparing both patterned substrates with electrodes pre-defined and polydimethylsiloxane (PDMS) molds containing the microfluidic channels. The overall process flow is outlined Fig. 3.2.

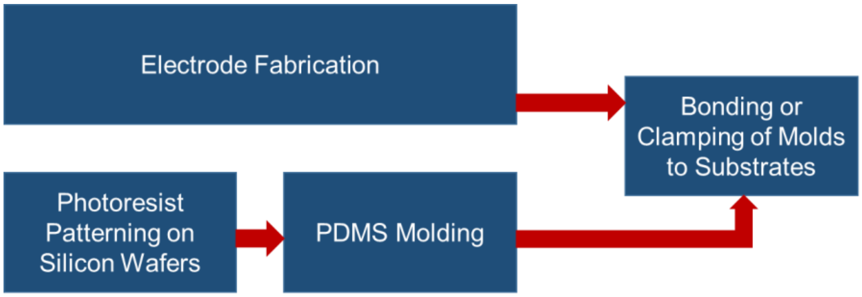

Fig. 3.2: Manufacturing of pore devices. Patterning of electrodes onto glass substrates is necessary to prepare substrates. Soft lithography using silicon wafers and PDMS is used to construct the microchannel molds, which are subsequently bonded or clamped to the glass substrates.

---

[1] This chapter is adapted from 25. Balakrishnan, K. and L.L. Sohn, *Cell screening using resistive-pulse sensing*, in *Methods in Cell Biology*, P.M. Conn, Editor. 2012, Elsevier. p. 369-387.

3.1 Device Fabrication

3.1.1 Electrodes

We define electrodes onto glass substrates to perform the four-terminal measurement of the electrical current across the pores. To pattern the electrodes and contact pad design, we use standard photolithography. We spin Shipley S1813 photoresist (SPR) onto pre-cleaned glass slides (VWR) at 3000 RPM for 60 seconds to achieve a resist height of ~1.5 µm. We then bake the SPR at 110 °C for 1 minute on a hotplate and subsequently expose the resist-coated substrate to a mask using UV light (~400 nm) for 25 seconds at 275 W. We develop the exposed SPR using MF 321 developer for 15 seconds, and subsequently wash the glass substrates thoroughly with 18 MΩ de-ionized (DI) water and dry with dry nitrogen gas. Following patterning, we mount the patterned substrates onto a holder, and insert them into an electron-gun evaporator for metal deposition (Fig. 3.3A). After evaporating a 75 Å titanium (Ti)/ 250 Å platinum (Pt)/ 250 Å gold (Au) layer onto the substrates (Fig. 3.3B), we perform a lift-off step in acetone to remove excess metal (Fig. 3.3C). We next pipette 30 µL of Au etchant (Transene Company) onto the electrodes (not the contact pads) for 30 seconds to expose the Pt layer. We stop the etching process by rinsing thoroughly with DI water (Fig. 3.3D).

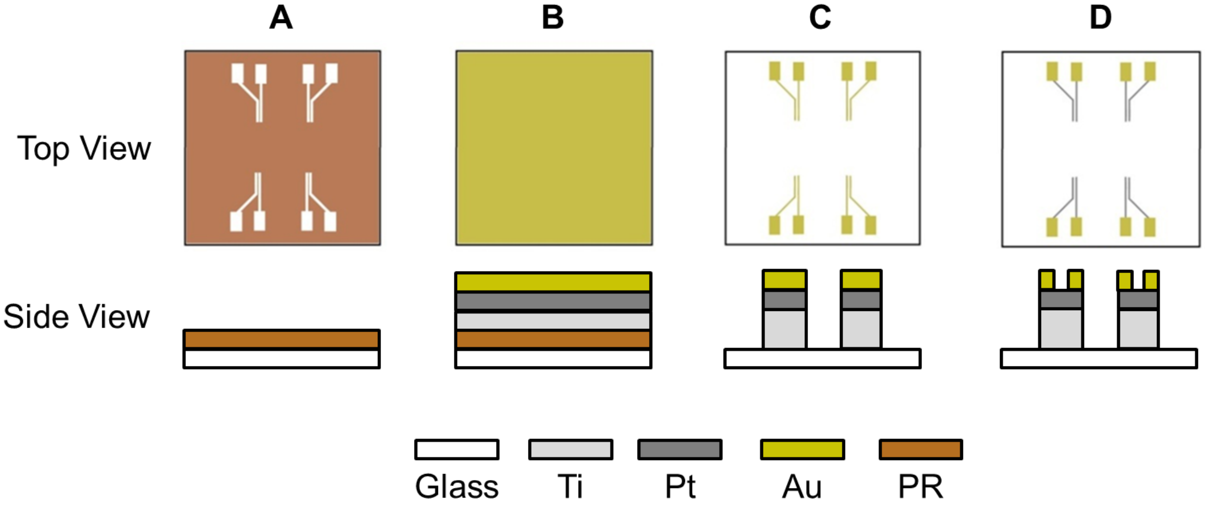

Fig. 3.3: Electrode fabrication. Top view and side view of electrode fabrication process flow is shown in four steps. (A) A glass substrate patterned with photoresist prior to metal deposition. Substrate after (B) Ti, Pt, and Au deposition, (c) acetone liftoff is complete, and (D) gold etching to expose Pt electrodes. Contact pads remain Au-coated.

3.1.2 Negative Relief Masters

To create negative masters of the pore devices, we lithographically pattern a silicon wafer. The process flow for the patterning, outlined in Fig. 3.4, involves patterning the pore structures first and then the reservoir structures. Because the dimensions of the pores and reservoirs are dependent on the specific sensing application, e.g. detecting viral particles (~100 nm in size) or screening large leukemic blast cells (> 12 µm in size), we use different SU-8 photoresists (MicroChem). For the overview below, we outline the procedure for creating an 800 µm x 25 µm x 25 µm (L x W x H) pore that we have used to screen stem cells (see Chapter 4).

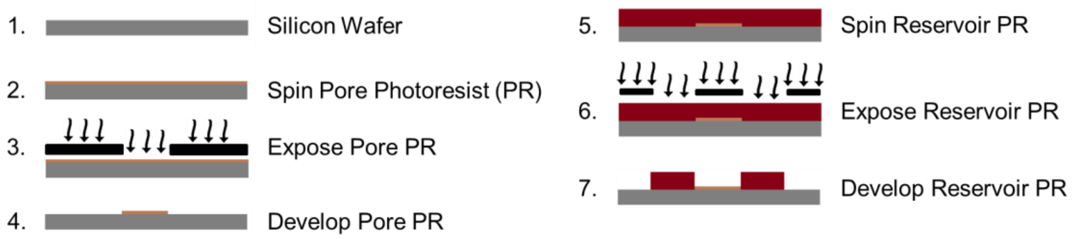

Fig. 3.4: Photoresist process flow to create the negative-relief masters. The steps involved in patterning a silicon wafer with two layers of SU-8 resist (pore and reservoir) are outlined. A side view is shown in the schematics.

We first spin a resist layer (SU-8 2025) at 3500 rpm for 30 sec. to produce a 25-µm thick resist layer. After soft-baking the wafer on a hot plate at 65 ºC for 1 minute and then hard-baking at 95ºC for 5 minutes, we expose the wafer to a mask that has the specific pore design (Fig. 3.5) with UV light (275W, 22 secs). After exposure, we heat the wafer at 65 ºC for 1 minute and then 95 ºC for 1 minute before cooling and developing in SU-8 Developer for 4 minutes. We then thoroughly rinse the wafer with isopropanol (IPA) and subsequently anneal the wafer to remove any cracks in the resist. Such annealing involves heating the wafer to 100ºC and then over a period of 5 minutes, gradually raising the temperature to 150ºC, the temperature at which the wafer remains for one hour.

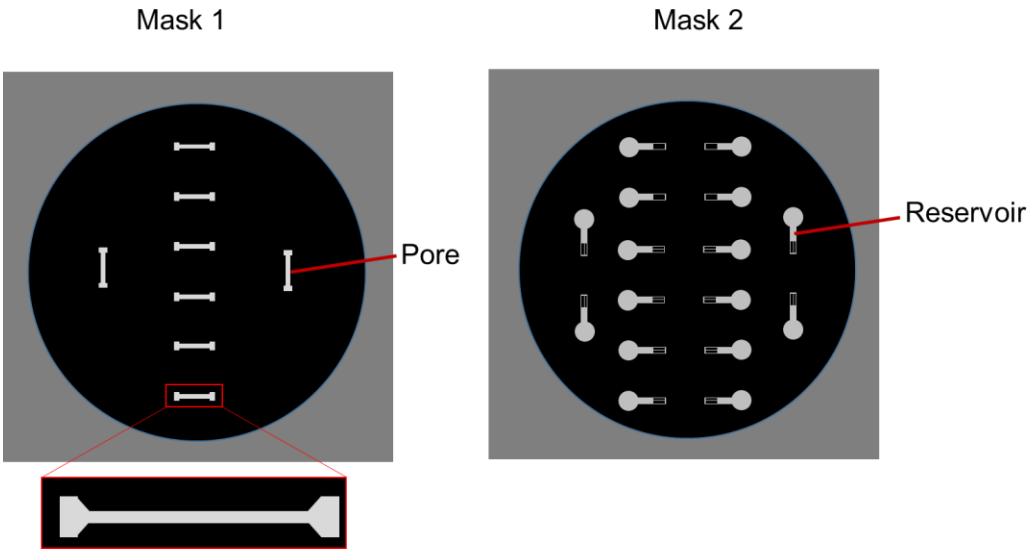

Fig. 3.5: Images of the masks used to fabricate a pore device. The mask is transparent in regions where UV light should be exposed to the photoresist. Two masks are shown, one for the pore (Mask 1), and one for the reservoirs (Mask 2). UV-exposed areas crosslink, resulting in those regions forming SU-8 resist structures on the silicon wafer after development.

After cooling, we spin SU-8 2100 photoresist (3000 rpm, 30s) onto the wafer to create 100 µm-tall reservoirs. As with the first SU-8 layer, we soft-bake the wafer 65 ºC for 5 minutes and then hard bake at 95 ºC for 20 minutes. We align the mask that has the reservoir design over the resist-coated substrate (such that the pore connects to the two reservoirs to be patterned, Fig. 3.6) under a microscope and expose to UV light (275W, 70 secs). We then place the wafer on a hot plate at 65 ºC for 5 minutes and subsequently at 95 ºC for 10 minutes. After baking, we develop with SU-8 developer for 10 minutes and rinse with IPA. We finally do another hard bake to anneal any cracks in the reservoir layer.

Fig. 3.6: Image showing the connection of the pore and reservoir layers. The green region indicates where the initial pore layer had been patterned. The reservoir mask is aligned such that the pore connects the two reservoirs of each device.

3.1.3 PDMS molds

We mold the integrated pore-reservoir structures pores with PDMS. After thoroughly mixing Dow Corning Sylgard 184 Base with Curing Agent in a 10:1 ratio and degasing the mixture in a vacuum desiccator, we carefully pour this mixture onto the negative relief master (Fig. 3.7) and cure the PDMS at 80 ºC for 45 minutes. Once the PDMS is cured, we cut the mold out with an X-Acto knife and core the inlet and outlet holes with a 16-gauge syringe needle.

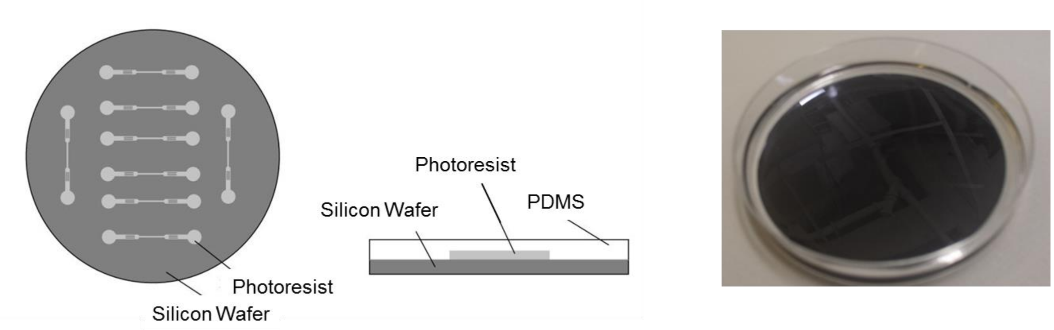

Fig. 3.7: Silicon wafer PDMS molding. Top (left) and side (middle) view schematics of a silicon wafer with multiple negative-relief structures of the pore devices. The side view shows PDMS poured over the wafer design. The image on the right shows a wafer in a petri dish with PDMS poured for molding.

3.1.4 Plasma bonding

For devices which require the PDMS molds to be bonded permanently to glass substrates, we expose both the PDMS molds and the glass substrates with oxygen plasma. After coring the inlet and outlet holes, we clean the PDMS molds with Scotch tape. Small PDMS “guards” are used to cover the silanized regions (if applicable) of the prepared glass substrates (Fig. 3.8). We subsequently expose both the substrate and PDMS to oxygen plasma (100 mT, 5 mA, 30 s) using a PlasmaTherm 790 system. After exposure, we remove the PDMS guards from the substrate and we deposit 10 µl of a 2:1 methanol: DI water mixture onto the glass substrate. After aligning the PDMS mold on top of the glass substrate, we place the entire device onto a hot-plate, initially set at 50 ºC. We then ramp the temperature of the hotplate to 120ºC for 45 minutes, thereby creating the permanent bond. The permanent bond was tested by flowing pressurized air (~100 KPa) into the bonded PDMS device.

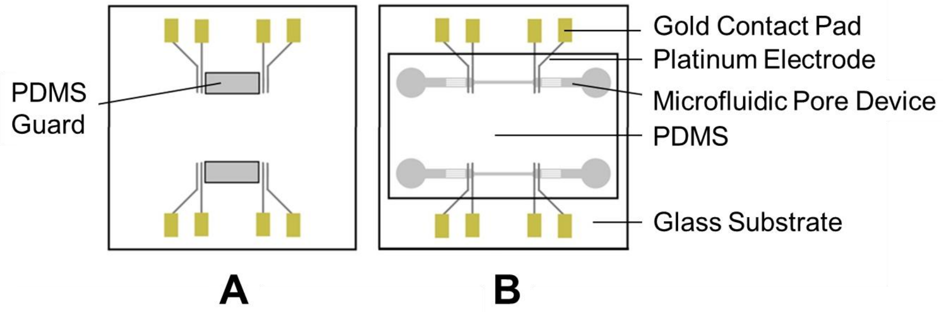

Fig. 3.8: Schematic of PDMS guards and bonding. (A) Schematic of a patterned glass substrate with PDMS guards over the regions that have been silanized. The guards shield this region during oxygen plasma exposure (B) A two-pore device that has been assembled by bonding the PDMS mold to the silanized substrate.

3.1.5 Device clamp

In certain scenarios, plasma bonding is not a favorable option, such as when we perform multiple antibody patterning using temporary channels (see Chapter 6). In these cases, we use a different mold for antibody incubation than for the actual pore-device. For this reason, the processing steps (e.g. heating) that are necessary for plasma bonding cannot be performed, in order to preserve the quality of the antibody functionalization. Instead, we clamp the microchannel mold to the glass substrate using a custom designed clamp (Fig. 3.9). The design consists of two access holes for inlet and outlet ports and was 3D printed using acrylonitrile butadiene styrene (ABS) polymer.

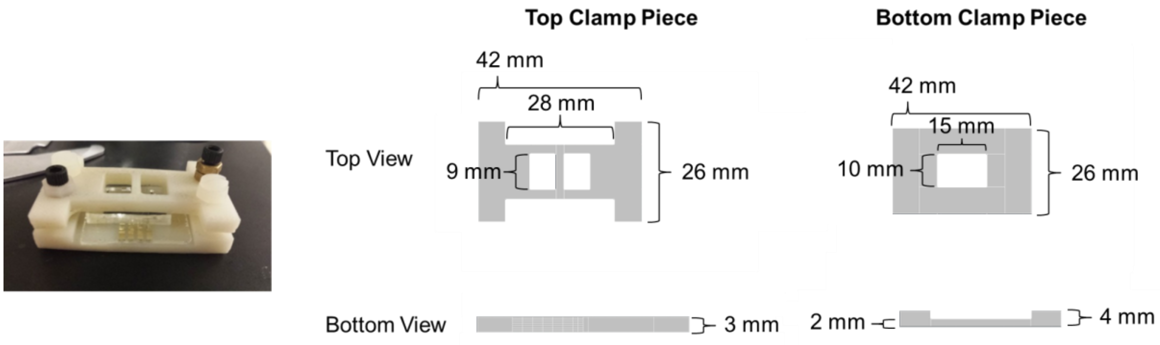

Fig. 3.9: Device clamp design. The clamp used to attach PDMS molds to glass substrates (left). The top and bottom view of the top (middle) and bottom (right) of the clamp are shown with dimensions shown in millimeters.

3.2 Platform setup

3.2.1 Data acquisition and analysis

Fig. 3.10 shows a diagram of the circuit used to measure the electrical current across a pore. The circuit is adapted from that found in O. A. Saleh's doctoral thesis [13]. As shown, we utilize a four-point measurement to remove the electrode/fluid interfacial resistance using a constant applied voltage (0.2-0.5 V). We use an INA110KP instrumentation amplifier, as this amplifier has a low input bias current and high input impedance. We use an OPA27GP operational amplifier for its high precision and low noise. The electrical current through the pore device runs from I_2 to I_1 to I_{out}. The electrical current passes through a current preamplifier (DL Instruments 1211) that converts the input current into a voltage signal before the measurement is sent to a DAQ Board (National Instruments PCI-6035E) for data sampling and subsequently processed using LabVIEW.

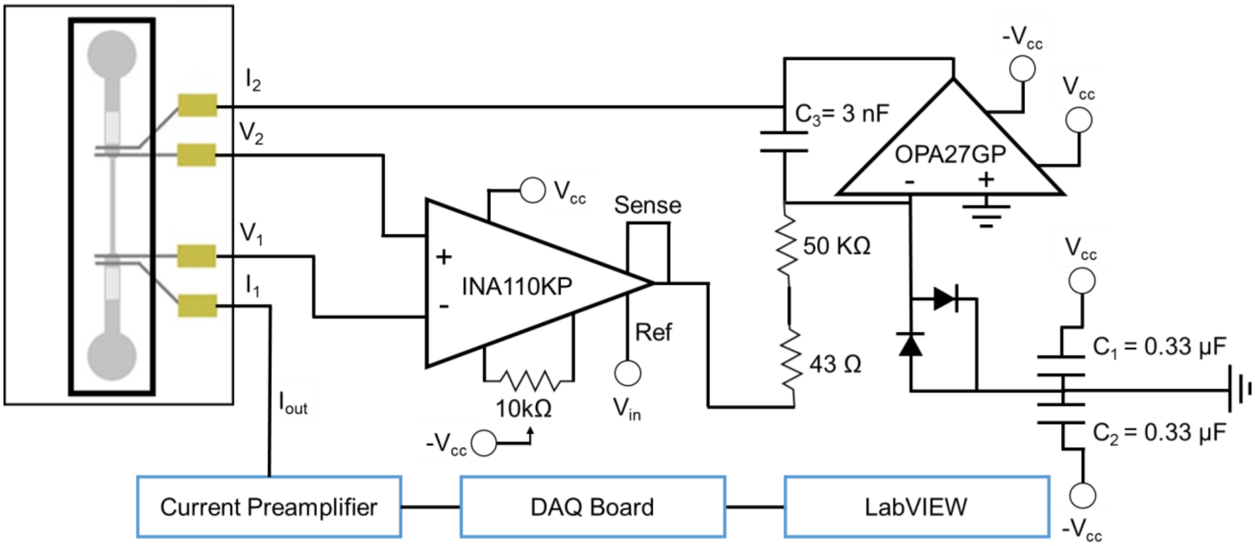

Fig. 3.10: Schematic of the circuit used for all of the electrical measurements in this thesis. The pore device and four contact pads are shown on the left. The output current passes into a current amplifier, a DAQ Board, and finally analyzed in LabVIEW.

3. 3 Antibody immobilization techniques

The immobilization of antibodies onto surfaces has been of significant value for diagnostic immunoassays and sensors. As mentioned earlier, our method of sensing also benefits from this technique, as pore devices functionalized with antibodies provide insight into the biomarkers expressed on cells, allowing for characterization beyond cell size. Carbonaro et al. demonstrated that functionalized pore devices provide a label-free technique for characterizing individual cells based on surface marker expression [18]. The sensitivity of such assays depends on the quality of antibody patterning. In particular, the specific binding capacity of the antibodies is influenced by antibody density on the substrate and the antibody orientation on the support surface. These characteristics influence the number of and specificity of binding events, and ultimately the sensitivity of surface marker characterization.

Antibodies are Y-shaped proteins that are used by the immune system to neutralize foreign bodies. Antibodies recognize unique antigens on these bodies and can bind to them, neutralizing them or tagging them in a manner that triggers immune system targeting. This is because the “top” end of the Y of an antibody contains a paratope that is specific for an epitope on an antigen. This antigen binding site is shown in Fig. 3.11. As shown, an antibody molecule is made of two Fab regions and a fragment crystallizable (Fc) region. The Fc fragment contains two identical protein fragments. The Fab regions contain variable sections that correspond to the specific target to which the antibody can bind.

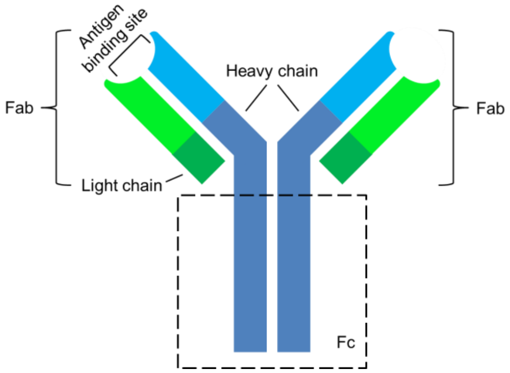

Fig. 3.11: Antibody schematic. An antibody molecule contains different fragments - an Fc region and two Fab regions. Antibodies are made of structural units containing heavy and light chains.

In certain coupling scenarios, there is no discrimination between which attachment points are chosen, and the location of binding to a surface can randomly occur close to or far away from the binding sites, as shown in Fig. 3.12. Thus, antibody spatial orientations on the substrate of interest can prevent the actual antigen-antibody binding complexes from forming [26].

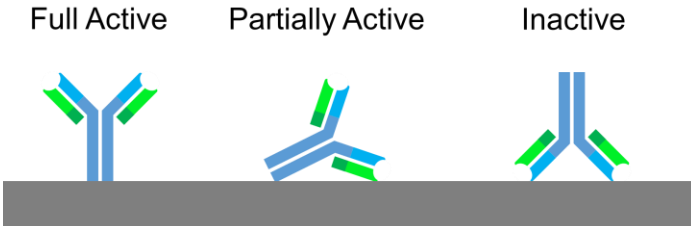

Fig. 3.12: Antibody orientation. Adapted from [26]. Random coupling results in different orientations of the antibody onto the substrate.

As shown in Fig. 3.12, immobilization of the antigen binding sites (shown in the right), can severely reduce or even eliminate the ability of the antigens on a cell to bind to the antibody. To counter these issues, antibodies can be bound to Fc receptors on solid supports, such as Protein G, an immunoglobulin-binding protein that is expressed in group C and G Streptococcal bacteria, which we utilize for our immobilization. Through this technique, the antigen-specific binding sites remain open.

To successfully pattern antibodies onto glass substrates, the glass surface must be modified. Silanization is a common way to introduce a variety of functional groups onto a glass surface [27]. We use APTES (3-aminopropyltriethoxysilane) to coat the glass surface with aminosilane groups that are subsequently coupled with a crosslinker (Sulfo-EGS is shown) that then bind to Protein G to achieve antibody immobilization, as shown in Fig. 3.13. Different strategies for antibody immobilization are outlined in the next section.

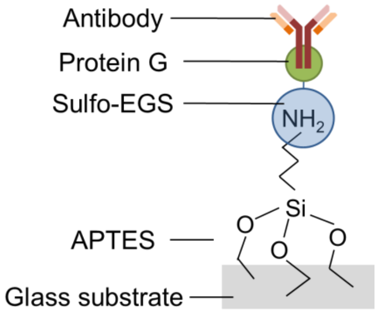

Fig. 3.13: Functionalization schematic to immobilize and orient antibody on glass substrates. APTES is first coated onto glass substrates, followed by Sulfo-EGS crosslinker. Protein G is then attached to Sulfo-EGS, followed by antibody immobilization.

To achieve the optimal antibody functionalization on our substrate, we tested several different methods for protein attachment. The different strategies involved using a variety of silanization techniques and crosslinkers. We utilized APTES in combination with acetone, ethanol, or toluene, and the crosslinkers tested included Sulfo-EGS (Ethylene glycol bis[sulfosuccinimidylsuccinate]) (Pierce), ANB-NOS (N-5-Azido-2-nitrobenzoyloxysuccinimide) (Pierce), and Sulfo-LC-SDA (Sulfosuccinimidyl 6-(4,4'-azipentanamido)hexanoate) (Pierce). Sulfo-EGS is a water-soluble crosslinker with amine-reactive sulfo-NHS-ester ends. ANB-NOS is a crosslinker with an amine-reactive NHS ester and a photoactivatable nitrophenyl azide. Sulfo-LC-SDA also combines the NHS-ester with photoactivatable properties and uses diazirine-based photoreactions that can be activated using long-wave UV-light.

Table 3.1. Protocols for substrate functionalization for antibody surface modification.

Test	Silanization Technique	Crosslinker	Spiked Protein G	Cross-linker Before Protein G
1	APTES + Ethanol	Sulf-EGS	X	
2	APTES + Ethanol	ANB-NOS	X	
3	APTES + Ethanol	Sulfo-LC-SDA	X	
4	APTES + Ethanol	Sulf-EGS		X
5	APTES + Ethanol	ANB-NOS		X
6	APTES + Ethanol	Sulfo-LC-SDA		X
7	APTES + Toulene (long bake)	Sulf-EGS	X	
8	APTES + Toulene (long bake)	ANB-NOS	X	
9	APTES + Toulene (long bake)	Sulfo-LC-SDA	X	
10	APTES + Toulene (long bake)	Sulf-EGS		X
11	APTES + Toulene (long bake)	ANB-NOS		X
12	APTES + Toulene (long bake)	Sulfo-LC-SDA		X
13	APTES + Toulene (short bake with rinse)	Sulf-EGS	X	
14	APTES + Toulene (short bake with rinse)	ANB-NOS	X	
15	APTES + Toulene (short bake with rinse)	Sulfo-LC-SDA	X	
16	APTES + Toulene (short bake with rinse)	Sulf-EGS		X
17	APTES + Toulene (short bake with rinse)	ANB-NOS		X
18	APTES + Toulene (short bake with rinse)	Sulfo-LC-SDA		X
19	APTES + Acetone	Sulf-EGS	X	
20	APTES + Acetone	ANB-NOS	X	
21	APTES + Acetone	Sulfo-LC-SDA	X	
22	APTES + Acetone	Sulf-EGS		X
23	APTES + Acetone	ANB-NOS		X
24	APTES + Acetone	Sulfo-LC-SDA		X

We first cleaned the glass substrates prior to antibody functionalization to remove any organic contaminants on the substrate surface. We placed the substrates in a 1:10 ammonium hydroxide (NH4OH) : 18 MΩ deionized (DI) water solution and heated the solution to 150°C for 10 minutes. 30% Hydrogen peroxide (H_2O_2) was then added to the solution (for a final mixture ratio of 1:1:10 H_2O_2 : NH_4OH : DI water). After 10 minutes, we removed the glass substrates, rinsed them with DI water and methanol (MeOH), and subsequently dried them with dry nitrogen gas.

The process flow for functionalizing the cleaned substrates is outlined in Fig. 3.14. Stage 1 of the functionalization procedures involved applying the aminosilane to the cleaned substrates.

Different APTES preparations were utilized for silanization. In one test, a 2 : 5 : 93 APTES : DI water : ethanol mixture was incubated for 10 minutes in microfluidic channels. The mixture was then incubated for five minutes and washed with 95% ethanol four times before heating at 100 C for 15 minutes. In another test, two different toluene techniques were used. The first involved mixing toluene in a 1:10 APTES : toluene ratio and also incubating for 10 minutes. Channels were then flushed out with air and heated at 80 C for 4 hours. The other toluene mixture was prepared with APTES in a 1: 20 APTES : toluene ratio and incubated in the channels for five minutes at room temperature. These devices were then flushed with toluene and rinsed with acetone before heating at 100 C for 1 hour. The APTES-acetone preparation involved mixing at a 1:50 APTES : acetone ratio and incubating for 1 minute at room temperature. We used acetone to wash the channels before drying and heating them at 100 C for 15 minutes.

Stage 2 involved injecting crosslinker into microchannels. We injected either Sulfo-EGS or Sulfo-LC-SDA dissolved in phosphate buffered saline solution (PBS) at a 1 mg/100 µL ratio. ANB-NOS was dissolved in DMSO (dimethyl sulfoxide) with HEPES (4-(2-hydroxyethyl)-1-piperazineethanesulfonic acid) in a 1 mg : 100 µL : 4 µL ANB-NOS : DMSO : HEPES ratio. Stage 3 involved Protein G application. Two methods of Protein G application were used. Protein G was mixed in with these solutions in a 1 mg/mL ratio prior to overnight incubation in some devices. Other devices were incubated with these solutions for 1 hour prior to overnight incubation with a 1 mg/mL Protein G/PBS mixture. Pressurized air was used before antibody was added and incubated for four hours. Finally, antibody was flushed out of the microchannels, and PBS was used to wash them. The PDMS channels were then removed and the glass substrates (the regions which containing the microchannels) were imaged using a fluorescence microscope.

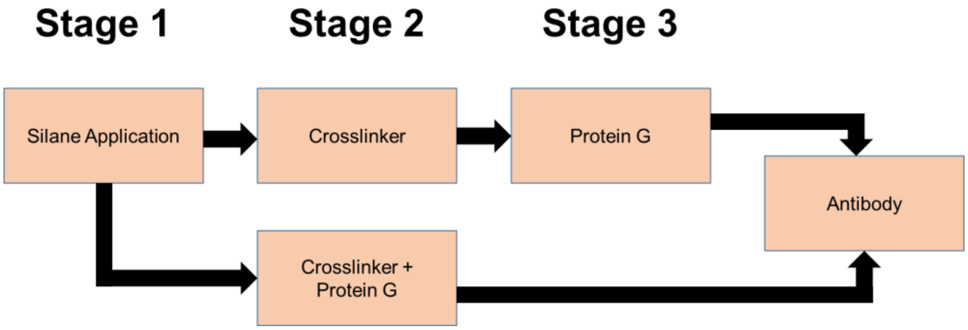

Fig. 3.14: Process flow for substrate functionalization. The different stages of silane, crosslinker, and Protein G application are indicated.

Fig. 3.15 summarizes the results for testing these protocols involving four different APTES mixtures, three different crosslinkers, and two different Protein G applications.

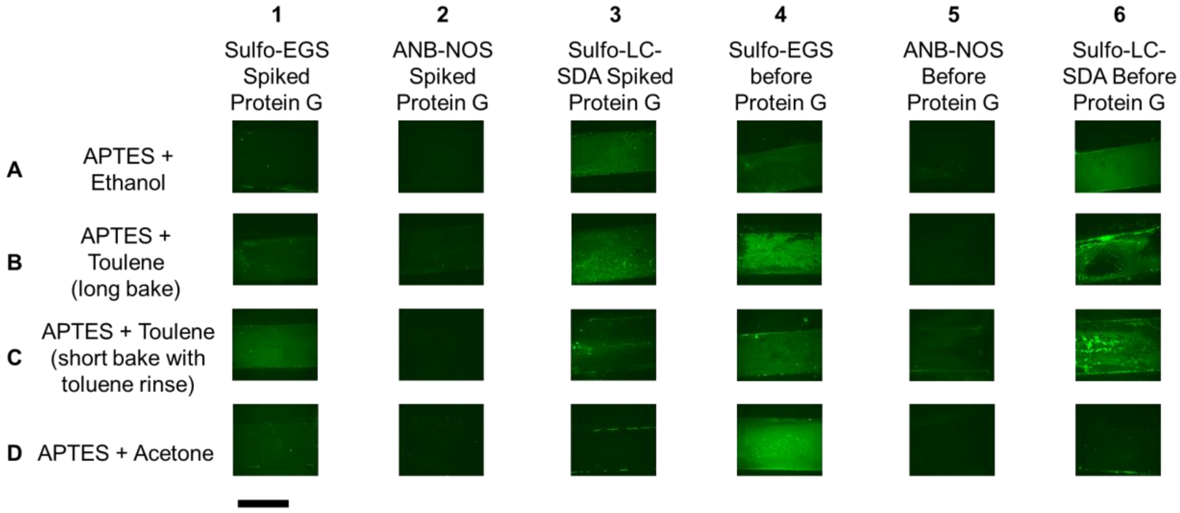

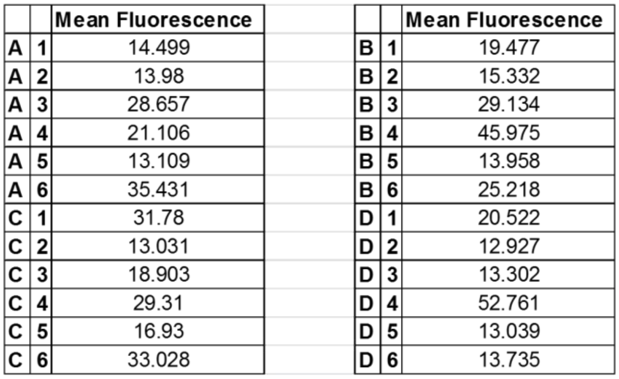

		Mean Fluorescence
A	1	14.499
A	2	13.98
A	3	28.657
A	4	21.106
A	5	13.109
A	6	35.431
C	1	31.78
C	2	13.031
C	3	18.903
C	4	29.31
C	5	16.93
C	6	33.028

		Mean Fluorescence
B	1	19.477
B	2	15.332
B	3	29.134
B	4	45.975
B	5	13.958
B	6	25.218
D	1	20.522
D	2	12.927
D	3	13.302
D	4	52.761
D	5	13.039
D	6	13.735

Fig. 3.15: Matrix of antibody immobilization techniques. 24 different silanization and crosslinker application techniques were tested. The regions of the glass substrates which contained the microchannels were imaged using a fluorescence microscope. As shown below, the mean fluorescence of the regions where the channel was placed on the substrate was calculated using ImageJ. Scale bar is 800 µm.

The regions of the glass substrates which contained the microchannels were imaged using a fluorescence microscope, and ImageJ was used to determine the levels of mean fluorescence (Fig. 3.15, bottom) in the regions where the microchannels were used. Overall, spiking crosslinker in Protein G prior to application did not yield successful immobilization as incubating crosslinker prior to protein G application. We determined the acetone and APTES silanization technique in combination with Sulfo-EGS crosslinker being incubated before Protein G application to be the best protocol, as indicated by the highest mean fluorescence value. This protocol provided a consistent pattern of immobilized antibody on the glass substrate and did not require the extra UV activation step that was needed for the UV-activated crosslinkers. Ultimately, functionalization quality depends on functionalization protocol, substrate type, and steric considerations. While we used fluorescence imaging, a more thorough analysis of these techniques could be performed using spectroscopy.

3. 4 Conclusion

As discussed in this chapter, there are several fabrication steps that are needed to manufacture RPS and NPS devices. Depending on the application (single or multi-marker screening), plasma bonding or clamping of pore device molds to substrates can be done. To accomplish surface-marker screening, we optimized our substrate functionalization technique by testing out several different protocols, ultimately identifying a combination of APTES silanization and Sulfo-EGS crosslinker followed by Protein G application to be the best substrate modification prior to antibody incubation.

Chapter 4

Screening and sorting single satellite cells from individual myofibers

4. 1 Introduction

This chapter outlines our work in applying our cell-screening platform to the stem-cell field by screening and sorting single muscle satellite cells from mice as published in Chapman, Balakrishnan, et al [28][2]. An understanding of both embryonic organogenesis and adult tissue regeneration relies on isolating and characterizing stem cells. In general, these cells are difficult to study because they constitute minute populations in organ niches and express multiple cell-surface markers, only some of which are known. Furthermore, their properties change quickly *in vitro* and possibly even during isolation procedures [29-31]. The different combinations of markers used to identify muscle satellite cells (e.g. CD34 [32, 33], CXCR4 [34], β1-integrin [34], Sca-1 [33, 34], M-cadherin [32], and Syndecan-4 [35]) illustrate the on-going debate as to which cell-surface markers do, indeed, identify particular rare stem cells. Fueling this debate are a number of important factors including: the known heterogeneity of muscle stem cells, variations introduced during sample isolation and processing, the difficulty in determining gene-expression accurately/quantitatively in the low starting stem-cell numbers within the micro-anatomical niche (i.e., a single myofiber), and the inability to functionally characterize single quiescent satellite cells.

Traditional quantitative methods of fluorescence-activated cell sorting (FACS) and magnetic-activated cell sorting (MACS) analysis are designed for large numbers of cells and cannot be easily applied to niche-specific characterization. In the case of muscle satellite cells, FACS and MACS cannot distinguish subsets of cells isolated from different myofibers or even different muscle groups. Microscopy, although capable of imaging stem cells in their niches, neither provides a straightforward means to quantify gene-expression levels, nor allows further characterization of immunostained cells. Adding to the overall complexity is the fact that FACS, MACS, and fluorescence microscopy depend on irreversible antibody binding to stem-cell surface proteins that then become internalized, likely altering cell properties, including gene expression and regenerative capacity [36].

In the work described in this chapter, we demonstrated the utility of our cell screening technique to characterize single, functional organ stem cells. As a first step, we screened primary-culture mouse myoblasts for Sca-1 and M-cadherin and compared our results with flow cytometry. We next screened satellite cells freshly isolated from single fibers of non-injured extensor digitorum longus (EDL) muscle [37, 38] for heterogeneous cell-surface marker expression, and subsequently sorted and characterized these cells for their myogenic capacity. We also compared

---

[2] The work in this chapter was done in collaboration with Matthew Chapman, Ju Li, Michael Conboy, Haiyan Huang, Swomitra Mohanty, Eric Jabart, James Hack, and Irina Conboy. All cell culture, harvesting, and imaging was done by Ju Li.

the marker heterogeneity of freshly isolated and cultured satellite cells and confirmed that the variance in expression levels increased with culture. After identifying Sca-1 expressing cells in the muscle stem-cell micro-niche, we isolated Sca-1 expressing cells and studied their myogenicity. Overall, we demonstrated the capability to analyze rare stem cells quantitatively but also the ability to purify and subsequently characterize these cells with our screening and sorting process.

4.2 Experimental Procedures

4.2.1 Harvesting of satellite cells from single muscle fibers

Un-injured EDL muscle was dissected from the hind leg of 3-month old C57/black-6 mouse and incubated at 37^{o}C in digestion medium (250 U/mL Collagenase type II (Sigma) in DMEM, buffered with 30 mM HEPES, pH 7) for 1 hour with gentle agitation [39]. Digested muscle was gently triturated through a flame-polished Pasteur pipette, fibers were settled briefly and pipetted to a tissue-culture dish in DMEM/F12 with 2 % horse serum. Single muscle fibers were handpicked under a microscope and satellite cells (Fig. 4.1A) were liberated from three single fibers by digestion for one hour, with 1 U/mL Dispase (Gibco#17105-014) and 40 U/mL Collagenase type II in medium). Freshly isolated satellite cells were directly analyzed with prepared RPS single-pore microfluidic devices (described in below and in Chapter 3).

4.2.2 Culture of activated satellite cells from single muscle fibers

Un-injured EDL muscle was dissected from the hind leg of 3-month old C57/black-6 mouse and incubated at 37^{o}C in digestion medium (600 U/mL Collagenase type I (Sigma) in DMEM, buffered with 30 mM HEPES, pH 7) for 2 hours with gentle agitation [39]. Digested muscle was gently triturated through a flame-polished Pasteur pipet, fibers were settled briefly and pipetted to a tissue culture dish in plating medium (DMEM/F12 with 2 % horse serum) for culture and activation overnight. Single fibers were handpicked under microscope and cultured in myoblast growth medium [DMEM/F12 with 10 % Bovine Growth Serum (Hyclone) and 5 ng/mL FGF-2], to further activate satellite cells for two days. Satellite cells were liberated from three single fibers by digestion for one hour, with 1 U/mL Dispase (Gibco) and 40 U/mL Collagenase type II in medium before analyzed with prepared (RPS single-pore) microfluidic devices.

4.2.3 Isolation and sorting of Sca-1-GFP myoblasts, and immunofluorescence staining

Fresh Sca-1-GFP muscle from a transgenic mouse, obtained from Dr. Zena Werb's research laboratory in the Dept. of Anatomy, University of California-San Francisco [40], was digested and bulk myofibers with satellite cells were isolated as published [41]. Bulk fibers were cultured in myoblast growth medium (DMEM/F12 with 10 % Bovine Growth Serum (Hyclone) and 5 ng/mL FGF-2) for three days; myogenic cells were prepared from the culture as published [41], and cultured for an additional day in growth medium on dishes coated with diluted Matrigel in PBS (3 µg/mL/cm^2). Myogenic cells were washed and lifted in PBS and live sorted by FACS on GFP for three populations: low/no GFP (21 %), intermediate GFP (34 %) and high GFP (17 %). The three populations were plated in Matrigel-coated chamber slides and cultured in growth medium overnight, then cultured in differentiation medium (2 % horse serum in DMEM) for four days. Cells were then imaged for GFP fluorescence, fixed in 4 % paraformaldehyde (5 minutes), and immunostained for embryonic myosin heavy chain (eMyHC) and GFP, as published.

4.2.4 Statistical analysis of transit-time data

Two different methods, Dixon's Q Test [42-44] and FDR, were employed to compare the transit times of cells passing through isotype control channels to those functionalized with an antibody specific for expressed surface markers (e.g. Sca-1, CXCR4, M-cadherin, β1-integrin, Notch-1, and Syndecan-4). For larger quasi-bulk samples (i.e. screening Notch-1 expression in satellite cells), an FDR was used to control for false positives [45]. We analyzed only those data that corresponded to cells of size 8-13 µm, the size range of satellite cells [41].

4.2.5 Device functionalization and assembly

RPS single-pore devices were prepared as described in Chapter 3. Antibodies were functionalized onto glass substrates using several steps, as outlined in Chapter 3 as well. Briefly, APTES was first coated onto glass slides. Next, Sulfo-EGS crosslinker was used to attach Protein G to the surface. Finally, the antibodies corresponding to the cell-surface antigens to be screened were immobilized via Protein G. A detailed overview of the functionalization technique used can be found in Chapter 9: Protocols.

4.2.6 Cell Size Determination

The effective diameter, *D*, of the microchannels used for testing was first determined experimentally by measuring the normalized pulse magnitude of 15 um colloids (Bangs Laboratories) transiting the microchannel. The pulse magnitude was averaged over three runs on three different devices made with the same master. The effective diameter of the microchannel was determined to be *D*= 24 µm using Eq. 2.3. We subsequently were able to determine the size (diameter, *d*) for each cell measured.

4.2.7 Screening primary-culture mouse myoblasts for Sca-1 and M-cadherin expression

Primary-culture mouse myoblasts were isolated from freshly harvested mouse EDL muscle. Myoblasts were cultured in Matrigel- coated plates (2 µg/ml/cm^2) in Ham's F-10 media with 20% BGS, 1X penstrep, and 6 ng/ml FGF. Cells were dissociated from the matrigel in PBS with gentle agitation for 3-5 min to prevent digestion of surface receptors prior to screening with prepared microfluidic devices.

4.2.8 Notch receptor screening

The preparation of satellite cells for notch receptor screening can be found in Chapter 9.

4.2.9 Analysis of Sca-1 expression through immunofluorescence staining and microfluidic channel capture

Myofiber-associated satellite cells were isolated as published [41]. Fresh, isolated satellite cells were injected into a 100 µm x 2000 µm x 40,000 µm (H x W x L) microchannel functionalized with a saturating concentration of anti-Sca-1 antibody (Table A.1) at a flow rate of 10 µL/min. Sca-1$^+$ cells became bound to the functionalized antibodies, and therefore captured. As a control, freshly isolated satellite cells were also injected into the same-sized microchannel functionalized with IgG_{2a} control antibody. As expected, no cells were captured with the control channel. Staining details can be found in Chapter 9.

4.3 Results

4.3.1 Description of the device, procedure, and control experiments

For our measurements, single satellite cells, freshly isolated from individual myofibers of uninjured EDL muscle (Fig. 4.1A), were injected directly into a PDMS microfluidic channel (Fig. 4.1B) that was functionalized with a saturating concentration of either a specific or isotype-control antibody. A non-pulsatile pressure of 17.4 kPa [4] was used to drive single satellite cells through filters, an inner reservoir, and finally through the functionalized microchannel for measurement. Immediately after screening, each cell was collected and sorted in a separate well of an 8-well slide using a pressurized flow of media in the outlet reservoir (Fig. 4.1C).

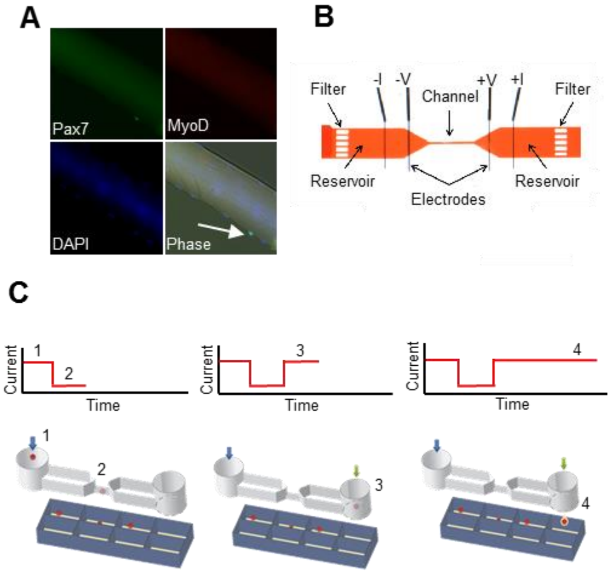

Fig. 4.1: Detailed view and description of the stem-cell analysis platform. (A) Freshly isolated single myofiber that has been immunostained. Satellite cells are sub-laminal and one expresses the conventional myogenic marker Pax7 (white arrow). No satellite cells express MyoD, indicating that the cells are not activated. Blue corresponds to Hoechst nuclear dye, and green to anti-Pax7 antibody. Scale bar corresponds to 100 µm. (B) Optical image of an actual device, consisting of two reservoirs connected by a single microchannel (800 µm x 25 µm x 25 µm, L x W x H), all embedded in a polydimethylsiloxane (PDMS) slab sealed to a glass substrate. (C) Schematic of cell sorting: a cell is initially injected into the microfluidic device (1), flows through the microchannel for measurement (2), and enters the exit chamber as a transverse flow of media is triggered (3) that enables collection in an individual well for culture (4). [28]

4.3.2 Screening of primary-culture myoblasts for Sca-1 and M-cadherin expression

To show that our method was capable of quantitatively determining both the expression and lack of expression of a particular surface antigen in a population, we screened primary-culture mouse myoblasts for Sca-1 and M-cadherin in prepared microchannels (Fig. 4.2). To identify Sca-1^+/M-cadherin$^+$ cells among the cells that passed through an anti-Sca-1/anti-M-cadherin antibody microchannel, we first estimated the empirical probability density function for all cells passing through an IgG_{2a} control microchannel. With the estimated probability density function serving as a null distribution, we next computed the p-value and corresponding False Discovery Rate (FDR) for each cell passing through an anti-Sca-1/anti-M-cadherin antibody microchannel. The FDR was computed as follows: Let $p(i)$ denote the ith largest p-value among all cells. We estimated the corresponding FDR (when $p(i)$ is used as a cutoff to determine Sca-1^+/M-cadherin$^+$ cells) by $m * p(i)/i$, where m denotes an (overly) estimated number of Sca-1^- cells, e.g., m can be the total number of cells passing through the anti-Sca-1 antibody microchannel. In agreement with previous reports that were based on FACS analysis, we found that 2.7% of the cultured myoblasts were Sca-1^+ [46] and 93.0% were M-cadherin$^+$ [47-49] (Fig. 4.2).

To demonstrate that our method could accurately analyze primary organ stem cells, both our functionalized microchannels and conventional flow cytometry to screen for Sca-1 expression. To identify Sca-1^+ cells, we performed an FDR analysis where, instead of using the empirical (i.e., non-parametric) probability density function, we used a parametric approach to estimate the probability density function (in a log-normal distribution family) for all cells passing through an IgG_{2a} control microchannel. We chose this parametric estimation because 1) the data fits the log-normal distribution very well and 2) there is less estimation of parameters involved so that the results are expected to be more robust. In our analysis for mouse myoblasts for Sca-1 and M-cadherin expression described above, the data did not seem to fit any parametric distribution, so a non-parametric estimation of the probability density function looked more appropriate. As shown in Fig. 4.3, the accuracy of our device and method are validated, as there is excellent correlation between the two analysis methods: 67.6% were determined to be Sca-1^+ by our method and 66.1% by the gold standard, FACS.

4.3.3 Niche-to-Niche Variation of Sca-1, CXCR4, β1-integrin, M-cadherin, Syndecan-4, and Notch-1 Expression

The presence, absence, and fiber-to-fiber heterogeneity of the surface markers Sca-1, CXCR4, β1-integrin, M-cadherin, Syndecan-4, and Notch-1 expressed by freshly isolated muscle satellite cells were examined. To ensure that our sample processing did not introduce artifacts, we hand-selected individual myofibers from bulk muscle for all our experiments. Furthermore, we sampled a subset of these single myofibers and immunostained them to ensure that all satellite cells were sub-laminal, expressed the conventional myogenic marker Pax7, and did not express MyoD or Ki67. In so doing, we confirmed that the satellite cells we studied were not activated from the technique we used to isolate the cells from single muscle fibers [37, 38].

The p-values were calculated directly from null distributions of transit time. For each control sample (consisting of cells passing through the isotype control microchannel), a null distribution was estimated parametrically by fitting a Normal or Gamma distribution based on the empirical distribution shape of the control sample. Let $F_0(t)$ denote the estimated cumulative density function of null distribution for the control sample of, say Sca-1. Then the p-value for transit time t_x for a cell x passing through an anti-Sca-1 antibody microchannel can be calculated by $1- F_0(t_x)$. We performed this p-value calculation on cells for all markers except β1-integrin. We categorized the cells into different expression groups as follows: cells whose transit times were significantly high (with raw p-values < 0.001 and Bonferroni corrected p-values < 0.05) were considered to have high levels of expression (Figs. 4.4, 4.5, and 4.6, A.1, red), while less stringent cutoffs on raw p-values of 0.01 and 0.05 were used to determine cells with medium (Figs. 4.4, 4.5, and 4.6, A.1, green) and low (Figs. 4.4, 4.5, and 4.6, A.1, blue) levels of expression of these markers, respectively. Note that the Bonferroni correction was applied here to address the problem of multiple comparisons, since we repeated the p-value calculation on all individual cells. This correction helped control the overall family-wise false positive discovery rate: if the probability of false positives is α for an individual test (i.e., the test at a significance level of α), the overall family-wise false positive discovery rate of n independent tests would be about $n\alpha$; the Bonferroni correction controls the family-wise probability of false positives by testing each of the individual tests at a significance level of α/n.

With the estimated null distributions, we further performed a FDR analysis to confirm our findings. Let p_0 be the p-value cutoff (e.g., $p_0 = 0.001$). Let m_1 be the number of cells with p-values less than p_0, and m_0 be the number of cells with p-values greater than a in the treatment sample. Then we estimate FDR at the p-value cutoff of p_0 as $m_0 p_0/((1-a)m_1)$. We used $a = 0.01$ in our calculations, which generally provides an overestimation of FDRs. The estimated FDRs for cells with high levels of expression are all found to be < 0.01 (actually more than 80% of those cells have FDRs < 0.0001). The estimated FDRs for cells with medium or low levels of expression are mostly found to be < 0.02 and 0.05, respectively. These FDR results, to some extent, provide us a high confidence on the identified Sca-1^+, M-cadherin$^+$, Syndecan-4^+, CXCR4^+, or Notch-1^+ cells.

To determine which cells were Sca-1^+, M-cadherin$^+$, β1-integrin$^+$, Syndecan-4^+, CXCR4^+, or Notch-1^+, we statistically analyzed the transit-time data to assess whether a particular cell had an outlying slow transit time as compared to those cells passing through the isotype control microchannel (Figs. 4.4 and A.1). We analyzed only those data that corresponded to cells of size 8-13 μm, the size range of satellite cells [41]. Because there is a direct correlation between the density of available epitopes and transit time, we can also determine expression levels of Sca-1, M-cadherin, β1-integrin, Syndecan-4, CXCR4, and Notch-1 in satellite cells (not just identify cells as positive or negative). The p-values were calculated directly from null distributions of transit time. For each control sample a null distribution was estimated parametrically by fitting a Normal or Gamma distribution based on the empirical distribution shape of the control sample. Let $F_0(t)$ denote the estimated cumulative density function of null distribution for the control sample of, say Sca-1. Then the p-value for transit time t_x for a cell x passing through an anti-Sca-1 antibody microchannel can be calculated by $1- F_0(t_x)$. We performed this p-value calculation on cells for all markers except β1-integrin. Thus, cells whose transit times were significantly high (with raw p-values < 0.001 and Bonferroni corrected p-values < 0.05) were considered to have high levels of expression (Figs. 4.4, 4.5, 4.6, and A.1, red), while less stringent cutoffs on raw p-values of 0.01 and 0.05 were used to determine cells with medium (Figs. 4.4, 4.5, 4.6, and A.1, green) and low (Figs. 4.4, 4.5, 4.6, and A.1, blue) expression levels of these markers, respectively. In the case of Sca-1, M- cadherin, Syndecan-4, CXCR4, or Notch-1, the p-values were calculated directly from null distributions of transit time; the null distributions were estimated based on cells passing through the isotype control microchannel. With the estimated null distributions, we further performed a FDR analysis to confirm our findings [45]. The FDRs for cells with high levels of expression were all found to be < 0.01 (more than 80% of these cells have FDRs < 0.0001). The FDRs for cells with medium or low levels of expression were mostly found to be < 0.02 and 0.05, respectively. The FDR results provide a high confidence on the identified Sca-1$^+$, M-cadherin$^+$, Syndecan-4$^+$, CXCR4$^+$, or Notch-1$^+$ cells. In the case of β1-integrin, the p-values were calculated from a Dixon's Q Test [42-44, 50], a robust statistical test that is used to identify values that appear diverging from a control sample and ideal for small sample sizes. Determination between the above two ways of p-value calculation was based on the number of cells measured in the control data. The details of this study were as follows. Let $x_1, x_2, \ldots, x_n$ be the transit time of the n cells passing through the IgG control microchannel, and let $y_{i1}, y_{i2}, \ldots, y_{in_i}$ be the transit time of the n_i cells passing through an anti-β1-integrin antibody microchannel in experiment i. For every y_{ij} (the transit time of the jth cell in experiment i), we ran a Dixon's test on $x_1, x_2, \ldots, x_n, y_{ij}$ to detect if y_{ij} was an outlier compared to $x_1, x_2, \ldots, x_n$. For each experiment, the cells with conservative Bonferroni corrected p-values < 0.05 are identified as high expressing β1-integrin$^+$ associated satellite cells. Cells in determined to have medium β1-integrin expression had a raw p-value $<$ 0.01. Further, cells determined to have low β1-integrin expression had a raw p-value < 0.05.

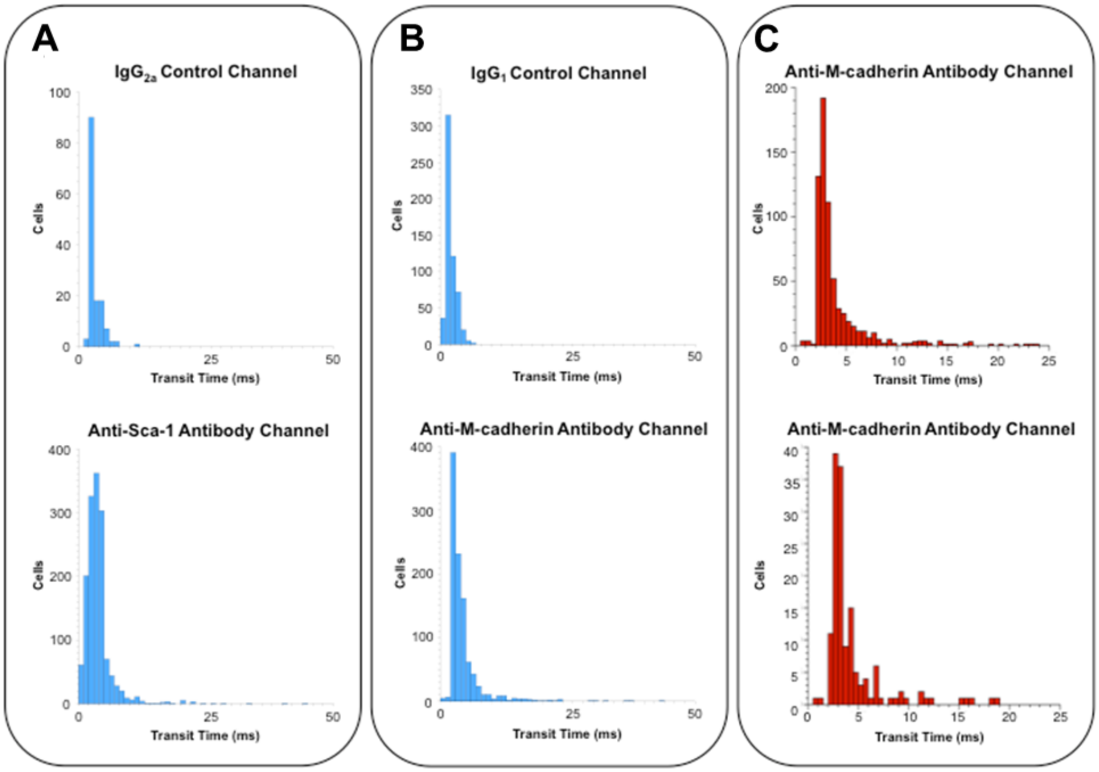

Fig. 4.2: Screening primary-culture mouse myoblasts with functionalized microchannels. (A) Transit-time (τ) distribution of myoblasts screened with IgG$_{2a}$ isotype-control (number of cells, n = 141, $\tau_{avg} = 3.16 \pm 0.13$ ms) and anti-Sca-1 (n = 1469, $\tau_{avg} = 3.89 \pm 0.35$ ms) antibody-coated microchannels, respectively. (B) τ-distribution of myoblasts screened with IgG$_1$ isotype-control (n = 218, $\tau_{avg} = 1.44 \pm 0.55$ ms) and anti-M-cadherin (n = 1004, $\tau_{avg} = 4.45 \pm 3.83$ ms) antibody-coated microchannels, respectively. Using an FDR analysis, 2.7% of cells screened were found to be Sca$^+$ and 93.0% were found to be M-cadherin$^+$. (C) τ-distributions of the same population of myoblasts screened with two different microchannels functionalized with anti-M-cadherin antibody. The distributions are nearly identical (top distribution: n=672, $\tau_{avg} = 4.16 \pm 3.00$ ms; bottom distribution: n=146, $\tau_{avg} = 4.38 \pm 3.00$ ms), thereby demonstrating that the screening method is accurate and reproducible. [28]

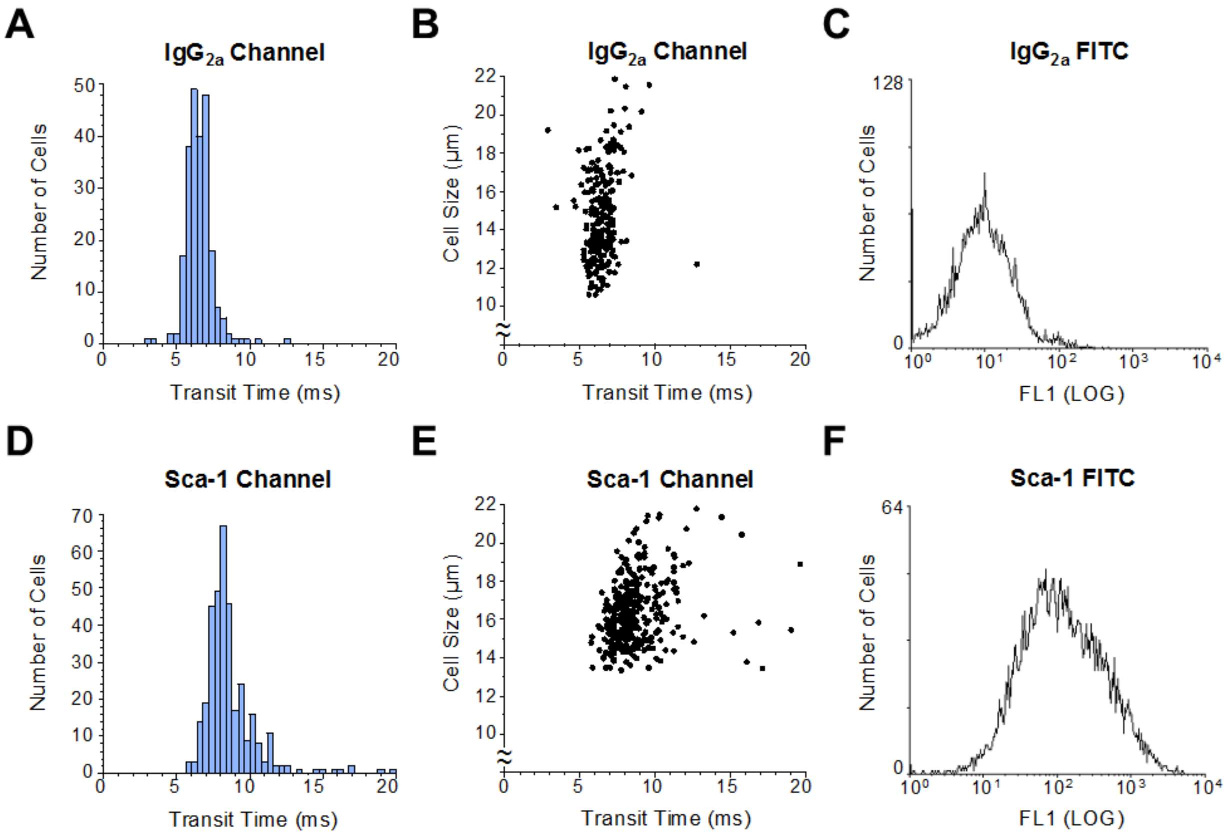

Fig. 4.3: Screening Sca-1+ cells with functionalized microchannels. (A) and (D) τ-distribution of a bulk population of satellite cells derived from uninjured (tibialis anterior and gastroc) muscle**.** Cells transited through microchannels functionalized with either an IgG_{2a} antibody (A) or anti-Sca-1 antibody (D). Using an FDR calculation, 67.6% of the cells were found to be Sca-1^+. (B) and (E) Scatter plot of cell size vs. transit time for cells transiting an IgG_{2a} and anti-Sca-1 antibody microchannel, respectively. In the scatter plots, $R^2 = 0.12$ and 0.06 for (B) and (E), respectively, indicating no correlation between cell size and transit time. (C) and (F) FACS histograms of the same population of cells screened with our microchannel described in (A) and (B). (C) corresponds to cells immunostained with control FITC-labeled IgG_{2a} while (F) corresponds to cells immunostained with FITC-labeled anti-Sca-1 antibody. FACS analysis determined that 66.1% of cells in the population are Sca-1^+. [28]

As shown in Figures 4.5 and 4.6, we found significant heterogeneity between fibers in all studied cell-surface markers. In the summary of experiments we performed for each marker, some fibers had almost no β1-integrin, M-cadherin, Notch-1, or Sca-1 expressing satellite cells. Other fibers had a significant number of satellite cells that express Syndecan-4, β1-integrin, CXCR4, or Notch-1 (>90% total expression). Significantly, almost no fibers had satellite cells with medium or low expression of CXCR4, Notch-1, or M-Cadherin. Notch-1 showed the greatest variability of expression between fibers, while Syndecan-4 showed the greatest variance in expression level of cells positive for this marker.

Following the discovery of microniche-specific heterogeneity of marker expression in satellite cells freshly isolated from single fibers, we investigated whether the high degree of cell-surface marker heterogeneity was due to the transient binding between the functionalized antibody and the cell-surface receptors that could activate receptor signaling and ultimately change cell properties [36]. Since the anti-Notch-1 antibody (specific for the external part of Notch-1 receptor) employed in our microchannels has been shown to mimic the native ligand binding and activate Notch-1 robustly in satellite cells, resulting in high levels of the truncated intracellular portion of Notch that is localized to the cell nucleus [32], we analyzed whether Notch would become activated when detected in freshly harvested satellite cells (Fig. 4.5B). As additional controls, unscreened satellite cells were plated on IgG_1 and anti-Notch-1 antibody-coated culture wells overnight. To determine whether the transient interactions between the extracellular portion of the receptor and the functionalized antibodies activated the Notch pathway, we performed immunofluorescence on all cells using an antibody that specifically recognizes the truncated-activated form of Notch-1. In contrast to wells coated with anti-Notch-1 antibody, which induced robust nuclear-active Notch, cells from the IgG_1 and anti-Notch-1 antibody microchannels and the IgG_1-coated wells showed low levels of Notch activation (Figs. 4.5b). Thus, the transient binding between functionalized antibody in our microchannel and specific receptors *does not* significantly contribute to Notch-pathway activation in satellite cells, thereby providing strong evidence that changes in signal transduction and cell behavior should not be expected when stem-cell populations are screened with our method.

The high degree of variation of surface-marker expression levels between fibers that our method detected is surprising, and the first to be reported. To validate that this heterogeneity is an accurate reflection of the screened surface-markers, we compared freshly isolated and cultured satellite cells and found that, as expected, the heterogeneity and variance in expression levels of the studied markers increased upon *in vitro* culture (Figs. 4.5 and 4.6). Similar analyses using the Dixon's Q Test and a Bonferroni correction, as before, were performed to determine high, medium, and low expressions of Sca-1^+, $CXCR4^+$, M-$Cadherin^+$, and β1-$Integrin^+$ activated satellite cells.

Overall, our data suggest that individual myofibers from non-injured EDL muscle are heterogeneous with respect to the expression levels of Sca-1, M-cadherin, β1-integrin, Syndecan-4, CXCR4, and Notch-1 on their associated satellite cells. Our findings are highly consistent with previous reports, which have indicated that the muscle satellite-cell population is heterogeneous between different mice [51] and muscle groups [52]. At the same time, our data are the first to reveal the variation of satellite cell subsets among single fibers in the same muscle and to establish quantitatively and directly this heterogeneity based on multiple surface markers.

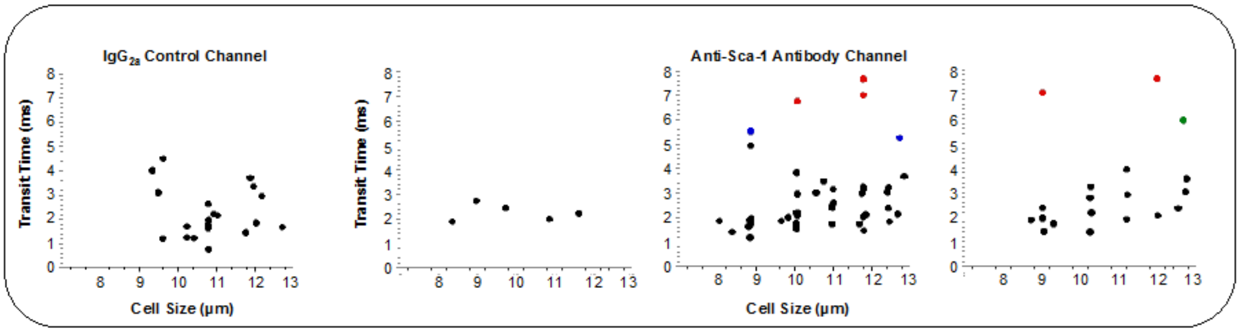

Fig. 4.4: Screening analysis of satellite cells freshly derived from single muscle fibers. Transit time of freshly isolated satellite cells for different experiments. Sca-1$^+$ cells were identified by statistically assessing whether a particular cell had an outlying slow transit time as compared to those cells passing through the isotype control microchannel (p-values were calculated). Syndecan-4$^+$, β1-integrin$^+$, CXCR4$^+$, Notch-1$^+$,and M-cadherin$^+$ data is shown in Fig. A.1 in the Appendix. Under different p-value cutoffs, cells can be considered as having a high expression (red), medium expression (green), low expression (blue), or no expression (black). Each experiment consisted of cells collected from 3 single muscle fibers and screened with a different anti-Syndecan-4 antibody microchannel. Based on an FDR analysis, cells were determined to have high (red), medium (green), low (blue), or no (black) Syndecan-4 expression. [28]

4.3.4 Correlating Myogenicity with the Heterogeneity of Cell-Surface Markers

Satellite cells were isolated as above from single myofibers of non-injured EDL muscle and screened and sorted by our microfluidic channels functionalized with anti-β1-integrin and anti-CXCR4 antibodies. Single cells with known levels of β1-integrin and CXCR4 were then plated and cultured for 14 days (the time-frame during which quiescent satellite cells are typically activated in culture and form myogenic colonies [56]). The capacity to form colonies of myogenic progenitor cells (Pax7$^+$ and/or MyoD$^+$) was assessed for each satellite cell that was isolated from each myofiber and the myogenicity was correlated with the levels of cell-surface markers, as shown in Chapman, et al. [28]. These results demonstrated that our device is capable of sorting single satellite cells and analyzing the correlation between their cell surface-marker expression and their myogenicity.

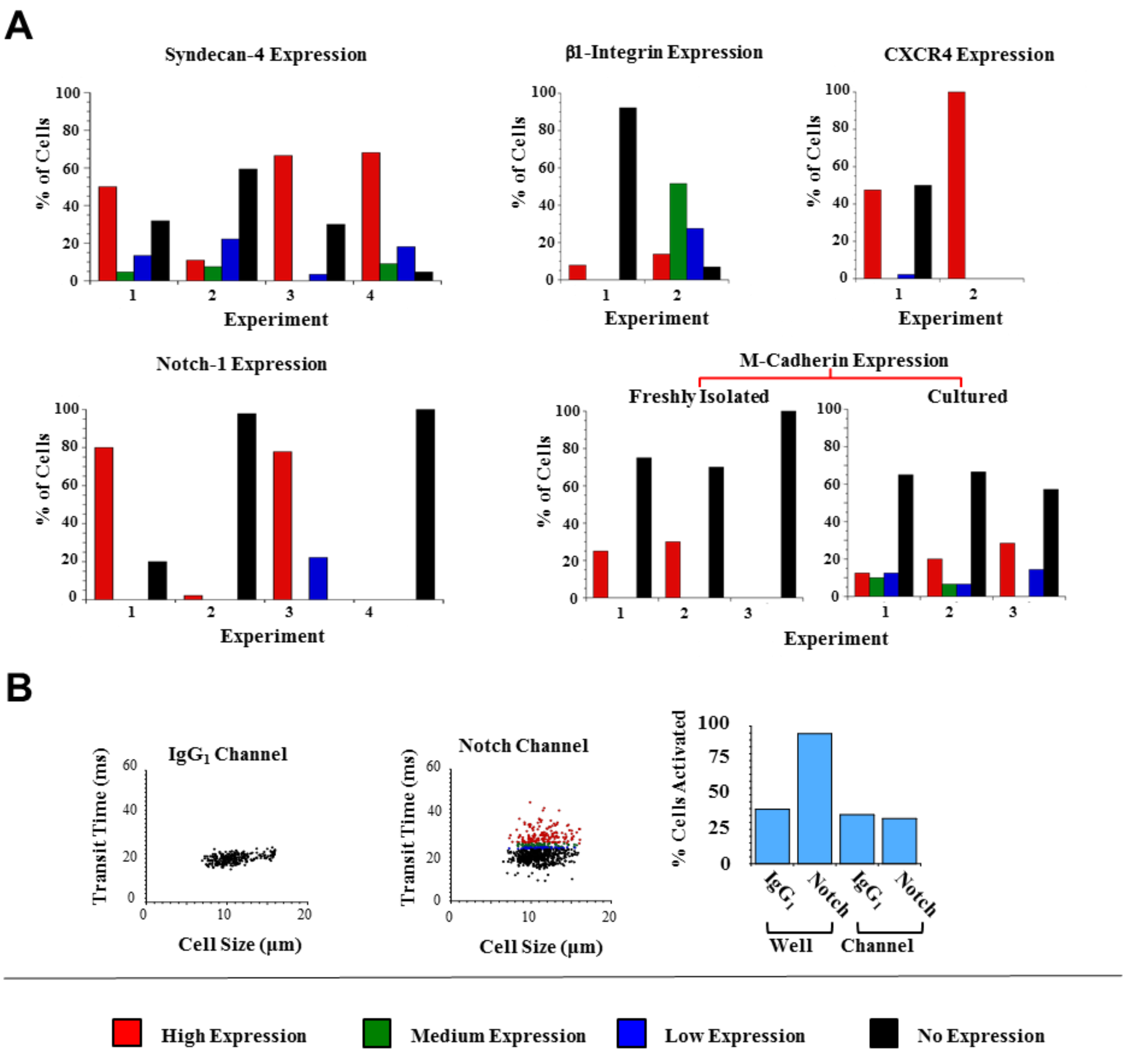

Fig. 4.5: Screening analysis of satellite cells freshly derived from single muscle fibers. (A) Summary of the observed expression levels of Syndecan-4 (Experiments 1, 2, 3, and 4 with n=20, 26, 28, and 22 cells, respectively); β1-integrin (Experiments 1 and 2 with n=38 and 29 cells, respectively); CXCR4 (Experiments 1 and 2 with n=23 and 11 cells, respectively); Notch-1 (Experiments 1, 2, 3, and 4 with n=5, 43, 9, and 32 cells, respectively); and M-cadherin (Experiments 1, 2, and 3 with n=8, 10, and 3 cells, respectively). All markers screened show a wide range of heterogeneity from fiber to fiber. Heterogeneity and variance in expression levels of the studied markers increase upon muscle-stem-cell activation. The bars correspond to the percentages calculated from the raw transit-time data. (B) Screening for Notch-1 protein expression on the surface of satellite cells. Transit time vs. cell size for satellite cells screened with a 2000 μm-long IgG_1 or Notch-1 microchannel. τ_{avg} = 19.80 ± 2.36 ms for the IgG_1 microchannel and τ_{avg} = 22.93 ± 4.83 ms for the Notch-1 microchannel Using an FDR calculation, with cutoffs of 0.1, 0.05, and 0.01, 21% of the 757 cells screened, had high levels of Notch1 expression (red), 8% had medium levels of expression (green), 9% had low levels (blue), respectively. The remaining cells (62%) did not express Notch1 (black). Percentage of cells showing high levels of nuclear Notch-1 after screening vs. control cultured conditions. Cells were not activated when screened with our microchannels. [28]

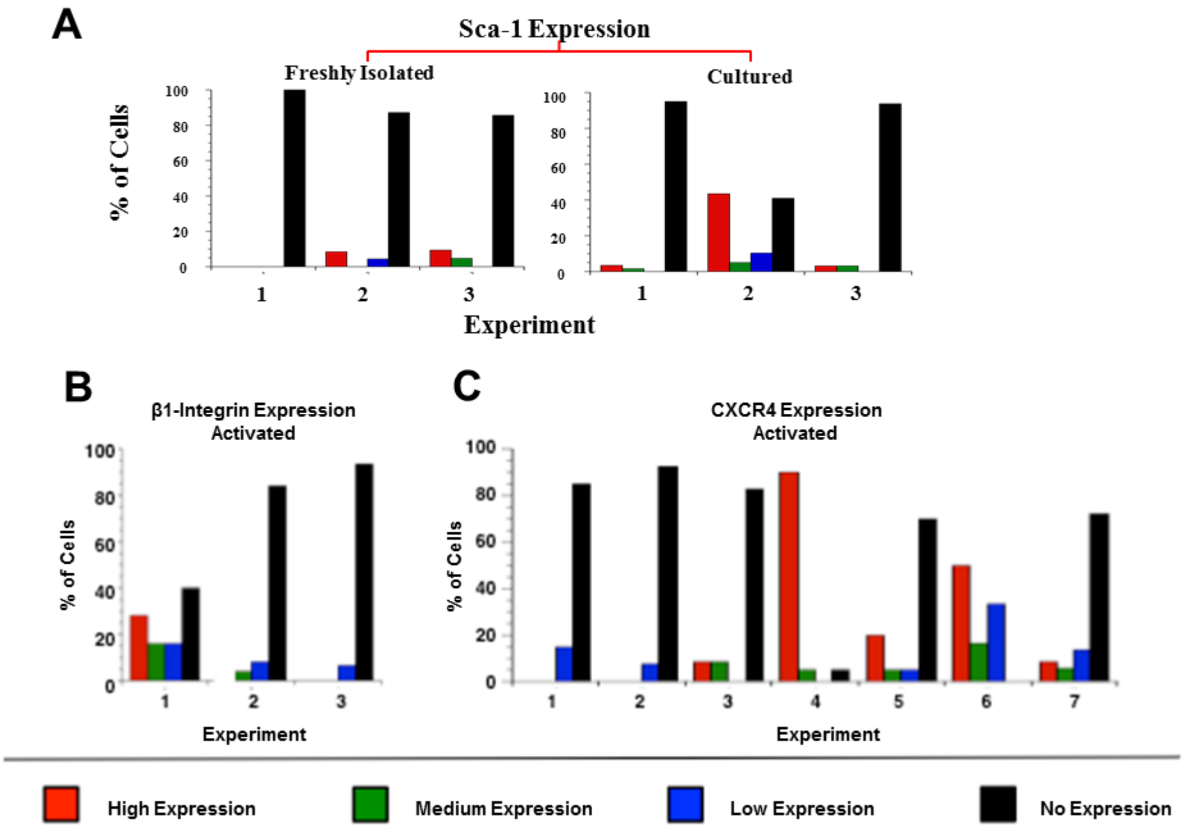

Fig. 4.6: Cultured and activated satellite cell screening. (A) Summary of the observed expression levels of Sca-1 in freshly isolated (Experiments 1, 2, and 3 with n=5, 47, and 21 cells, respectively) and cultured satellite cells (Experiments 1, 2, and 3 with n = 60, 39, and 33 cells, respectively). (B) β1-integrin marker screening of cultured activated satellite cells derived from single muscle fibers. Each experiment consisted of cells collected from 3 single muscle fibers and screened with a different β1-integrin antibody microchannel, each 800 μm-long. Based on Dixon's Q Test (see Supporting Information Materials and Methods for analyses details), cells were determined to have high (red), medium (green), low (blue), or no (black) β1-integrin expression. Experiments 1, 2, and 3 consisted of n=25, 25, and 15 cells, respectively. Wide heterogeneity in the expression of the β1-integrin marker is evident from fiber to fiber. (C) CXCR4 marker screening of cultured activated satellite cells derived from single muscle fibers. 800 μm long microchannels were used for Experiments 1-3 (n=20, 27, and 35 cells, respectively); 2000 μm long microchannels were used for Experiments 4-7 (n=20, 20, 6, and 36 cells, respectively). All markers screened show a wide range of heterogeneity. [28]

4.4 Discussion

This chapter describes how our sensing platform can be used to screen successfully rare subsets of stem cells and to subsequently sort these cells for downstream analysis. Particularly germane to the muscle stem-cell field, we show that with our technique, we can quantify the heterogeneity of a number of surface-markers expressed by satellite cells. In addition, we are able to isolate cells and show the potential of correlating surface-marker expression to myogenicity at the single-cell level. Equally important, with our Notch-1 screening, we have demonstrated that our label-free method which relies on transient binding between antibody and receptor does not lead to cell activation. While further testing on a per-cell type, per-marker basis is necessary to confirm this characteristic of our platform in other applications, we believe that we have already gone beyond conventional techniques in which irreversible antibody binding may lead to cell activation or changes in the physical properties of the cells.

To demonstrate the strong potential of our method for analyzing stem cells from their microniche, we chose to screen muscle (satellite) stem cells from single muscle fibers. Beyond muscle stem cells, our method could be broadly applied to the quantitative analysis of single stem cells in other adult and developing organs potentially leading to new discoveries on stem-cell properties and regenerative potential.

Chapter 5

Node-pore sensing

5. 1 Introduction

This chapter introduces node-pore sensing, which enhances the detection capabilities of RPS, as outlined in Chapter 2 [60]. Commercial Coulter counters can detect normalized current pulses ($|\Delta I|/I$) corresponding to a particle-to-pore volume ratio $V_{\text{particle}}/V_{\text{pore}} \sim 1.6 \times 10^{-5}$ when a dynamic aperture range of 64000:1 by volume is employed (Multisizer 4 Coulter Counter). On-chip RPS devices [61] are even more sensitive, with the state-of-the-art capable of measuring $|\Delta I|/I$ as low as $V_{\text{particle}}/V_{\text{pore}} \sim 4 \times 10^{-6}$. Ultimately, the signal-to-noise ratio (SNR) (defined as $|\Delta I|/I_{RMS}$ [62], where I_{RMS} is root-mean-square current noise), is the limiting factor to sensitivity, and even the use of sophisticated signal amplification and noise filtering is insufficient for lower $V_{\text{particle}}/V_{\text{pore}}$ ratios. Detecting nanoscale particles therefore becomes challenging and requires $V_{\text{particle}} \sim V_{\text{pore}}$ for sufficient SNR.

As there is a driving interest to measure single molecules of DNA for sequencing and to detect and enumerate HIV in human plasma for improved disease detection and monitoring, methods for fabricating smaller, more definable pores have grown more sophisticated: from utilizing high-energy nuclear particles to irradiate a plastic sheet that is then etched [11], to employing naturally-occurring or genetically-modified biological proteins [63, 64] such as alpha-hemolysin [65-71], to creating hybrid [72, 73] or solid-state pores [74-77] using electron-beam lithography and atomic-layer deposition, to directly employing carbon nanotubes [78-80]. Although the resulting pores have successfully measured nanometer-sized particles, the fact that V_{particle} needs to be equivalent to V_{pore} places a major restriction on the type of sample that can be measured. The sample must consist of a particles that are fairly uniform in size or else clogging of the pore would occur. Larger-sized pores could be used to screen a population of particles heterogeneous in size (e.g. ranging in size from nanometers to several microns), but SNR would far be too low to detect the nanometer-scaled particles.

We address these current limitations of RPS with NPS. As described in Chapter 2, by modifying the geometry of our sensors so that there is a sequence of nodes along the channel (Fig. 5.1), we can achieve distinct electronic signatures that can be easily distinguished within the measured noise. An enhanced fast Fourier transform (FFT) power spectra for rapid detection of the electronic signature can be easily accomplished. As we show here, NPS achieves high dynamic range such that Vpore >> V particle and detection is easily accomplished. We demonstrate the power of NPS by detecting HIV viral particles in human plasma.

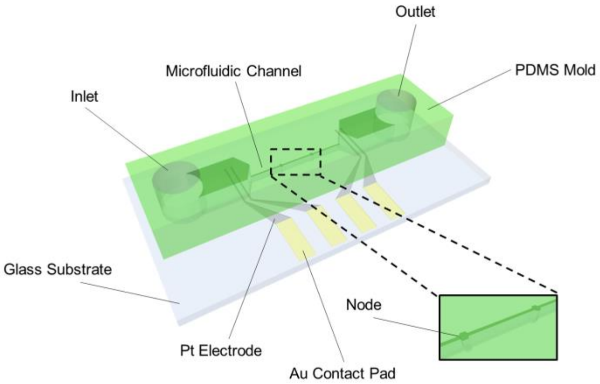

Fig. 5.1: Schematic of the node-pore sensor platform. The node-pore consists of a PDMS mold bonded to a glass substrate with Pt electrodes and Au contact pads that enable a four-terminal measurement of the electrical current across the pore. The device consists of two reservoirs, cored with entry and exit ports, connected by a small channel, i.e. pore. Magnified view: In this particular node-pore sensor design, the pore is segmented into three regions, separated by two nodes of larger cross-sectional area than the rest of the pore.

5. 2 Experimental Methods

5.2.1 Platform design

Fig. 5.1 shows an NPS device created with soft lithography. Like our RPS devices, the NPS device consists of a PDMS mold that is bonded to a glass substrate with pre-defined Pt electrodes and Au contact pads. The mold has two reservoirs that are connected by a single microfluidic channel (the “pore”). In direct contrast to standard RPS pores, the NPS pore is segmented by a series of nodes. Because of our use of standard lithography as detailed in Chapter 3, we have extensive flexibility and control to include as many nodes, spaced as close or as far apart, as are advantageous for measurements.

5. 3 Results

5.3.1 Versatility of design and signal measurements

To demonstrate the unique electronic signatures that our node-pores produce, we show how the electrical current pulse generated by a 15.45 µm polystyrene colloid (Bangs Laboratories, Inc.) transiting a node-pore changes with an increasing number of nodes. Fig. 5.2A (left) is a fluorescence image of a conventional pore (25 µm x 25 µm x 800 µm, H x W x L) and the corresponding electrical current pulse measured (right). As expected, the pulse has a well-defined square shape that is typically recorded in standard RPS measurements. In contrast, Fig. 5.2B (left) shows a pore (25 µm x 20 µm x 2400 µm, H x W x L) that has two, equally-spaced 50 µm-wide nodes and the corresponding pulse produced (right). Unlike the pulse in Fig. 5.2A, this pulse is clearly modulated. As the colloid enters the node-pore, the electrical current initially drops from the baseline as expected. When the colloid enters the first node, however, the electrical current rises, only to drop again once the colloid exits. This rise and fall in electrical current is repeated as the colloid enters and exits the next node. Finally, when the colloid exits the pore, the electrical current returns to the baseline value. The electrical current modulation we observe is a hallmark of all node-pores. Fig. 5.2C shows the electrical current pulse recorded when a pore with eleven equally-spaced nodes is employed, and Fig. 5.2D, when a pore has seven variably-spaced nodes. In each case, the electrical current modulation is clearly identifiable and reflects the number and spacing of the nodes in a pore. Thus, flexibility in device fabrication allows for variation in the number of nodes and their spacing, offering design versatility in NPS.

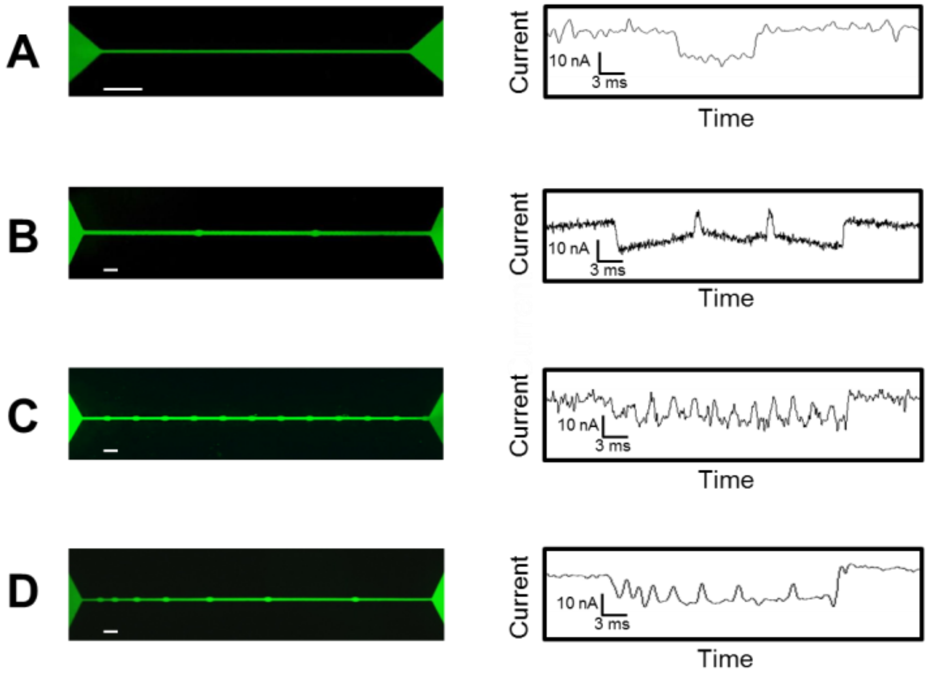

Fig. 5.2: Node-pore designs and measurements. Scale bar, 100 µm. (A-D) Fluorescence images of various pore designs (left) and the electrical current pulses produced when a 15.45 µm colloid transits each pore (right). (A) A conventional pore without nodes. (B-D) Node-pore sensors with two (B) and eleven (C) equally-spaced nodes, and seven variably-spaced nodes (D). Distinct electrical current modulation can be detected due to the presence of nodes.

5.3.2 Detection capabilities for heterogeneous populations

Because the unique electronic signatures produced by node-pores are easily identifiable, SNR becomes far less of an issue than with a standard pore in RPS. Even with SNRs << 1, signals within noise can be extracted using simple low-pass filtering and identified by their unique signature. With a single, microscale pore (8 µm x 10 µm x 500 µm, H x W x L) with four nodes that are equidistant apart (Fig. 5.3A), we can measure colloids ranging from 50 to 4900 nm in size

(Fig. 5.3B-E). While the electrical current pulse produced by the passage of the smaller colloids is difficult to distinguish from the baseline electrical current, the unique modulation of the electrical current pulse in the low-pass filtered signal makes the signature readily identifiable for detection (Fig. 5.3E). By designing pores with patterned node arrangements and by screening samples at a specific flow rate, the current-modulated pulse can be predicted and identified. Utilizing this particular strategy, we are able to screen successfully 50 nm colloids with the large micron-sized pore shown in Fig. 5.3A. Furthermore, $V_{\text{particle}}/V_{\text{pore}} \sim 1.2 \times 10^{-9}$, which to our knowledge, is the lowest ever recorded by an RPS-based system.

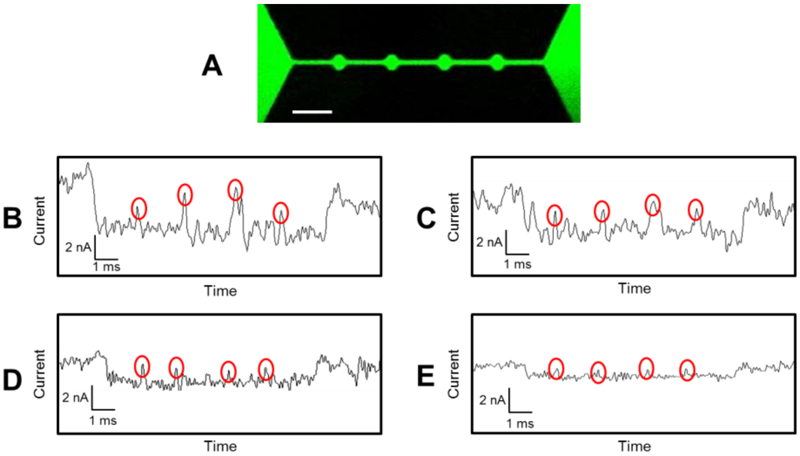

Fig. 5.3: Detection capabilities of a four-node device with varying sized colloids. Scale bars, 100 um. The pore size used is 8 µm x 10 µm x 500 µm, H x W x L. (A) Fluorescence image of the device. (B-D) Representative electrical current pulse of a 4900 nm (Interfacial Dynamics Corp.) (B), 930 nm (Interfacial Dynamics Corp.) (C), 500 nm (Polysciences, Inc.), (D), and 50 nm (Polysciences, Inc.) (E) colloid traversing the node-pore after applying a low-pass filter. Four distinct peaks (red ovals) within each pulse correspond to the colloid traveling through the individual nodes.

5.3.3 Fast Fourier transform testing

The node spacing in a pore provides a unique ability to utilize its spatial geometry to translate measured signals into an FFT power spectrum for quick detection analysis. The steps used in data translation are outlined in Fig. 5.4. We demonstrate FFT analysis capabilities by employing a specifically designed pore (18 µm x 20 µm x 2400 µm, H x W x L) that has two 50 µm-wide nodes that are 100 µm apart from one another, a 400 µm-long node "spacer", and two additional 50 µm-wide nodes, 500 µm apart (Fig. 5.5A). The electrical current pulse produced when a 15.45 µm colloid transits the pore (Fig. 5.5B) has two distinguishable signatures reflecting the different geometric spacing of the nodes. The associated FFT spectrum (Fig. 5.5C) displays both high frequency (f_{high}) and low frequency (f_{low}) peaks corresponding to the electronic signatures produced by the 100 µm node-spacing and 500 µm node-spacing segments of the pore, respectively. Node/pore combinations thus translate spatial frequencies directly into measurable temporal frequencies that can be directly detected and analyzed. Therefore, a single pore with a specific number of nodes optimized to enhance the corresponding FFT power spectrum has improved detection capabilities. This unique FFT analysis allows for NPS to utilize FFT detection algorithms for data extraction, which could ultimately improve data processing times.

.

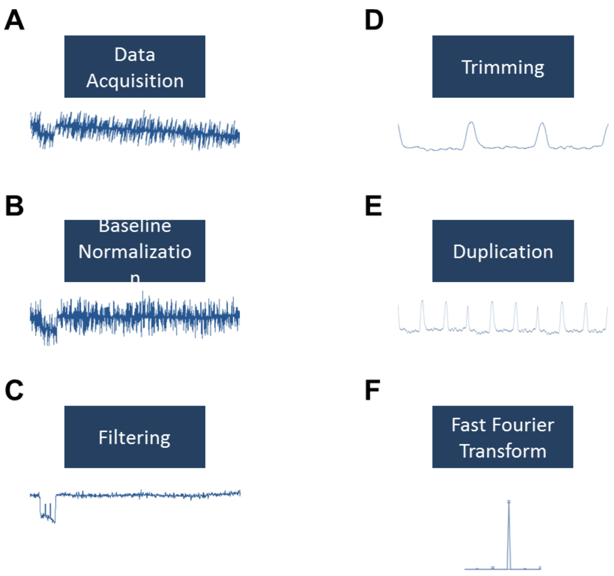

Figure 5.4: Detection scheme for applying fast Fourier transform (FFT) analysis. (A) Image of raw data during data acquisition. (B) Image of data after normalization to a baseline fit. (C) Data after a low-pass filter has been applied. (D) Data after regions of interest are identified and trimmed using derivative cutoff detection. (E) Duplication of the trimmed data prior to FFT analysis. (F) Calculation of the FFT of the duplication data.

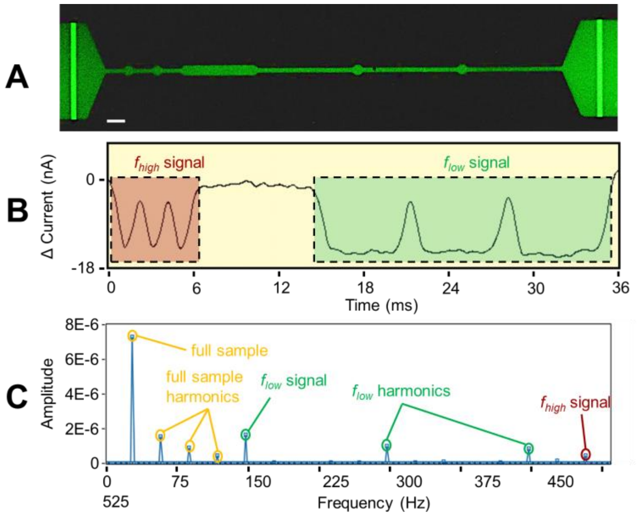

Fig. 5.5: Frequency analysis using a pore with two sections with different node spacing. Scale bar, 100 µm. (A) An image of an 18 µm x 20 µm x 2400 µm (H x W x L) pore with two 50 µm-

wide nodes that are 100 µm apart from one another, a 400 µm-long node “spacer”, and two additional 50 µm-wide nodes, 500 µm apart. (B) The electrical current pulse produced as a 15.45 µm colloid travels through the device. The high (shaded in red) and low (shaded in green) frequency, f_{high} and f_{low}, correspond to the sequence of nodes in the device. (C) The fast Fourier transform frequency spectrum of the total signal after ten duplications of the data (Fig. 5.4E).

5.3.4 Viral detection

Using the same microscale four-node pore shown in Fig. 5.3, we detected HIV particles, whose size range from 100 to 200 nm in diameter [86, 87] depending on viral maturity. In three experiments, we screened 50 nL of human plasma containing 100,000 copies/mL of a replication-incompetent strain of HIV (8E5 LAV Subtype B, SeraCare Life Sciences). As a control, we screened human plasma with no viral content. Fig. 5.6A shows a representative electrical current versus time trace we obtained when we measured the HIV-positive human plasma sample. As shown, there are two distinct modulated electrical current pulses with strikingly different magnitudes. Reference colloids of known size were measured with the same four-node device and their normalized electrical current-pulse magnitudes, i.e. $|\Delta I|/I$, were used to determine the size of the particles in transit. The cutoff frequency used for detecting signals can be optimized to reduce noise while still retaining the overall signature of the measurement, as outlined in Fig. 5.7.

The larger of the two pulses shown in Fig. 5.6A is a particle >1 µm and corresponds to fibrin in human plasma. The smaller pulse, present only in the HIV-positive human plasma sample and not in the control, corresponds to an HIV particle of size 140 nm. The particle size distribution for all our experiments is shown in Fig. 5.6B-E. We find that the number of viral particles detected per volume sampled is in agreement with the expected number given the concentration of HIV in each sample screened. Thus, our microscale node-pore in which $V_{\text{particle}} << V_{\text{pore}}$ is highly accurate in measuring viral particles without the need for sample preparation or the use of nanoscale fabrication. Furthermore, its large cross-sectional area makes the node-pore much less susceptible to clogging as compared to much smaller RPS-based viral sensors [8-10], making NPS appropriate for determining particle concentrations in heterogeneous samples.

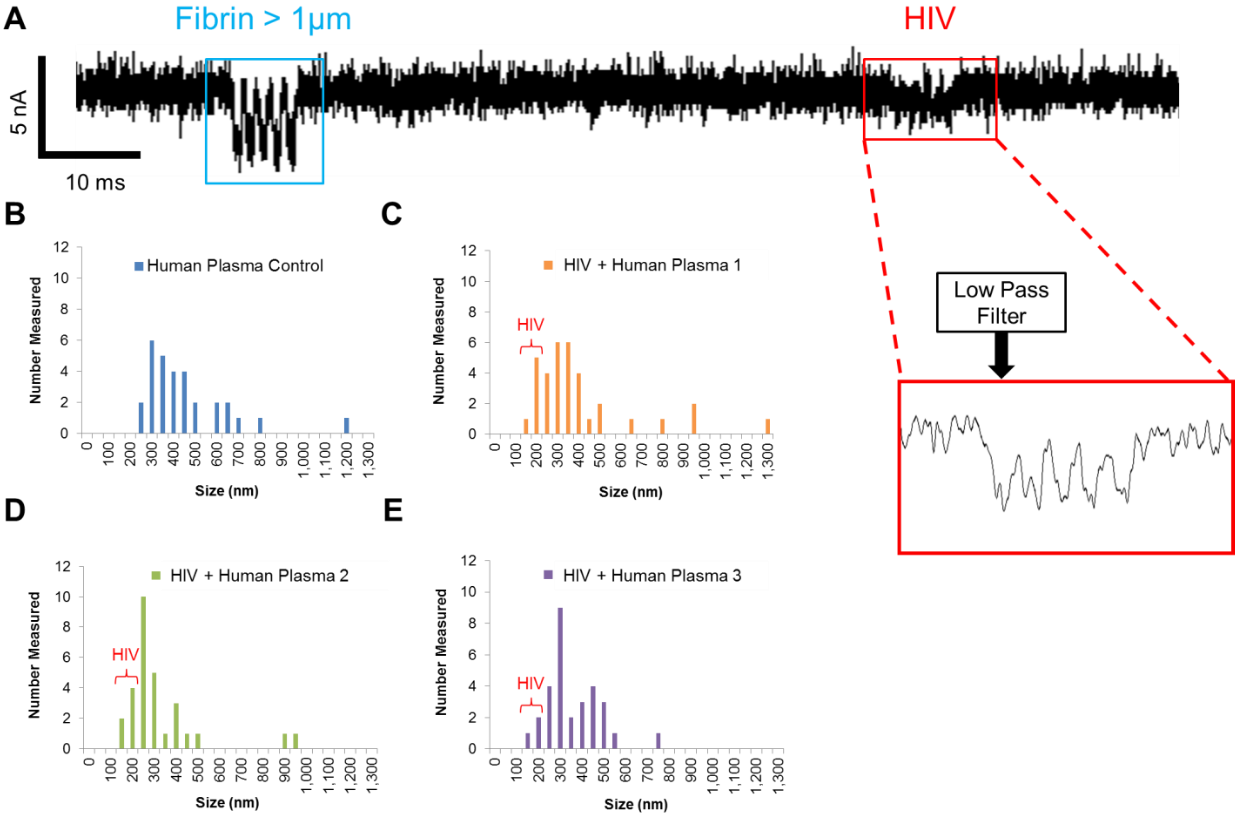

Fig. 5.6: HIV detection. (A) Representative electrical current vs. time trace of a sample of human plasma spiked with HIV at 100,000 copies/mL. A large-sized particle, e.g. fibrin (blue box), is easily detected. After applying a low-pass filter (cutoff ~1500 Hz), a nanoscale HIV particle (magnified red box) is readily apparent. (B) Size distribution of particles detected after screening 50 nL of human plasma without HIV. (C-D) Particle-size distribution of three 50 nL samples of human plasma with HIV. Particles with size ranging from 100-200 nm are HIV. Particle concentrations can be determined from these distributions. All particle sizes are determined by the magnitude of the normalized electrical current, $|\Delta I|/I$, as described in the ESI.

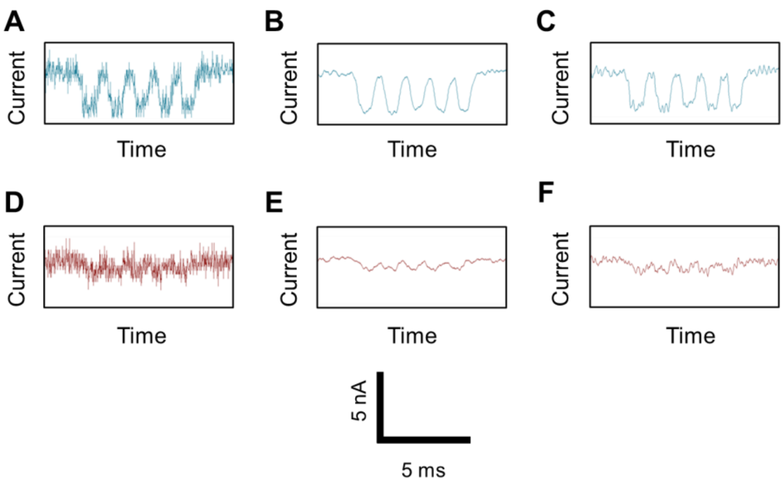

Figure 5.7: Low-pass filtering of measurement signal. Measurements of particles in human plasma sample transiting a (8 µm x 10 µm x 500 µm, H x W x L) four-node pore. Electrical current vs. time traces of a fibrin particle (A) and HIV (D) before filtering. (B) and (E) show the signals after a low-pass filter with a cutoff frequency of 1500 Hz has been applied. (C) and (F) show the signals after applying a cutoff frequency of 500 Hz to the original signal.

5.3.5 Discussion

Unlike commercial Coulter counters, the node-pores we have developed enable one to perform sensing with unprecedented dynamic range, flexibility, and sensitivity, i.e. $V_{\text{particle}}/V_{\text{pore}}$. Because node-pores have a large dynamic range, we can measure nanometer-sized particles without extraordinary effort, i.e. optimizing aperture size or using multiple apertures for detection is not necessary as is for commercial Coulter counters. In comparison with other on-chip RPS-based devices, including those we have previously developed and discussed in Chapters 2 and 4 [4, 88-91], node-pores distinguish themselves in a number of ways. First, high signal amplification is not needed. Second, complicated and expensive nanofabrication procedures, such as atomic-layer deposition, electron-beam lithography, and incorporation of naturally occurring pores, are not needed to measure at the nanoscale. With regard to processing volume, we have employed flow rates > 10 µL/min without loss of signal detection or resolution. Throughput of our node-pores is limited by the fact that having multiple particles traversing the pore simultaneously presents signal identification complications; however, multiplexing strategies such as integrating parallel-sensing arrays [91, 92] could be utilized to boost processing efficiency, resulting in an extraordinarily versatile high-throughput sensing platform.

While viral detection using RPS has been accomplished with nanometer-scaled pores [8-10], the ability to detect viral particles directly in human plasma has been a major challenge due to the inability of nanopores to screen fibrin and other aggregate components in blood plasma. Because of their applicability for screening heterogeneous populations, node-pores could be utilized at the point-of-care, determining viral particle counts to monitor disease progression and response to therapy. Node-pore viral counts would make rapid, low-cost HIV testing accessible in areas with limited medical facilities. Beyond HIV detection, node-pores, with its ease in manufacturing, dynamic range, and accuracy in detection, could be utilized in a number of diverse medical, environmental, and industrial applications, including screening bacterial and other viral populations, assessing water quality and determining contaminants, and monitoring protein aggregation in pharmaceutical processes.

In summary, we have created an extremely robust, flexible, and powerful screening platform. Chapter 6 and 7 focus on our work modifying node-pores to probe several particle-pore interactions in a single device, enabling us to take advantage of transit-time measurements corresponding to different segments of the pore, thereby adding a new dimension to particle characterization.

Chapter 6

Leukemia Cell Line Multi-marker Screening

6. 1 Introduction

This chapter details the development of NPS into a multi-marker screening platform [93], for screening single cells for cell size and *multiple* cell-surface epitopes, simultaneously. As described earlier in Chapters 3 and 4, we still employ protein immobilization; however, in this particular case, the individual segments between the nodes are functionalized with different antibodies corresponding to distinct cell-surface antigens. Cells whose antigens can interact specifically with the functionalized antibodies in a particular segment travel more slowly through that section of the channel than through an isotype-control segment. Surface-marker identification is thus accomplished by comparing transit times within the modulated pulse the node-pore device produces, as explained below.

We demonstrate proof-of-principle by screening cells from two different established acute promyelocytic leukemia (APL) human cell lines—NB4 and AP-1060—for myeloid antigens, CD13, CD14, CD15, and CD33, simultaneously. NB4 cells were established from a patient who was resistant to all-*trans*-retinoic acid (ATRA) [94]. These cells, however, remain sensitive to the induction of terminal neutrophilic differentiation by ATRA [94]. In contrast, AP-1060 cells were established from a patient who was resistant to both ATRA and arsenic trioxide (ATO) [95]. While both CD13 and CD33 are expressed in the majority of NB4 and AP-1060 cells, expression of CD14 is absent. Moreover, CD15 is expressed moderately in NB4 cells and only weakly in AP-1060 cells. In addition, we show NPS's ability to distinguish two different cell types of similar size—AP-1060 and NALM-1—in a mixture solely by screening for surface markers, CD13 and HLA-DR. NALM-1 cells were established from a patient with chronic myeloid leukemia who was in lymphoid blast crisis [96] and are similar in size to AP-1060 cells. However, while AP-1060 cells are HLA-DR-/CD13+ [95], NALM-1 cells are HLA-DR+/CD13-[97]. We also show that patterning the same antibody in different regions of the node-pore can enhance the surface-marker detection capabilities of the NPS sensor. We validated our technique by comparing our results with the gold standard, flow cytometry (FCM).

6. 2 Experimental Methods

6.2.1 Platform design

Our multi-marker screening method is based on performing NPS, and as such, we utilize the same standard microfabrication techniques to manufacture the overall NPS device (Fig. 6.1A and described in Chapters 3 and 5). The major difference from our earlier experiments is that we immobilize several different proteins onto the glass substrate of our device. To accomplish this patterning, we employ soft lithography to create a set of temporary channels whose individual widths are the same size as the segment lengths between the nodes. We align these channels transverse to the direction of the eventual node-pore to thus functionalize each segment between the nodes with a saturating concentration of either a specific antibody corresponding to a particular cell-surface antigen or an isotype-control antibody (Figs. 6.1B-C). We subsequently align the node-pore on top of, and clamp to, the prepared substrate (Figs. 6.1D-E).

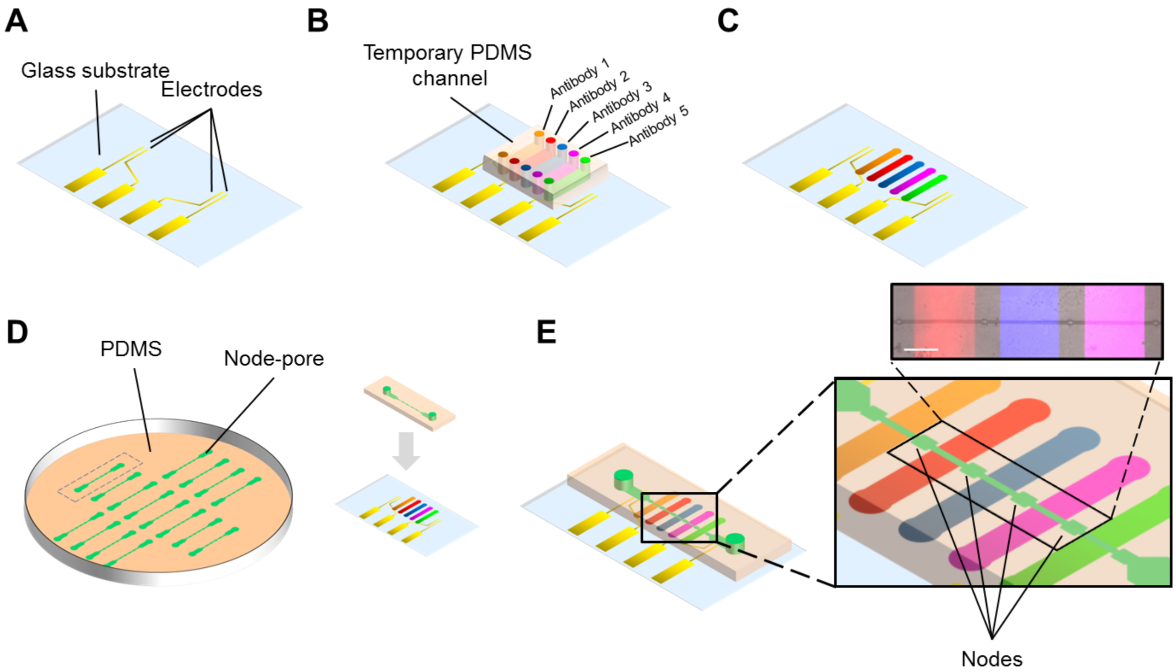

Fig. 6.1. Functionalized node-pore device assembly. (A) The basic node-pore platform consists of a glass substrate with pre-defined electrodes. (B) To functionalize the node-pore device with antibodies, a temporary PDMS mold embedded with *N* individual microchannels, corresponding to *N* functionalized segments (five are shown here), is positioned onto the substrate transverse to the direction of the ultimate node-pore channel. APTES, Sulfo-EGS, Protein G, and antibodies are injected and incubated into the channels to functionalize and pattern the antibodies onto the substrate (C). (D) A slab of PDMS embedded with the node-pore is aligned directly on top of the functionalized substrate such that the channel is perpendicular to the patterned antibodies. (E) The completed node-pore device has functionalized antibodies in the channel between the nodes. (inset) A pseudocolored (ImageJ) fluorescence image of three different patterned antibodies (PE Mouse IgG1, κ Isotype Control (200 µg/mL), Brilliant Violet 421 Rat IgG1, κ isotype control (50 µg/mL), Alexa Fluor 647 Mouse IgG2b, κ Isotype Control (500 µg/mL), all from Biolegend) in a completed node-pore. Scale bar, 500 µm.

6.2.2 Cell culture and FCM of cell lines

Cell culture details are found in Chapter 9: Protocols. FCM preparation of the cell lines involved primary staining with unconjugated antibodies and secondary staining with fluorescent antibody. Detailed FCM preparation of the cell lines can also be found in Chapter 9: Protocols.

6. 3 Results

6.3.1 Cutoff determination using isotype control labeled devices

For all screening experiments, we used a device that was 18 µm x 18 µm (H x W) with five 1150-µm long segments separated by four nodes, each 58-µm wide and 50-µm long. To determine whether a cell interacted specifically with one of the functionalized segments, we normalized the cell's transit time in that particular segment, τ_{specific}, with respect to its transit time through the isotype control, $\tau_{\mathrm{norm}} = \tau_{\mathrm{specific}}/\tau_{\mathrm{isotype}}$. To account for the inherent variability in non-specific interactions between cells and the functionalized isotype antibodies, we conservatively defined positive expression of an antigen if $\tau_{\mathrm{norm}} > 1+2\sigma_{\mathrm{isotype}}$. Here, $\sigma_{\mathrm{isotype}}$ is the standard deviation of the normalized transit time values we measured when we screened a sample of cells with a node-pore consisting of only multiple isotype-control segments, as shown in Fig. 6.2. In this case,

$$\tau_{\mathrm{norm}} = \tau_{\mathrm{IgG1,\ segment\ 1}} / \tau_{\mathrm{IgG1,\ segment\ 2}} \qquad \text{Eq. (6.1)}$$

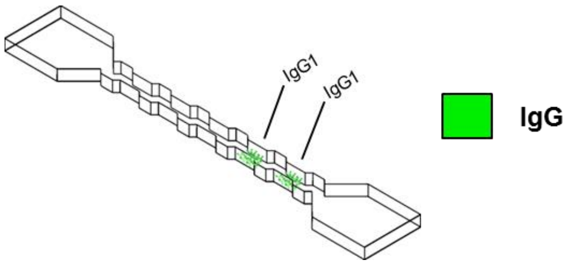

Fig. 6.2: Isotype control node-pore testing configuration for transit-time cutoff determination. Schematic of a four-node-pore with two consecutive sections functionalized with IgG1 isotype control antibody. The actual device was 18 µm x 18 µm (H x W) with five 1150-µm long segments separated by four nodes, each 58-µm wide and 50-µm long.

Normalized transit-time distributions of NB4, AP-1060, and NALM-1/AP-1060 mixed samples are shown in Fig. 6.3. From these distributions, $\sigma_{\mathrm{isotype}}$ values were calculated and threshold cutoff values were found (1.0228, 1.0250, and 1.0229, for NB4, AP-1060, and NALM-1/AP1060, respectively), as denoted with a vertical dashed line.

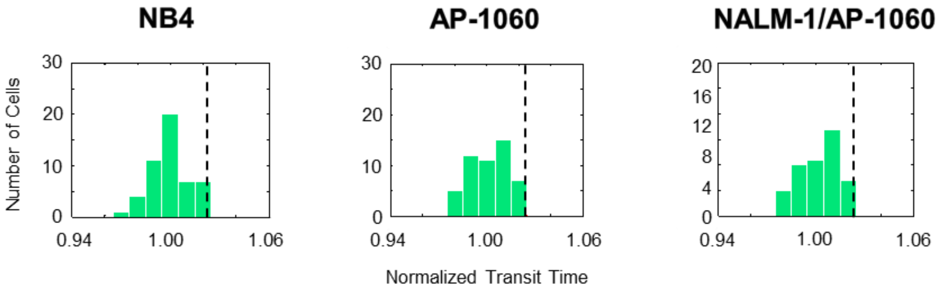

Fig. 6.3: Isotype control node-pore testing with transit-time cutoff determination. Data was obtained by screening NB4 cells (10^6 cells/mL), AP-1060 (2 x 10^6 cells/mL), and a 1:1 mixture of NALM-1 : AP-1060 cells (10^6 cells/mL) with the prepared IgG1 node-pore devices. Normalized transit-time distributions of the NB4, AP-1060, and mixed NALM-1 : AP-1060 cells (top row), with the positive expression cutoffs, corresponding to $1+2\sigma_{\text{isotype}}$, indicated by the vertical dashed lines.

6.3.2 Sizing of NB4, AP-1060, and NALM-1/AP-1060 cells

In the same tests that we used to determine the isotype-control normalized transit-time cutoffs, we also determined the size distributions of each sample (Fig. 7.4). We verified that the cell populations had a variation in cell size and all overlapped with one another such that size alone could not be used to distinguish these cell lines.

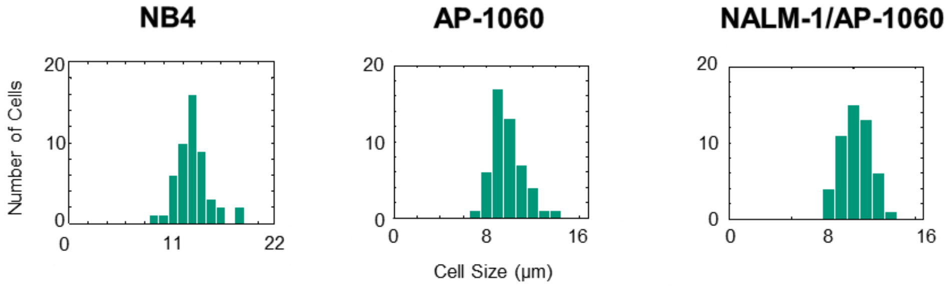

Fig. 6.4: Sizing of NB4, AP-1060, and NALM-1/AP-1060 samples. Size distributions of each sample obtained from NPS are shown.

6.3.3 Simultaneous Screening of Four Surface Markers on NB4 and AP-1060 Cells

Fig. 6.5B shows a representative electrical current vs. time pulse that was produced when a single NB4 cell traversed the prepared node-pore. The pulse is clearly modulated, consisting of five sub-pulses corresponding to the cell transiting the five different segments of the node-pore. The transit time of each sub-pulse is as indicated: τ_{CD13}, τ_{CD14}, τ_{CD15}, τ_{CD33}, and τ_{IgG1}. Fig. 6.5C shows the individual phenotypic profiles of ten NB4 and AP-1060 cells. Each dashed box corresponds to a single cell and contains the normalized transit times corresponding to the markers screened ($\tau_{\text{CD13, norm}}$= orange, $\tau_{\text{CD14, norm}}$ = red, $\tau_{\text{CD15, norm}}$ = blue, $\tau_{\text{CD33, norm}}$ = pink). The dashed green line corresponds to the cutoff value, $1+2\sigma_{\text{isotype}}$. Thus, the phenotype of NB4 Cell 1 is CD13+/CD14-/CD15+/CD33+, and Cell 10 is CD13+/CD14-/CD15-/CD33+. Likewise, AP-1060 Cell 2 is CD13+/CD14-/CD15-/CD33+, and Cell 7 is CD13-/CD14-/CD15-/CD33+. The normalized transit-time distributions for all cells measured for each marker screened is also shown in Fig. 6.5C. With our NPS screening method, we found that most NB4 cells express CD13 and CD33 (92% and 83%, respectively), whereas only some express CD15 (45%), and few express CD14 (5%). Similarly, we found that most AP-1060 cells express CD13 and CD33 (86% and 76%, respectively), far less express CD15 (21%), and few express CD14 (3%). These surface-marker expression trends are consistent with previous reports [94, 95] and our own FCM results (Fig. 6.5D).

Cells were stained for FCM using primary antibody and secondary Alexa Fluor 488 Goat Anti-Mouse IgG antibody. The specific protocols can be found in Chapter 9: Protocols. Results for FCM on NB4 and AP-1060 cells can be found in Figs. 6.6 and 6.7, respectively. Overall, 99%, 2%, 55%, and 97% of NB4 cells expressed CD13, CD14, CD15, and CD33, respectively. 92%, 1%, 16%, 97% of AP1060 cells expressed CD13, CD14, CD15, and CD33, respectively.

We employed a χ^2 test,

$$\chi^2 = \sum_{i=1}^{n} \frac{\left(O_i - E_i\right)^2}{E_i} \qquad \text{Eq. (6.2)}$$

to determine whether there were any statistically significant differences between NPS and FCM results. The observed values, O_{i}, were the number of cells NPS detected as positive for a particular surface marker in a sample. The expected values, E_{i}, were the number of cells expected to be positive in the same sample based on the percentages FCM obtained for each surface marker; these percentages were applied to the total number of cells screened with the NPS deviceWith a p-value of 0.05, we found that, with the exception of our AP-1060 CD14 and CD33 results, there were no statistically significant differences between the results obtained from NPS and those of FCM. Minor discrepancies between the two may be due to the small sample sizes NPS screened (less than 150 cells vs. greater than 15,000 cells for FCM), and/or to the fact that some cells did not have a sufficient number of transient interactions to lead to a detectable transit-time delay in NPS. For CD14, the discrepancy between the two methods was due to the fact that only a small number of cells were expected to express this marker; even minor differences in detection (3% in NPS vs. 1% in FCM) would result in a greatly exaggerated χ^2 value. For CD33, the larger discrepancy may be due to weak transient interaction between antibody and antigen in the node-pore vs. the permanent binding between the two that occurs during incubation for FCM.

Table 6.1 shows the χ^2 values of the NB4 and AP-1060 samples. For a p-value=0.05, χ^2=3.841. Thus, the only statistically significant differences between FCM and NPS results were those corresponding to the screening of CD14 and CD33 on AP-1060 cells

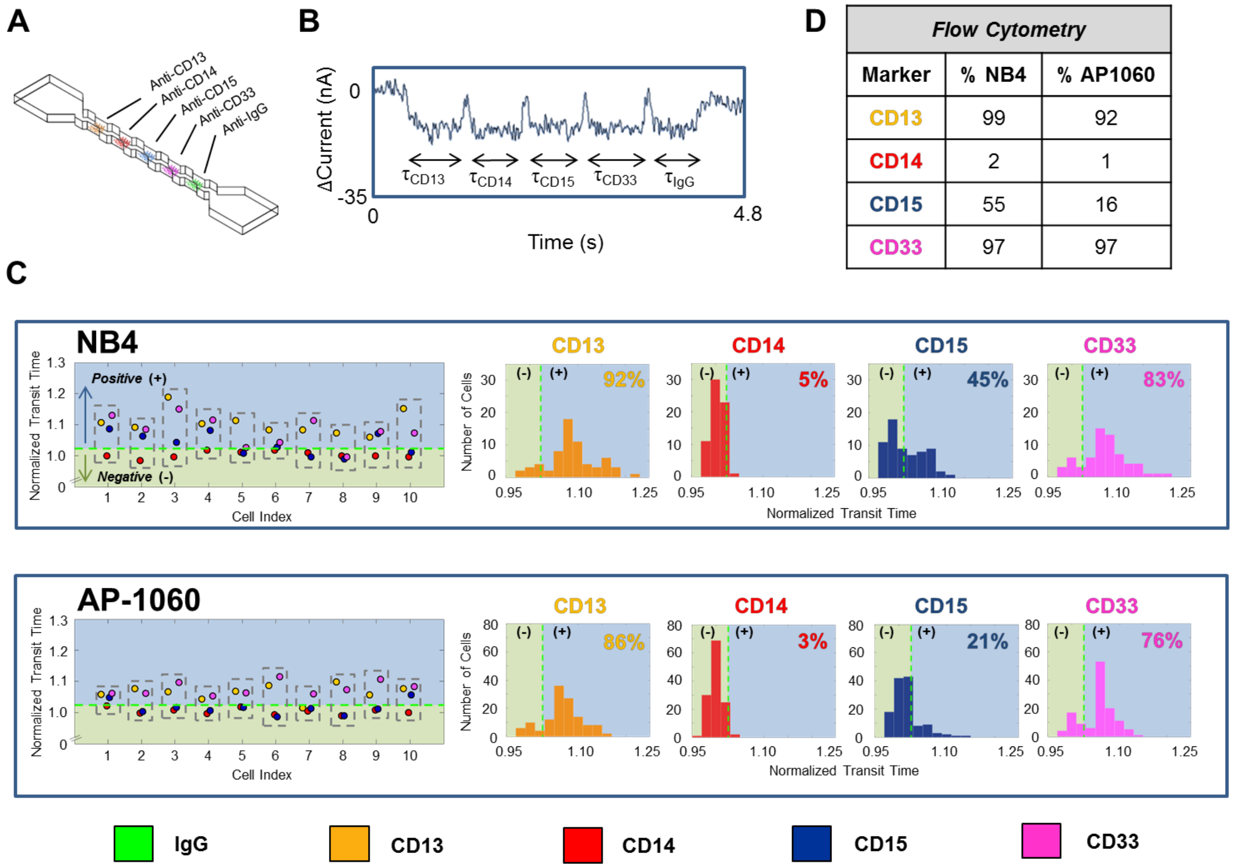

Flow Cytometry		
Marker	% NB4	% AP1060
CD13	99	92
CD14	2	1
CD15	55	16
CD33	97	97

Fig. 6.5: Surface-marker profiling of leukemia cells using NPS. Acute Promyelocytic Leukemia (APL) human cell lines, NB4 and AP-1060, were screened for CD13, CD14, CD15, and CD33, simultaneously. (A) Schematic of the utilized node-pore device, which was functionalized with four specific antibodies (anti-CD13 Ab., anti-CD14 Ab., anti-CD15 Ab., and anti-CD33 Ab., all at a saturating concentration of 1 mg/mL) and an isotype control antibody (IgG1, 1 mg/mL). The device was 18 µm x 18 µm (H x W) with five 1150-µm long segments separated by four nodes, each 58-µm wide and 50-µm long. (B) A representative electrical current pulse caused by an NB4 cell transiting the node-pore device. The modulated pulse is due to the cell traveling through each segment of the node-pore. The width of each sub-pulse, indicated as τ_{CD13}, τ_{CD14}, τ_{CD15}, τ_{CD33}, and τ_{IgG1}, corresponds to the transit time of the cell through each segment. (C) Representative normalized transit times ($\tau_{\mathrm{norm}} = \tau_{\mathrm{specific}}/\tau_{\mathrm{IgG1}}$) of 10 NB4 cells and 10 AP-1060 cells and the resulting distribution for each marker screened. A cell is positive for a particular marker (CD13 = yellow; CD14 = red; CD15 = blue; and CD33 = pink) if τ_{norm} is greater than a threshold cutoff (denoted as a dashed green line and defined as $1+ 2\sigma_{\mathrm{isotype}}$, where $\sigma_{\mathrm{isotype}}$ describes the inherent variability in non-specific interactions between the cells and the functionalized isotype antibodies). Thus, NB4 Cell 1 is $\mathrm{CD13}^{+}/\mathrm{CD14}^{-}/\mathrm{CD15}^{+}/\mathrm{CD33}^{+}$, and AP1060 Cell 3 is $\mathrm{CD13}^{+}/\mathrm{CD14}^{-}/\mathrm{CD15}^{-}/\mathrm{CD33}^{+}$. A summary of cells positive/negative for each marker is shown in the normalized transit-time distribution. A total of 65 NB4 cells and 127 AP-1060 cells were measured. (D) FCM analysis of cells from the same population of NB4 and AP-1060 cells measured with the node-pore device. 15,000 NB4 cells and 35,000 AP-1060 cells were screened.

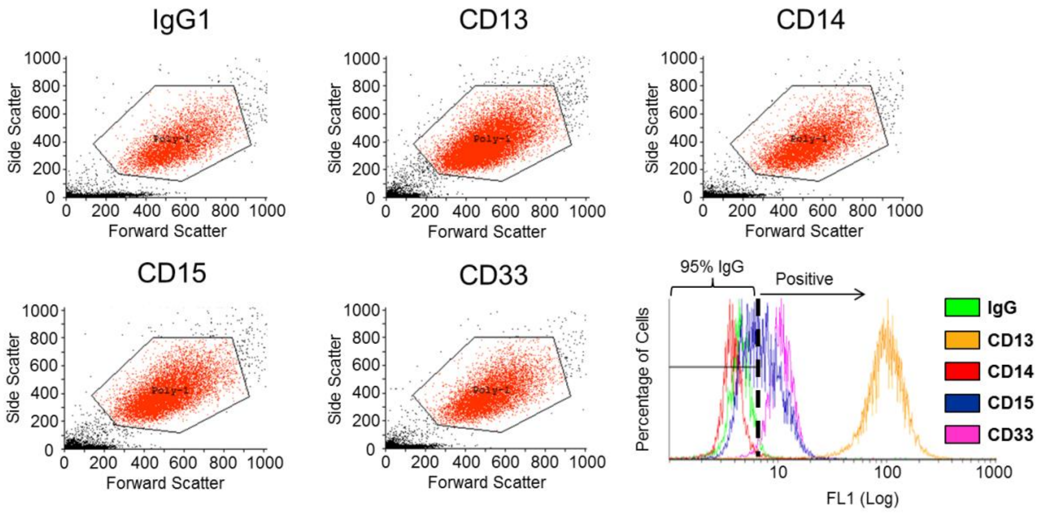

Fig. 6.6: FCM forward-scatter and side-scatter plots and an overlay fluorescence histogram of NB4 cells. Each sample was stained with a different primary antibody (IgG1, anti-CD13 Ab., anti-CD14 Ab., anti-CD15 Ab., or anti-CD33 Ab.) and then secondary antibody (Alexa Fluor 488 Goat polyclonal Secondary Antibody to Mouse IgG). A vertical dashed line indicates 95% of the IgG sample. Cells expressing more fluorescence than this cutoff value were determined to be positive for the particular surface marker.

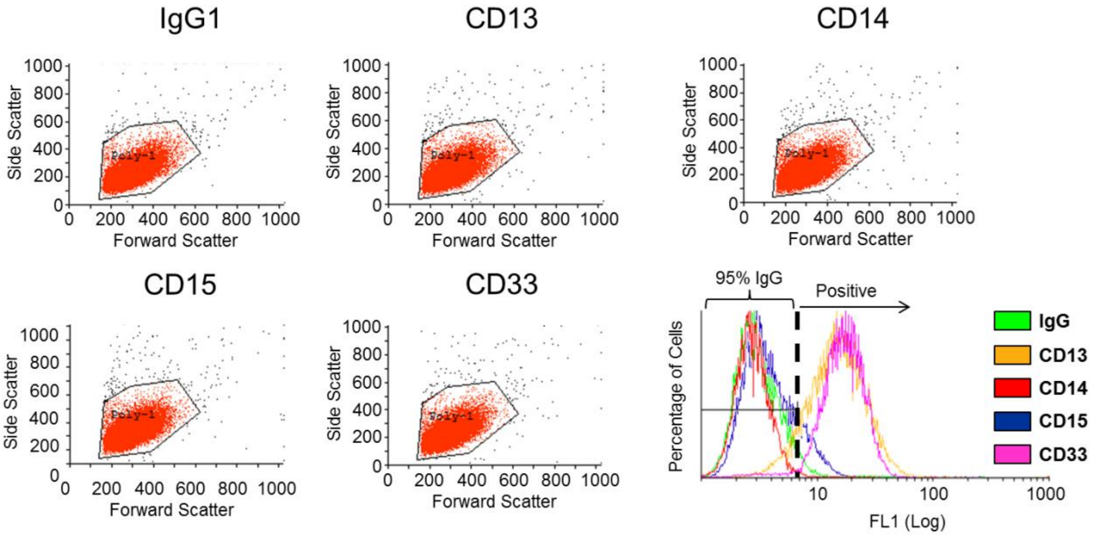

Fig. 6.7: FCM forward-scatter and side-scatter plots and an overlay fluorescence histogram of AP-1060 cells. Each sample was stained with a different primary antibody (IgG1, anti-CD13 Ab., anti-CD14 Ab., anti-CD15 Ab., or anti-CD33 Ab.) and then secondary antibody (Alexa Fluor 488 Goat polyclonal Secondary Antibody to Mouse IgG). A vertical dashed line is shown to indicate 95% of the IgG sample. Cells expressing more fluorescence than this cutoff value were determined to be positive for the particular surface marker.

Table 6.1. χ^2 **test comparing NPS with FCM for NB4 and AP-1060 cell lines.**

Surface Antigen	**NB4** χ^2	**AP-1060** χ^2
CD13	0.294	0.526
CD14	2.223	5.868
CD15	1.274	2.196
CD33	1.300	5.568
HLA-DR	N/A	N/A

6.3.4 Differentiating Mixed Populations and Including Redundancy for Higher Sensitivity in the Node-Pore

We screened a 1:1 mixture of AP-1060 cells and NALM-1 cells for HLA-DR and CD13 using a node-pore consisting of repeated segments of the same set of antibodies (i.e. anti-HLA-DR antibody and anti-CD13 antibody) (Fig. 6.8B). As shown above, NALM-1 cells are similar in size to AP-1060 cells. However, while AP-1060 cells are HLA-DR-/CD13+ [95], NALM-1 cells are HLA-DR+/CD13- [97]. We chose to employ a redundant-patterned node-pore to increase the sensitivity of our screening method. Using two segments functionalized with the same antibody, we increased the probability of transient interactions that could occur between the cell-surface antigen and that particular antibody.

The normalized transit times of representative cells from the screened mixture are shown in Fig. 6.8C. Using the same analysis as before, where positive expression for a marker corresponds to $\tau_{\text{norm}} > 1+2\sigma_{\text{isotype}}$, we find that in the first half of the device, 39% of the cells were HLA-DR+/CD13-, or NALM-1, and 44% were HLA-DR-/CD13+, or AP-1060. In contrast, in the second half of the device, only 32% of the cells were identified as NALM-1, and 41% as AP-1060 (Fig. 6.8D). The different percentages obtained by the two different halves of the device highlight the fact that some cells may not have had sufficient transient interactions to lead to a measurable change in transit time in a particular functionalized segment. By considering those cells that are negative for a particular marker in one section of the device but positive in the other redundant section as positive overall, we greatly increase the sensitivity and accuracy of our screening method: 41% are thus NALM-1 and 49% are AP-1060. These results are virtually identical to those we obtained by performing FCM on the same population of cells (Fig. 6.8A), showcasing our method's ability to distinguish two different subpopulations accurately in a sample even though the subpopulations overlap considerably in their size distributions.

Cells were stained for FCM using primary antibody and secondary Alexa Fluor 488 Goat Anti-Mouse IgG antibody. The specific protocols can be found in Chapter 9: Protocols. Results for NALM-1/AP-1060 mixed sample can be found in Fig. 6.9. In the mixed sample, 40% of cells expressed NALM-1 while 52% expressed CD13.

Table 6.2 shows the χ^2 values of the AP-1060/NALM-1 mixture sample. Again, for a p-value=0.05, χ^2=3.841. As shown by the lower χ^2 values, incorporating redundant antibody patterning can be used to increase sensitivity, greatly reducing the differences between the two methods.

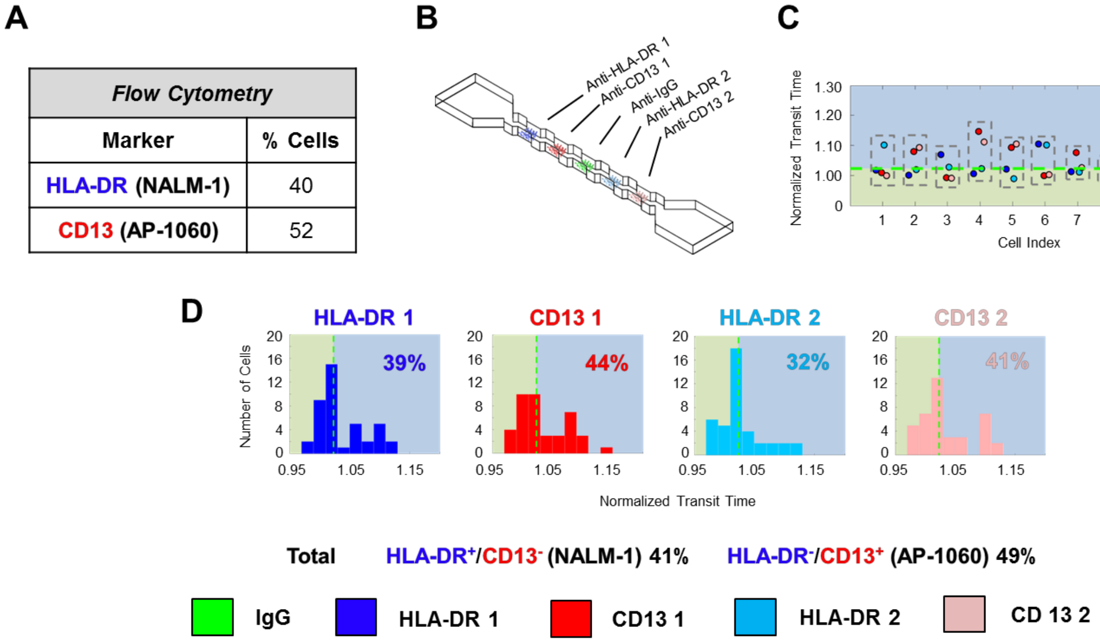

Flow Cytometry	
Marker	% Cells
HLA-DR (NALM-1)	40
CD13 (AP-1060)	52

Fig. 6.8: Analysis of a 1:1 mixture of AP-1060 : NALM-1 cells using a 4-node-pore device that has repeated regions of antibody functionalization. AP-1060 cells are HLA-DR-/CD13+, while NALM-1 cells are HLA-DR+/CD13-. (A) FCM analysis of the cell mixture confirmed the nearly 1:1 mixture of cells. (B) Schematic of the 4-node-pore device employed. The repeated patterning of the anti-HLA-DR Ab. and anti-CD13 Ab. combination on either side of the patterned IgG1 was included to increase the sensitivity of screening. All regions were functionalized with 1 mg/mL of antibodies. HLA-DR 1 (region 1) = blue; CD13 1 (region 2) = red, HLA-DR 2 (region 4) = light blue; and CD13 2 (region 5) = pink). (C) Representative normalized transit time of 10 cells from the mixed sample. As in Fig. 6.5, a cell is determined to be positive for a surface marker if its normalized transit time is greater than the IgG1 threshold cutoff, which is indicated as a green dashed line. Although HLA-DR-/CD13- in the first half of the device, Cell 1 is HLA-DR+/CD13- in the second half. We consider the cell to be overall HLA-DR+/CD13-. (D) Normalized transit-time distribution of each functionalized segment. A total of 41 cells were measured. By considering those cells like Cell 1, whose normalized transit time is above the threshold cutoff in at least one of the two similarly functionalized segments as positive for a particular surface-marker, the sensitivity of the overall device is greatly increased.

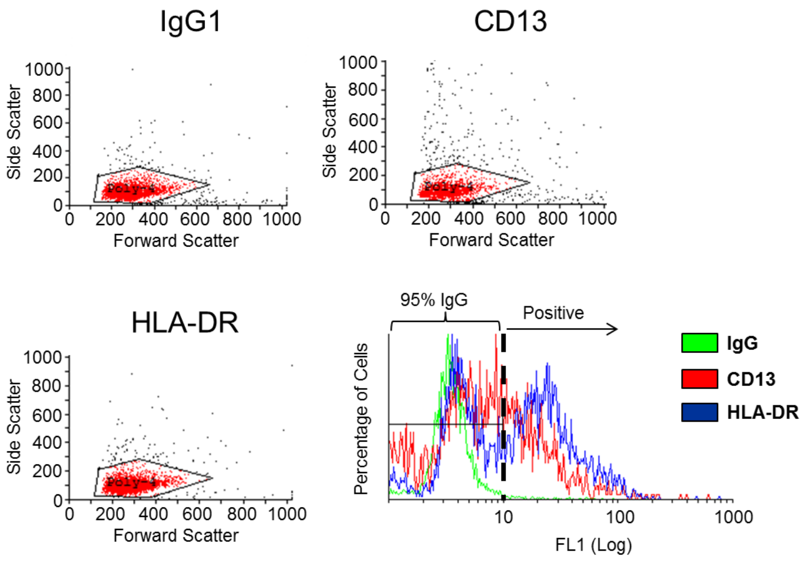

Fig. 6.9: FCM forward-scatter and side-scatter plots and an overlay fluorescence histogram of a 1:1 NALM-1/AP-1060 cell mixture. Each sample was stained with a different primary antibody (IgG1, anti-CD13 Ab., or anti-HLA-DR Ab.) and then secondary antibody (Alexa Fluor 488 Goat polyclonal Secondary Antibody to Mouse IgG). A vertical dashed line is shown to indicate 95% of the IgG sample. Cells expressing more fluorescence than this cutoff value were determined to be positive for the particular surface marker.

Table 6.2. χ^2 test comparing NPS with FCM for the AP-1060/NALM-1 mixed sample.

Surface Antigen	**AP-1060/NALM-1 Mixture χ^2**
CD13	0.0817
HLA-DR	0.220

6.3.5 Viability of cells after screening with NPS

To demonstrate that NPS does not damage cells during the screening process, we used Propidium Iodide (PI) to determine the number of dead cells post-screening. We collected AP-1060 cells from the outlet port of the node-pore devices after screening (Fig. 6.10A) and incubated these cells with PI solution (1.0 mg/mL, Life Technologies) for 10 minutes in a 1:100 PI : cell media volume ratio. We then used fluorescence intensity to identify dead cells (Fig. 6.10B). Of the 315 cells we analyzed, only 7 cells (i.e. 2.2%) showed high levels of fluorescence. Thus, greater than 97% of cells screened with the node-pore devices remained viable. As a control, we performed a viability test on cells that we did not screen with the node-pore devices. We found that 96% of these control cells remained viable, suggesting that the node-pore method does not damage cells during the screening process.

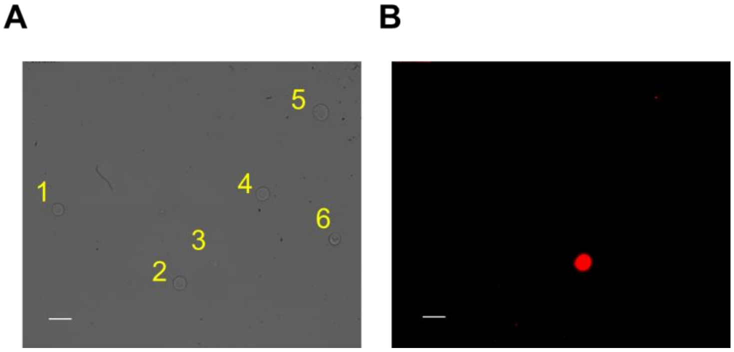

Fig. 6.10: Propidium Iodide testing for cell viability post screening with the node-pore. (A) Bright-field image of six AP-1060 cells that were collected from the output of a node-pore device and stained with PI. (B) Fluorescence image of the same 6 cells show that only cell 3 (red) had died; the rest remained viable after being screened in the node-pore device. Scale bar, 20 µm (A and B).

6.4 Discussion

NPS offers significant advantages over conventional microfluidics for screening surface antigens [18, 28, 98-100], as the technique enables screening simultaneously for multiple surface antigens on cells, and importantly, allows for the collection of viable, unlabeled cells for secondary analysis or culture, post-screening. As described in Chapter 4, our previous experiments [18, 25, 28, 101] used RPS single-pores for surface-marker screening, and these tests were limited to detecting only a single marker on a cell's surface. Furthermore, two different RPS pores, one functionalized with a specific antibody and the other with the isotype control, were necessary to screen for that single marker. NPS is transformative in its ability to screen several markers within a single assay while also allowing for intrinsic control comparisons within the same device. In the next chapter, we demonstrate the ability of NPS to screen complex samples, such as those typically found in medical samples for patients.

Chapter 7

Leukemia Patient Bone-Marrow Screening

7. 1 Introduction

This chapter describes the applicability of NPS as a screening tool for clinicians and elaborates on the benefits the method could provide in undeveloped areas of the world. A number of different cancers, including leukemia and lymphoma, are now considered treatable diseases with improved patient outcomes in countries with a robust healthcare infrastructure that can provide early detection, diagnosis, and continuous monitoring during therapy [102, 103]. In contrast, cancer, in general, is still a challenge to treat in developing countries with minimal healthcare resources [102-104]. The World Health Organization (WHO) has estimated that in 2008, 70% of the 7.6 million cancer-patient deaths worldwide occurred in developing countries [105]. Many of these deaths could have been prevented with early detection, diagnosis, and treatment, while the cancer was in its earliest stages. A lack of access to state-of-the-art diagnostic tools in developing countries, however, makes such detection and diagnosis nearly impossible. Patients often present with later stages of cancer, which can result in poor prognoses [104, 105]. There is a critical need for affordable, highly sensitive, user-friendly technologies for early cancer detection that could be applicable for widespread global-health use.

The need for more suitable diagnostic tools in resource-limited environments has led to emerging opportunities for microfluidic technologies [106, 107], which are ideal, given their low-cost, low-power requirement, and portable nature. Examples of microfluidic platforms that have been developed to detect and characterize cancer cells include a true miniaturization of fluorescence-activated-cell-sorting [108], dielectrophoretic cell characterization [109], aptamer-based cell capture [110-112], and immunoaffinity-based cell-capture [113-117]. While many of these platforms have demonstrated varying degrees of success, none have been capable of matching the power of multi-color FCM for characterizing, and subsequently identifying subpopulations of, cancer cells [118-120]. This core clinical diagnostic tool is critical to diagnosing hematologic malignancies, among other cancers, as FCM screens cells for multiple cell-surface epitopes simultaneously and identifies cellular sub-populations. Multi-color FCM is widely used in developed countries, but not so in low-resource settings, as the system is highly complex, expensive, and requires frequent calibration, a skilled technician for operation, and a highly trained pathologist for data interpretation [121, 122]. While able to address the cost and user-friendly issues that limit the utilization of multi-color FCM in low-resource settings, current microfluidic platforms are limited, themselves, by the number of parameters that can be screened. Moreover, many microfluidic technologies that incorporate either optical-sensing modalities or magnetic fields for separation require just as many manual sample-processing steps as multi-color FCM in terms of labeling cells with fluorophore-conjugated antibodies or antibody-coated magnetic beads. Likewise, platforms that are “label-free” are unable to identify cellular sub-populations with similar morphologies or physical properties (e.g. dielectric constants, cell size, etc.). Because an extensive panel of markers is required for diagnosing hematologic malignancies and distinguishing disease subtypes, current microfluidic platforms are thus far insufficient.

In this chapter, we demonstrate the value of NPS toward clinical use by screening primary human bone marrow samples from acute myeloid leukemia (AML) patients for CD13, HLA-DR, and CD34, as highlighted in [93]. Overall, we show that NPS multi-marker screening goes beyond current microfluidic cell-screening methods with its ability to determine surface-marker profiles and subsequently identify and distinguish different cell types and subpopulations. Furthermore, we verify our results by comparing to FCM. We showcase our platform's potential as an affordable, highly-sensitive, user-friendly technology for cancer detection in low-resource settings by screening leukemia patient samples, as there is no better example of the disparity of patient outcome between developed and undeveloped countries than this disease and its many subtypes. For example, the cure rate for acute lymphoblastic leukemia (ALL) in children in 2003 was reported to be ~80% in developed countries, but less than 10% in developing countries [123]. As another example, APL is a highly aggressive disease that accounts for 6-8% of all adult and 10% of all pediatric AML cases in the United States [124-126]. In Latin America, APL is the most frequent subtype of AML [102, 127]. Immediate diagnosis of APL and subsequent administration of all-*trans* retinoic acid (ATRA) are necessary to prevent the irreversible disease progression that leads to rapid death [124, 126]. In the United States, APL has an early death rate of 17.3% [126, 128-130]. In contrast, in Latin America, the induction mortality rate was, until recently, 32.1% with an overall mortality rate of 44.7% [102, 127]. With limited access to advanced diagnostic technologies in low-resource settings, the low-power, portable, and label-free technology we have developed using NPS could have high impact in these areas.

7. 2 Experimental Methods

7.2.1 Primary human bone marrow sample preparation

Primary bone marrow samples were obtained from patients with AML and were processed using a standard red-blood cell lysis protocol. Details on the minor sample preparation prior to testing is described in Chapter 9: Protocols.

7.2.2 Flow cytometry of cell lines

FCM details for the bone marrow samples can be found in the Chapter 9: Protocols.

7.2.3 Platform design

We screened previously frozen bone-marrow samples from three different AML patients to characterize blast populations. We employed a five-node device to measure the expression of CD13, HLA-DR, CD34, and CD45, as shown in Fig. 7.1. Samples, which had been treated with a standard red blood cell lysis protocol prior to freezing, were thawed, then diluted in RPMI 1640 (supplemented with 10% fetal bovine serum) media to a concentration of 10^6 cells/mL, and immediately injected into prepared node-devices.

Fig. 7.1: Node-pore antibody patterning schematic used for bone marrow testing. The antibody pattern configuration for the five-node-pore used to screen the AML patient bone-marrow samples included anti-CD13, anti-HLA-DR, anti-CD34, anti-CD45, and isotype controls. Two different isotype-controls, IgG1 and IgG2, were included because of the specific antibodies chosen.

7.2.4 Positive surface-marker expression cutoff determination using isotype control labeled devices

To establish the normalized transit-time threshold values, which we used to determine whether a blast cell is positive for a particular surface marker, we screened a sample of each patient sample in node-pores that had isotype-control patterned segments, as shown in Fig. 7.2. Because the anti-HLA-DR antibody used in these experiments had a different isotype control than that of all the other antibodies (IgG2 vs. IgG1), the node-pores consisted of two consecutive segments that were functionalized with one isotype control antibody and two segments functionalized with the other isotype control antibody, as shown in Fig. 7.2. We analyzed only those cells that were greater than 12 µm (as explained later) and normalized their transit times as follows,

$$\tau_{\text{norm, IgG1}} = \tau_{\text{IgG1 segment 1}} / \tau_{\text{IgG1 segment 2}} \qquad \text{Eq. (7.1)}$$

$$\tau_{\text{norm, IgG2}} = \tau_{\text{IgG2 segment 1}} / \tau_{\text{IgG2 segment 2}} \qquad \text{Eq. (7.2)}$$

For each patient sample, we determined the standard deviation of each normalized transit-time distribution, σ_{IgG1} and σ_{IgG2}, and as before, set the positive-expression threshold cutoff to be $1+2\sigma_{\text{isotype}}$, thereby taking into account the inherent variability in nonspecific interactions between the cells and functionalized isotype-control antibodies.

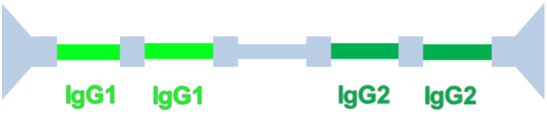

Fig. 7.2: Schematic of a four-node pore with two consecutive segments functionalized with IgG1 isotype-control antibody and two consecutive segments functionalized with IgG2 isotype-control antibody. The device dimensions were 25µm x 25 µm (H x W) with five 1150 µm long segments separated by four nodes, each 65 µm x 50 µm (W x L).

7. 3 Results

7.3.1 Positive surface-marker expression cutoff determination for AML patient bone-marrow samples

Normalized transit-time distributions are shown in Fig. 7.3, with threshold cutoff values for each patient sample denoted with a vertical dashed line. Threshold cutoff values were determined to be 1.0580, 1.0609, 1.0492 for IgG1, and 1.0514, 1.0460, 1.0467 for IgG2 for Patient 1, 2, and 3, respectively.

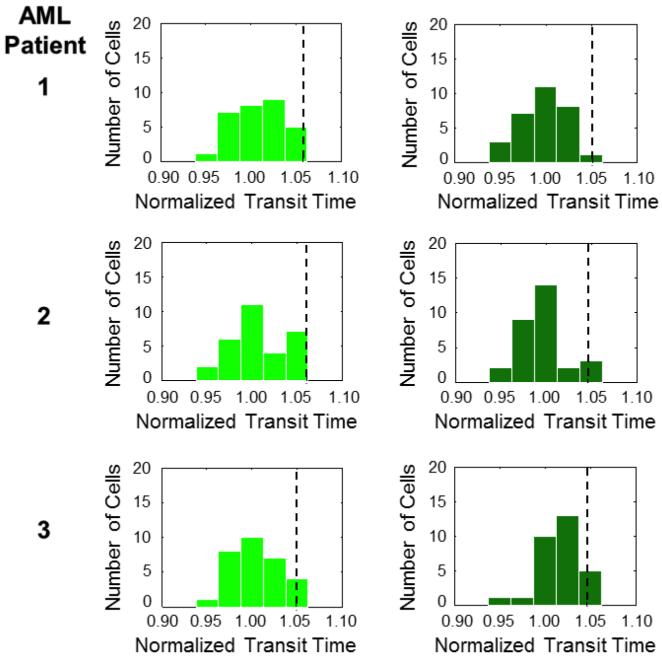

Fig. 7.3: Isotype-control transit-time cutoff determination. Normalized transit-time distributions for IgG1 (left) and IgG2 (right) for all three patient samples are shown, and the positive-expression cutoffs, corresponding to $1+2\sigma_{\text{isotype}}$, are indicated by the vertical dashed lines.

7.3.2 Screening Primary Human Bone Marrow Samples from Patients with AML

Some of the main criteria of interest in bone marrow samples for leukemia diagnosis and subtyping include the detection and characterization the blast cell populations. Blast cells are large, typically 12-20 µm [131] and have low expression of CD45. While FCM employs side-scatter (SS)/CD45 expression to identify the blast-cell population [132, 133], we used cell size and considered only those cells larger than 12 µm (dark purple in Fig. 7.4A). By using a cell size cutoff, we could also be including subpopulations such as promyelocytes (13-25 µm) [134], myelocytes (12-15 µm) [135], and histiocytes (15-25 µm) [131]. Larger-sized cells, e.g.

megakaryocytes (35-150 µm) [134], would not be included, as these cells are far larger than the employed node-pore channel cross sectional area (25 µm x 25 µm , H x) and would not have been able to enter into the node-pore. Using our size cutoff of >12 µm, we determined the blast-cell population to be 43%, 44%, and 34% for Patient 1, 2, and 3, respectively, which is in remarkable agreement with the FCM blast percentages of 46%, 36%, and 39% for the respective patients, as shown in Fig. 7.4B.

A

Flow Cytometry				
Patient	**Blasts**	**CD13**	**HLA-DR**	**CD34**
1	46	91	99	87
2	36	71	36	2
3	39	76	99	37

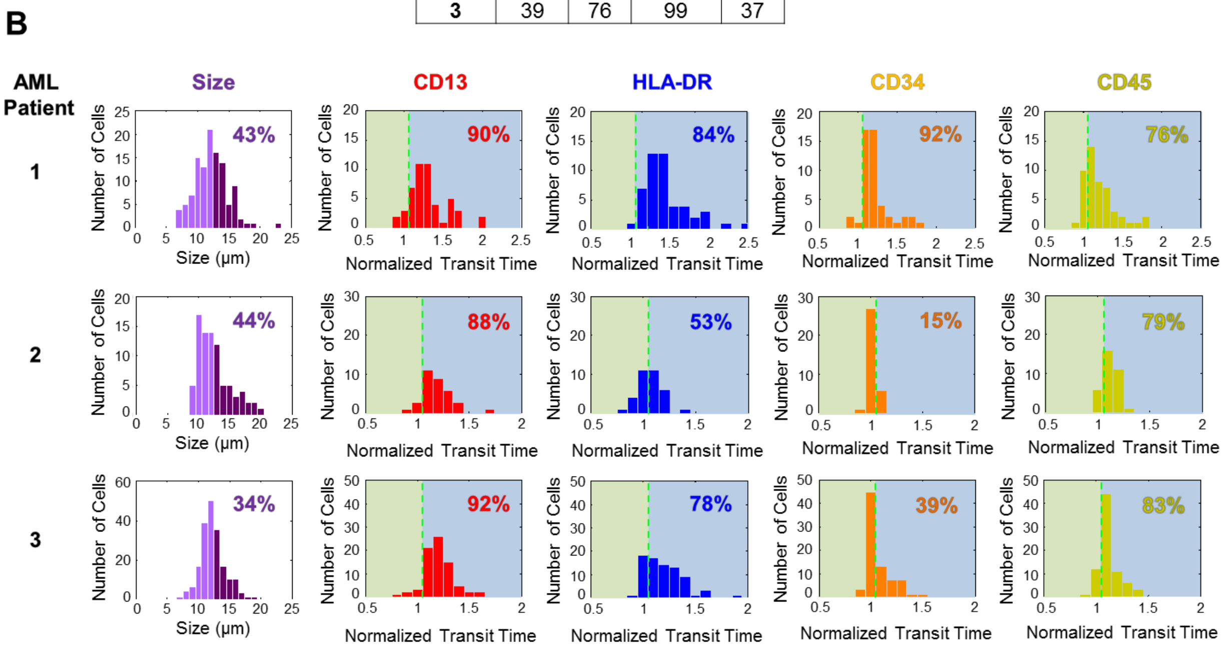

Fig. 7.4: FCM and NPS analysis summary of AML patient bone-marrow samples. (A) FCM analysis of the patient samples. FCM analyzed ~ 4000, 5000, and 9000 cells for Patient 1, 2, and 3, respectively. (B) NPS cell-size distribution (left) and surface-marker normalized transit-time distributions (right) for each patient sample. Cells greater than 12 µm (dark purple in the cell-size distribution) were considered to be blasts and the percentage of the blast population is as indicated.

As with the cultured leukemia cell lines, positive expression for a particular surface marker was determined by normalizing the transit time of a cell with respect to the corresponding isotype control. If $\tau_{norm} > 1 + 2\sigma_{isotype}$, the cell is positive for that surface marker. Each patient's normalized blast-cell transit-time distribution for each surface marker is shown in Fig. 7.4B. The dashed vertical green lines indicate the positive-expression cutoff. While all three patients showed a high percentage of cells that expressed CD13 and CD45, there was high variability in HLA-DR and CD34 expression. These results were consistent with our FCM data (Figs. 7.5, 7.6, and 7.7).

7.3.3 Flow cytometry results

Results for FCM for samples from Patient 1, 2, and 3 are shown in Figs. 7.5, 7.6, and 7.7, respectively.

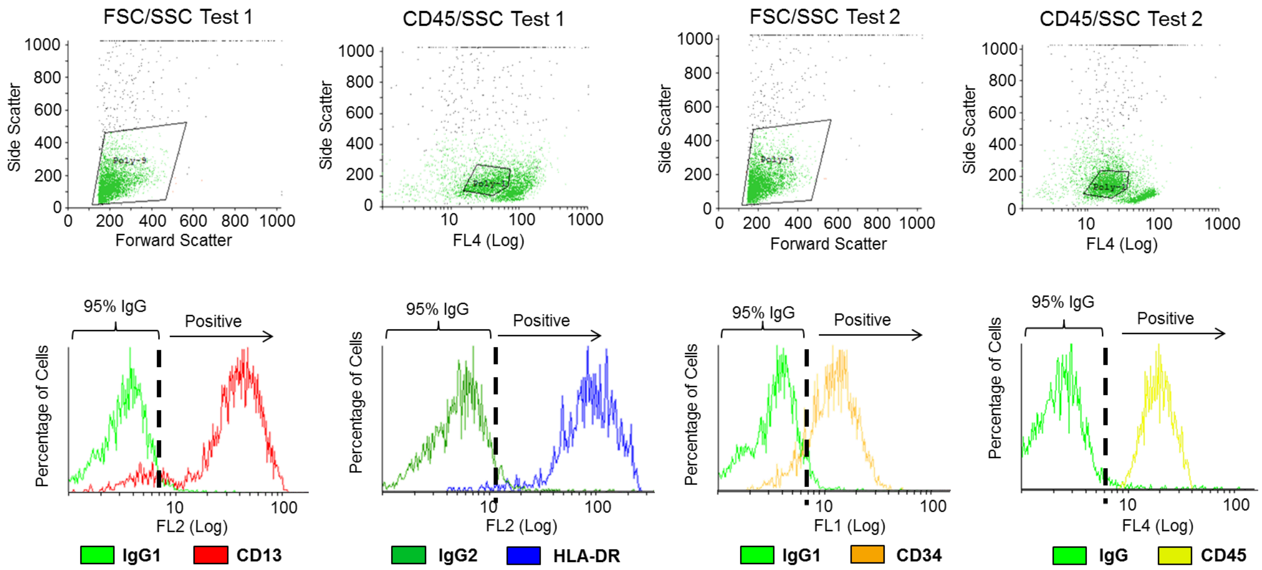

Fig. 7.5: FCM of AML Patient 1 bone-marrow sample. Two tests were performed, with each test involving staining with anti-CD34 antibody, anti-CD45 antibody, and either anti-CD13 or anti-HLA-DR antibody. Forward scatter/side scatter plots and CD45/side scatter plots are shown for both tests (top row). The CD45/side scatter plots were used to gate for the blast-cell population. Histograms showing fluorescence compared to isotype-control antibody staining are shown with vertical dashed lines indicating 95% of the control samples, which was used as a positive cutoff.

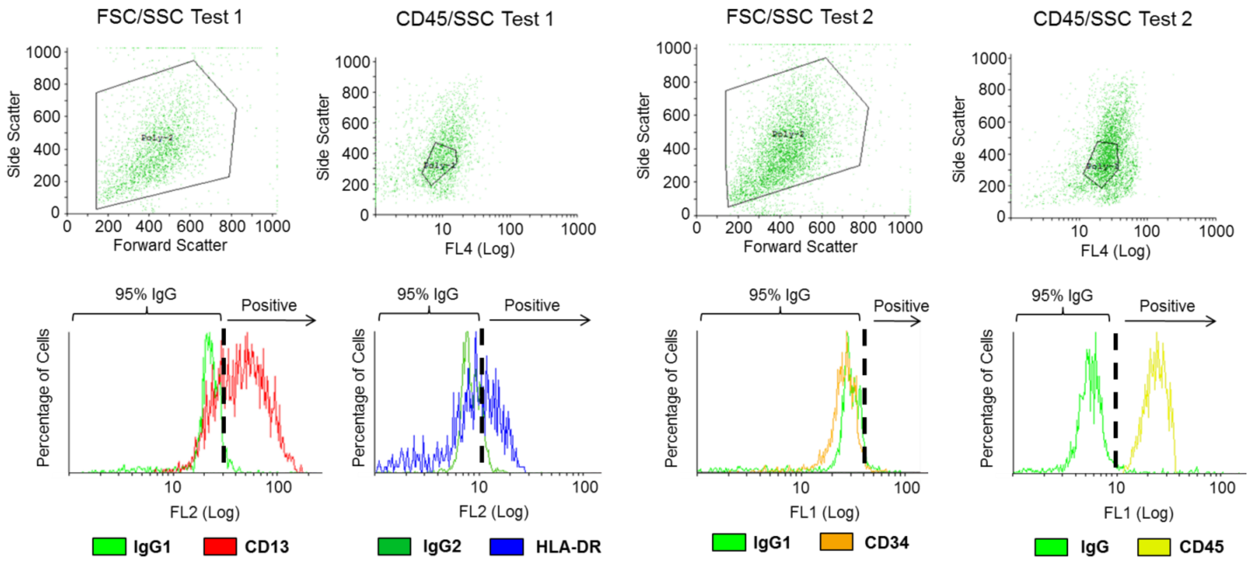

Fig. 7.6: FCM of AML Patient 2 bone-marrow sample. Two tests were performed with each test involving staining with anti-CD34 antibody, anti-CD45 antibody, and either anti-CD13 or anti-HLA-DR antibody. Forward scatter/side scatter plots and CD45/side scatter plots are shown for both tests (top row). The CD45/side scatter plots were used to gate for the blast cell population. Histograms showing fluorescence compared to isotype-control antibody staining are shown with vertical dashed lines indicating 95% of the control samples, which was used as a positive cutoff.

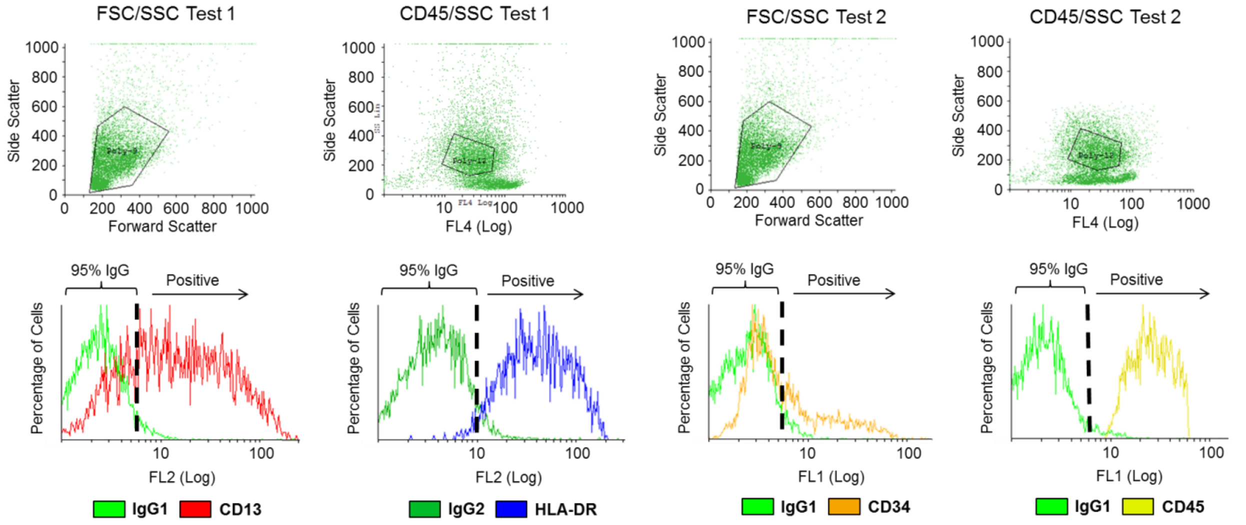

Fig. 7.7: FCM of AML Patient 3 bone-marrow sample. Two tests were performed with each involving staining with anti-CD34 antibody, anti-CD45 antibody, and either anti-CD13 or anti-HLA-DR antibody. Forward scatter/side scatter plots and CD45/side scatter plots both tests (top two rows). The CD45/side scatter plots were used to gate for the blast population. Histograms for both blast populations showing fluorescence compared to isotype-control antibody staining are shown with vertical dashed lines indicating 95% of the control samples, which was used as a positive cutoff.

7.3.4 Statistical analysis of patient bone marrow sample testing

As done with the cultured cell line screening (Chapter 6), we again employed a χ^2 test on the patient bone-marrow samples to determine whether there were any statistically significant differences between NPS and FCM results. Table 7.1 shows the χ^2 values of all three patient samples for each marker. By employing a χ^2 test with a p-value of 0.05 as we had done previously, we find that, with the exception of Patient 2's CD34 expression, there were no statistically significant differences between the results obtained with NPS and those of FCM. The large discrepancy between the two methods for Patient 2's CD34 expression is exaggerated due to the low expected levels of expression (2% in FCM). In general, however, differences between NPS and FCM could mainly be attributed to their different gating strategies, with NPS's size gating resulting in the potential inclusion of cells other than blasts.

Table 7.1. χ^2 test comparing NPS with FCM on AML patient samples.

Surface Antigen	**Patient 1 χ^2**	**Patient 2 χ^2**	**Patient 3 χ^2**
CD13	0.008	1.423	2.661
HLA-DR	1.163	2.711	3.456
CD34	0.132	27.445	0.080

7. 4 Discussion

NPS is an accurate, label-free, and simple method for screening cells for multiple markers, simultaneously. While the work we have highlighted utilized either a four or five-node-pore device to screen for markers, the device could have been easily expanded to include more nodes and thus screen many more markers (greater than ten) or include redundancy. Such screening would be especially important for distinguishing disease subtypes that have complex phenotypic profiles and require an extensive panel of markers for accurate diagnosis. In the experiments we performed, only one or two isotype controls were needed for all the antibodies utilized; however, one could include many more controls if necessary.

Ultimately, NPS could be a potentially valuable tool for diagnostic cancer screening in low-resource settings, and the ease of operation makes implementation of NPS in these areas entirely feasible. The node-pore is low-cost, disposable, and requires two 15-volt batteries as its power source. The device compactness and electronic circuitry make it possible to assemble a portable, handheld platform that could be suitable for point-of-care applications. For leukemia diagnosis in low-resource settings, administration of a standard red-blood cell lysis protocol to either a bone-marrow biopsy, as we have demonstrated, or a single draw of blood could be used for immediate screening in functionalized node-pore devices that had been prepared in advance and placed in a refrigerator (or freezer for long-term storage) until needed. Furthermore, only a small volume of sample would be needed for NPS. While the technique currently uses cell size as its gating strategy to identify the potential blast population, NPS could combine cell size with specific surface markers, beyond those that we utilized here, to determine specific subpopulations. As well, the cross-sectional area of the node-pore could be easily changed to include larger cells, such as megakaryocytes, for screening. Finally, higher accuracy could be achieved if redundancy of antibodies is included, as we showed when screening a mixture of cell lines. In the future, NPS could provide both the physician and patient a rapid and early pre-screening, complete with surface-marker profiles of a sample, with which then the patient could seek further testing or appropriate treatment at a major medical facility in a centralized hospital. Furthermore, the NPS platform could assist physicians in monitoring therapy and detecting minimal residual disease and remission states.

CHAPTER 8

Conclusions and Future Directions

In this thesis, we have described advancements to RPS that enhance the capabilities of this versatile technique and broaden its applicability. We have demonstrated screening of several different biological samples, including stem cells, HIV in human plasma, cultured leukemia cells, and leukemia patient bone marrow.

By screening stem cells from mice, we were able to show that RPS can be used with small samples with minute populations of cells. While we manually isolated satellite cells from their respective fibers and then injected them into our device for screening, the modular nature of our microfluidics platform allows for the incorporation of a series of gated microfluidic valves, reservoirs to introduce enzymes for cell disassociation from tissue, and mixers that ultimately would enable isolation and subsequent screening *in situ*. Such an *in situ* method and device could be generally applied to other stem-cell systems in which both sample and cells are rare.

Further, we have developed unique geometry pores that offer benefits for detection and characterization. The segmented structure of these node-pores allows us to determine when a cell passes through a given pore segment and also leads to a unique measurement signature as each cell transits through, which allows for identifying small particles in a sample without risks of clogging from much larger particles. NPS sensing for cell characterization requires minimal sample preparation because the devices are functionalized with antibodies (in contrast to systems where pre-processing steps are needed to bind antibodies directly to targets in the sample). NPS provides an unprecedented dynamic range and could be used for medical, environmental, and industrial applications, including screening bacterial and other viral populations, assessing water quality and determining contaminants, and monitoring protein aggregation in pharmaceutical processes.

We have presented an extremely robust, flexible, and powerful screening platform, and further work could be done to add further value to the platform in a number of ways. Throughput of our platform is limited because multiple particles transiting the pore at the same time complicates signal identification. More robust signal extraction algorithms could be developed to solve this challenge. We have shown testing using a single pore, but throughput could be greatly increased by using multiplexing strategies such as parallel-sensing arrays. Furthermore, integrating sorting functionality with NPS would provide a multi-marker screening and isolation platform that would allow for collecting rare cells for further analysis.

The multi-marker NPS substrate functionalization techniques outlined in this thesis do not optimally utilize antibody. Only a small subset of the antibody volume that is injected into the temporary channels is used to functionalize the region where the node-pore is placed. Further optimization and development for patterning these segments on the substrate would greatly drive down the cost of manufacturing by minimizing the volume of antibody needed. Moreover, a method of permanently bonding the PDMS mold while still incorporating multi-antibody patterning could be beneficial.

We have showcased the application of NPS within the context of cell-surface marker profiling and distinguishing leukemic cells and bone-marrow samples, but the versatility of the platform makes NPS broadly applicable for the screening of several disease markers, including those associated with other types of cancer. Isolation of sorted cells could be used for downstream analysis and subsequent determination of treatment for an individual patient (i.e. personalized medicine). NPS has great potential to be utilized as a label-free, multi-marker screening tool; the minimal sample preparation and sample volume required make the system a promising diagnostic platform for widespread global-health use.

CHAPTER 9

Protocols

9.1 Stem cell testing protocols

9.1.1 Functionalization of substrates

Glass substrates were cleaned in a 10:1:1 RCA solution heated to 80°C for 5 min, followed by a thorough rinse in DI water. To functionalize the glass substrate area between the electrodes with antibodies, a temporary PDMS microchannel, created with soft lithography, was aligned between the electrodes and hermetically (reversibly) sealed to the substrate. This microchannel served as a patterning guide and ensured that only the region between the electrodes was silanized. A solution of 1M sodium hydroxide (Fisher Scientific) was injected into the microchannel for 10 min. The solution was then removed from the microchannel, and the devices were heated to 150°C for 10 min. After cooling, a silane solution (2% N-3-triethoxysilypropyl-4-hydroxybutramide [Gelest] in 95% ethanol [Acros], 0.1% acetic acid [Fisher Scientific]) was injected into the microchannel and incubated for 4 hours. The glass substrate was rinsed with a stock solution of 95% ethanol and 0.1% acetic acid, DI water, and baked at 120°C for 2 hours. The prepared PDMS microchannel was subsequently aligned and bonded (via oxygen plasma and heat) to the substrate. The just-silanized region on the glass substrate was protected with a piece of PDMS during plasma treatment. After PDMS bonding, 10 μL of the cross-linker, Sulfo-EGS, (3 mg/mL, Pierce) was injected into the microchannel for 20 minutes. Protein G (1 mg/mL, Pierce) was subsequently injected into the microchannel and incubated for 2-5 hrs. After incubation, excess Protein G was washed away with PBS. Antibodies at a concentration of 0.2-0.25 mg/mL (depending on stock concentration from the supplier) were injected into the prepared microchannel and incubated overnight at 4°C. The microchannel was then flushed thoroughly with PBS, then media, and kept filled with media for cell screening.

9.1.2 Satellite cell preparation for notch receptor screening

Satellite cells were isolated from mouse muscle as described [41]. Briefly, muscle was dissected from the hind leg of 2-month old C57/black-6 mouse and incubated at 37°C in digestion medium (200 U/mL Collagenase type II (Sigma) in DMEM, buffered with 10 mM HEPES, pH 7) for 2 hours with gentle agitation. After digestion the muscle was washed with PBS two times and triturated with a flame-polished broken pasteur pipette in buffered media (DMEM with 10% serum, buffered with 10 mM HEPES, pH7) in a shallow dish until the fibers were liberated. The dish containing the fibers was tilted to pool the liquid with fibers away from muscle chunks. The fibers were then transferred to a conical tube with additional buffered media and allowed to settle for 10 minutes, then washed two more times in buffered media before enzymatic digestion to liberate satellite cells (1 U/ml Dispase (Gibco), 40 U/ml Collagenase type II (Sigma) in DMEM, buffered with 10 mM HEPES, pH 7, for 1 hour with moderate agitation). The remaining debris was removed by gentle sedimentation (1 min, 200 x g), followed by filtration with a 40-50 μm mesh, and then the satellite cells were sedimented by centrifugation. After screening, the cells were collected from the device and cultured in DMEM/F12 media with only 2 % horse serum so as not to further activate the cells. Cells from the original culture that were not screened with the microfluidic device were also plated overnight in 8-well plates coated with either anti-Notch1 antibody (Invitrogen, 0.2 mg/ml), which was a positive control for Notch activation, or the isotype control IgG_1 (Invitrogen, 0.2 mg/mL). Cells were fixed in ethanol and immunostained for activated Notch as described [136].

9.1.3 Staining for Sca-1 expression through immunofluorescence with microfluidic channel capture

Myofiber-associated satellite cells were isolated as published [41]. Cells were attached to matrigel-coated plates (2 µg/ml/cm^2) for 2 hours before immunostained for Sca-1 and Pax7. The cells were first live-stained for cell surface Sca-1 using Alexa 488 conjugated secondary antibodies (BD Biosciences), fixed in 4% paraformaldehyde, and washed and permeabilized before immunostaining for nuclear Pax7 (Developmental Studies Hybridoma Bank) as described [137]. Sca-1$^+$ cells captured in the anti-Sca-1 antibody channel were fixed in 4% paraformaldehyde, washed, and permeabilized before immunostaining for nuclear Myf5 (Santa Cruz Biotechnology).

9.2 Leukemia Cell Line Protocols

9.2.1 Cell culture of NB4, AP-1060, and NALM-1 cell lines

NB4 cells were cultured at 2 x 10^6 cells/mL in RPMI 1640 media supplemented with 10% Fetal Bovine Serum (FBS) and 1X penicillin/streptomycin and routinely passaged as described by Lanotte et al. [94]. AP-1060 cells were obtained from Dr. Scott Kogan, University of California-San Francisco, San Francisco, CA, USA. Cells were cultured at 1 x 10^6 cells/mL in 70% Iscove's MDM supplemented with 20% FBS, 1X penicillin/streptomycin, and 10% conditioned medium from A5637 cells (ATTC) cultured in RPMI 1640 supplemented with 10% FBS and 1 X penicillin/streptomycin. AP-1060 cells were routinely passaged as described by Sun et al. [95]. NALM-1 cells (ATCC) were cultured at 1 x 10^6 cells/mL in RPMI 1640 supplemented with 15% FBS and 1X penicillin/streptomycin and routinely passaged as described by Minowada et al. [96]. For the screening experiments described, NB4, AP-1060, and NALM-1 cells were sedimented and re-suspended at a concentration of ~1 x 10^6 cells/mL in their respective (fresh) media prior to being injected into the node-pore device. For mixed sample testing, the samples were re-suspended in a 1:1 mixture of each cell line media.

9.2.2 FCM preparation for NB4, AP-1060, and NALM-1 cell lines

Cells for FCM were prepared by first washing 10^6 cells/mL in PBS 1X by centrifugation at 300 g for 3 minutes and re-suspending in fresh PBS. The cells were then incubated with 4% formaldehyde for 15 minutes before being washed two more times with PBS and subsequently suspended in PBS with 1% bovine serum albumin (BSA, Sigma-Aldrich) and 0.1% sodium azide (Sigma-Aldrich). Cells were then incubated with primary antibody at 10 µg/ml for 3 hours. Samples were then washed three more times with PBS before being suspended in 1% BSA and 0.1% sodium azide with secondary antibody (Alexa Fluor 488 Goat Anti-Mouse IgG) at 2 µg/mL and stored for 90 minutes in the dark. After incubation, samples were washed three more times with PBS and finally suspended in PBS with 1% BSA and 0.1% sodium azide for FCM testing in an FC 500 Series machine (Beckman Coulter). Antibody details are found in Table A.2 in the Appendix.

9.3 Patient bone marrow sample protocols

9.3.1 Bone marrow sample preparation

Primary bone marrow samples were provided by Dr. Lucy Godley and were obtained from patients with AML after obtaining written informed consent to an IRB-approved protocol at The University of Chicago, which allows for the use of AML samples for future scientific research. Bone marrow samples were processed using a standard red-blood cell lysis protocol, frozen viably with 10% DMSO, and stored in liquid nitrogen. For screening, samples were thawed, suspended in pre-warmed RPMI 1640 supplemented with 10% FBS and 1X penicillin/streptomycin, and spun at 300 g for 3 min. Cells were then re-suspended in RPMI 1640 media supplemented with 10% FBS and immediately screened with NPS. All sample screening was performed under a University of California, Berkeley IRB-approved protocol.

9.3.2 FCM preparation of bone marrow samples

Bone marrow samples for FCM were prepared by first washing the cells in PBS (1X) by centrifugation at 300 g for 3 minutes and re-suspending in fresh PBS. Cells were then incubated with 4% formaldehyde for 15 minutes before being washed two more times with PBS and subsequently suspended in PBS with 1% bovine serum albumin (BSA, Sigma-Aldrich) and 0.1% sodium azide (Sigma-Aldrich). The cells were then incubated in the dark with primary antibody at 4 µg/ml for 30 minutes. After incubation, cells were washed three more times with PBS and finally suspended in PBS with 1% BSA and 0.1% sodium azide at 10^6 cells/mL for FCM testing in an FC 500 Series machine (Beckman Coulter). Antibody details are found in the Appendix.

Bibliography

1. Gregg, E.C. and K.D. Steidley, *Electrical Counting and Sizing of Mammalian Cells in Suspension.* Biophys J., 1965. 5(4): p. 393-405.

2. Kubitschek, H.E., *Electronic counting and sizing of bacteria.* Nature, 1958. 182(4630): p. 234-5.

3. Craine, K. and A.D. Waft, *Red cell volume distribution histograms for establishing the normal range using the Coulter plotter model J.* J Clin Pathol, 1967. 20(6): p. 913-5.

4. Carbonaro, A., et al., *Cell characterization using a protein-functionalized pore.* Lab on a Chip, 2008. 8(9): p. 1478-85.

5. Hirsch, J. and E. Gallian, *Methods for the determination of adipose cell size in man and animals.* J Lipid Res, 1968. 9(1): p. 110-9.

6. Bryan, A.K., et al., *Continuous and long-term volume measurements with a commercial Coulter counter.* PLoS One, 2012. 7(1): p. e29866.

7. Wu, Y.F., J.D. Benson, and M. Almasri, *Micromachined Coulter counter for dynamic impedance study of time sensitive cells.* Biomedical Microdevices, 2012. 14(4): p. 739-750.

8. DeBlois, R.W. and R.K. Wesley, *Sizes and concentrations of several type C oncornaviruses and bacteriophage T2 by the resistive-pulse technique.* J Virol, 1977. 23(2): p. 227-33.

9. Zhou, K., et al., *Characterization of hepatitis B virus capsids by resistive-pulse sensing.* J Am Chem Soc, 2011. 133(6): p. 1618-21.

10. Harms, Z.D., et al., *Nanofluidic devices with two pores in series for resistive-pulse sensing of single virus capsids.* Anal Chem, 2011. 83(24): p. 9573-8.

11. Deblois, R.W. and C.P. Bean, *Counting and Sizing of Submicron Particles by Resistive Pulse Technique.* Review of Scientific Instruments, 1970. 41(7): p. 909-&.

12. Gregg, E.C. and K.D. Steidley, *Electrical counting and sizing of mammalian cells in suspension.* Biophys J, 1965. 5(4): p. 393-405.

13. Saleh, O.A., *A Novel Resistive Pulse Sensor for Biological Measurements*, in *Physics* 2003, Princeton University: Princeton, NJ. p. 1-111.

14. Deblois, R.W., C.P. Bean, and R.K. Wesley, *Electrokinetic Measurements with Submicron Particles and Pores by Resistive Pulse Technique.* Journal of Colloid and Interface Science, 1977. 61: p. 323-335.

15. Smythe, W.R., *Flow around a Sphere in a Circular Tube.* Physics of Fluids, 1961. 4(6): p. 756-759.

16. Smythe, W.R., *Flow around a Spheroid in a Circular Tube.* Physics of Fluids, 1964. 7(5): p. 633-638.

17. Wanunu, M. and A. Meller, *Chemically modified solid-state nanopores.* Nano Lett, 2007. 7(6): p. 1580-5.

18. Carbonaro, A., et al., *Cell characterization using a protein-functionalized pore.* Lab Chip, 2008. 8(9): p. 1478-85.

19. Watkins, N.N., et al., *Microfluidic CD4+ and CD8+ T lymphocyte counters for point-of-care HIV diagnostics using whole blood.* Sci Transl Med, 2013. 5(214): p. 214ra170.

20. Zheng, X., et al., *Cell receptor and surface ligand density effects on dynamic states of adhering circulating tumor cells.* Lab Chip, 2011. 11(20): p. 3431-9.

21. Cheung, L.S.L., et al., *Adhesion dynamics of circulating tumor cells under shear flow in a bio-functionalized microchannel.* Journal of Micromechanics and Microengineering, 2011. 21(5).

22. Myung, J.H., et al., *Enhanced tumor cell isolation by a biomimetic combination of E-selectin and anti-EpCAM: implications for the effective separation of circulating tumor cells (CTCs).* Langmuir, 2010. 26(11): p. 8589-96.

23. Hammer, D.A. and D.A. Lauffenburger, *A Dynamical Model for Receptor-Mediated Cell-Adhesion to Surfaces in Viscous Shear-Flow.* Cell Biophysics, 1989. 14(2): p. 139-173.

24. cozens-roberts, *receptor-mediated adhesion phenomena.* 1990.

25. Balakrishnan, K. and L.L. Sohn, *Cell screening using resistive-pulse sensing*, in *Methods in Cell Biology*, P.M. Conn, Editor. 2012, Elsevier. p. 369-387.

26. Lu, B.S., M.R.; O'Kennedy, R., *Oriented immobilization of antibodies and its applications in immunoassays and imunosensors.* Analyst, 1996. 121(3).

27. Qin, M., et al., *Two methods for glass surface modification and their application in protein immobilization.* Colloids and Surfaces B-Biointerfaces, 2007. 60(2): p. 243-249.

28. Chapman, M.R., et al., *Sorting single satellite cells from individual myofibers reveals heterogeneity in cell-surface markers and myogenic capacity.* Integrative Biology, 2013.

29. Slack, J.M., *Origin of stem cells in organogenesis.* Science, 2008. 322(5907): p. 1498-501.

30. Shefer, G.Y.-R., Z., *Isolation and culture of skeletal muscle myofibers as a means to analyze satellite cells.* Methods in Molecular Biology, 2005. 290: p. 281-304.

31. Kuci, S., et al., *Adult Stem Cells as an Alternative Source of Multipotential (Pluripotential) Cells in Regenerative Medicine.* Current Stem Cell Research & Therapy, 2009. 4(2): p. 107-117.

32. Conboy, I.M., et al., *Notch-mediated restoration of regenerative potential to aged muscle.* Science, 2003. 302(5650): p. 1575-7.

33. Zammit, P.S., T.A. Partridge, and Z. Yablonka-Reuveni, *The skeletal muscle satellite cell: the stem cell that came in from the cold.* J Histochem Cytochem, 2006. 54(11): p. 1177-91.

34. Sherwood, R.I., et al., *Isolation of adult mouse myogenic progenitors: Functional heterogeneity of cells within and engrafting skeletal muscle.* Cell, 2004. 119(4): p. 543-554.

35. Tanaka, K.K., et al., *Syndecan-4-Expressing Muscle Progenitor Cells in the SP Engraft as Satellite Cells during Muscle Regeneration.* Cell Stem Cell, 2009. 4(3): p. 217-225.

36. Tarnok, A., H. Ulrich, and J. Bocsi, *Phenotypes of stem cells from diverse origin.* Cytometry A, 2010. 77(1): p. 6-10.

37. Chakkalakal, J.V., et al., *The aged niche disrupts muscle stem cell quiescence.* Nature, 2012. 490(7420): p. 355-60.

38. Cheung, T.H., et al., *Maintenance of muscle stem-cell quiescence by microRNA-489.* Nature, 2012. 482(7386): p. 524-8.

39. Rosenblatt, J.D., et al., *Culturing satellite cells from living single muscle fiber explants.* In Vitro Cell Dev Biol Anim, 1995. 31(10): p. 773-9.

40. Hanson, P., et al., *Enhanced green fluorescent protein targeted to the Sca-1 (Ly-6A) locus in transgenic mice results in efficient marking of hematopoietic stem cells in vivo.* Exp. Hematol., 2003. 31: p. 159-167.

41. Conboy, M.J. and I.M. Conboy, *Preparation of adult muscle fiber-associated stem/precursor cells.* Methods Mol Biol, 2010. 621: p. 149-63.

42. Rorabacher, D.B., *Statistical Treatment for Rejection of Deviant Values - Critical-Values of Dixon Q Parameter and Related Subrange Ratios at the 95-Percent Confidence Level.* Analytical Chemistry, 1991. 63(2): p. 139-146.

43. Dixon, W.J., *Analysis of Extreme Values.* Annals of Mathematical Statistics, 1950. 21(4): p. 488-506.

44. Dixon, W.J., *Ratios involving extreme values.* Ann. Math. Stat., 1951. 21(4): p. 488-506.

45. Benjamini, Y. and Y. Hochberg, *Controlling the false discovery rate: a practical and powerful approach to multiple testing.* Journal of the Royal Statistical Society, Series B (Methodological), 1995. 57(1): p. 289-300.

46. Mitchell, P.O., et al., *Sca-1 negatively regulates proliferation and differentiation of muscle cells.* Developmental Biology, 2005. 283: p. 240-252.

47. Moore, R. and F.S. Walsh, *The cell adhesion molecule M-cadherin is specifically expressed in developing and regenerating, but not denervated skeletal muscle.* Development, 1993. 117(4): p. 1409-20.

48. Irintchev, A., et al., *Expression pattern of M-cadherin in normal, denervated, and regenerating mouse muscles.* Dev Dyn, 1994. 199(4): p. 326-37.

49. Kaufmann, U., et al., *M-cadherin and its sisters in development of striated muscle.* Cell Tissue Res, 1999. 296(1): p. 191-8.

50. Dean, R.B. and W.J. Dixon, *Simplified Statistics for Small Numbers of Observations.* Analytical Chemistry, 1951. 23(4): p. 636-638.

51. Zammit, P.S., et al., *Muscle satellite cells adopt divergent fates: a mechanism for self-renewal?* J. Cell Biol., 2004. 166: p. 347-357.

52. Ono, Y., et al., *Muscle satellite cells are a functionally heterogeneous population in both somite-derived and branchiomeric muscles.* Dev. Biol., 2010. 337: p. 29-41.

53. Royer, C.L., et al., *Muscle-derived CD45-SCA-1+c-kit- progenitor cells give rise to skeletal muscle myotubes in vitro.* In Vitro Cell Dev Biol Anim, 2002. 38(9): p. 512-7.

54. Schulz, T.J., et al., *Identification of inducible brown adipocyte progenitors residing in skeletal muscle and white fat.* Proc Natl Acad Sci U S A, 2011. 108(1): p. 143-8.

55. Cerletti, M., et al., *Highly efficient, functional engraftment of skeletal muscle stem cells in dystrophic muscles.* Cell, 2008. 134(1): p. 37-47.

56. Conboy, I.M. and T.A. Rando, *The regulation of Notch signaling controls satellite cell activation and cell fate determination in postnatal myogenesis.* Dev Cell, 2002. 3(3): p. 397-409.

57. Biressi, S. and T.A. Rando, *Heterogeneity in the muscle satellite cell population.* Semin Cell Dev Biol, 2010. 21(8): p. 845-54.

58. Dimario, J.X., S.E. Fernyak, and F.E. Stockdale, *Myoblasts Transferred to the Limbs of Embryos Are Committed to Specific Fiber Fates.* Nature, 1993. 362(6416): p. 165-167.

59. Kalhovde, J.M., et al., *'Fast' and 'slow' muscle fibres in hindlimb muscles of adult rats regenerate from intrinsically different satellite cells.* Journal of Physiology-London, 2005. 562(3): p. 847-857.

60. Balakrishnan, K.R., et al., *Node-pore sensing: a robust, high-dynamic range method for detecting biological species.* Lab Chip, 2013. 13(7): p. 1302-7.

61. Wu, X., et al., *Microfluidic differential resistive pulse sensors.* Electrophoresis, 2008. 29(13): p. 2754-9.

62. Smeets, R.M.M., et al., *Noise in solid-state nanopores.* Proc Natl Acad Sci U S A, 2007. 105(2): p. 417-421.

63. Bezrukov, S.M., I. Vodyanoy, and V.A. Parsegian, *Counting Polymers Moving through a Single-Ion Channel.* Nature, 1994. 370(6487): p. 279-281.

64. Clarke, J., et al., *Continuous base identification for single-molecule nanopore DNA sequencing.* Nature Nanotechnology, 2009. 4(4): p. 265-270.

65. Rincon-Restrepo, M., et al., *Controlled Translocation of Individual DNA Molecules through Protein Nanopores with Engineered Molecular Brakes.* Nano Letters, 2011. 11(2): p. 746-750.

66. Kasianowicz, J.J., et al., *Characterization of individual polynucleotide molecules using a membrane channel.* Proc Natl Acad Sci U S A, 1996. 93(24): p. 13770-3.

67. Gu, L.Q., S. Cheley, and H. Bayley, *Capture of a single molecule in a nanocavity.* Science, 2001. 291: p. 636-40.

68. Bayley, H. and P.S. Cremer, *Stochastic sensors inspired by biology.* Nature, 2001. 413(6852): p. 226-30.

69. Wang, H.Y., et al., *Nanopore analysis of beta-amyloid peptide aggregation transition induced by small molecules.* Anal Chem, 2011. 83(5): p. 1746-52.

70. Ying, Y.L., et al., *Enhanced translocation of poly(dt)45 through an alpha-hemolysin nanopore by binding with antibody.* Chem Commun (Camb), 2011. 47(20): p. 5690-2.

71. Wang, Y., et al., *Nanopore-based detection of circulating microRNAs in lung cancer patients.* Nat Nanotechnol, 2011. 6(10): p. 668-74.

72. Hall, A.R., et al., *Hybrid pore formation by directed insertion of alpha-haemolysin into solid-state nanopores.* Nature Nanotechnology, 2010. 5(12): p. 874-877.

73. Xie, P., et al., *Local electrical potential detection of DNA by nanowire-nanopore sensors.* Nat Nanotechnol, 2012. 7(2): p. 119-25.

74. Li, J., et al., *Ion-beam sculpting at nanometre length scales.* Nature, 2001. 412: p. 166-169.

75. Wanunu, M., J. Sutin, and A. Meller, *DNA Profiling Using Solid-State Nanopores: Detection of DNA-Binding Molecules.* Nano Letters, 2009. 9(10): p. 3498-3502.

76. Franke, T., et al., *Surface acoustic wave actuated cell sorting (SAWACS).* Lab Chip, 2010. 10(6): p. 789-94.

77. Wanunu, M., et al., *Rapid electronic detection of probe-specific microRNAs using thin nanopore sensors.* Nature Nanotechnology, 2010. 5: p. 807-814.

78. Sun, L. and R.M. Crooks, *Single carbon nanotube membranes: A well-defined model for studying mass transport through nanoporous materials.* Journal of the American Chemical Society, 2000. 122(49): p. 12340-12345.

79. Rodriguez, A.T., et al., *Nanoporous carbon nanotubes synthesized through confined hydrogen-bonding self-assembly.* Journal of the American Chemical Society, 2006. 128(29): p. 9276-9277.

80. Bayley, H. and C.R. Martin, *Resistive-Pulse Sensing-From Microbes to Molecules.* Chemical Reviews, 2000. 100(7): p. 2575-2594.

81. Kwok, S., et al., *Identification of human immunodeficiency virus sequences by using in vitro enzymatic amplification and oligomer cleavage detection.* J Virol, 1987. 61(5): p. 1690-4.

82. Comandini, U.V., et al., *Quantification of HIV-1 proviral DNA from peripheral blood mononuclear cells using a high throughput four-competitor competitive PCR.* J Virol Methods, 1997. 69(1-2): p. 171-80.

83. Simmonds, P., et al., *Human Immunodeficiency Virus-Infected Individuals Contain Provirus in Small Numbers of Peripheral Mononuclear-Cells and at Low Copy Numbers.* Journal of Virology, 1990. 64(2): p. 864-872.

84. Bell, J. and L. Ratner, *Specificity of polymerase chain amplification reactions for human immunodeficiency virus type 1 DNA sequences.* AIDS Res Hum Retroviruses, 1989. 5(1): p. 87-95.

85. Hart, C., et al., *Direct detection of HIV RNA expression in seropositive subjects.* Lancet, 1988. 2(8611): p. 596-9.

86. Briggs, J.A., et al., *Structural organization of authentic, mature HIV-1 virions and cores.* EMBO J, 2003. 22(7): p. 1707-15.

87. Gentile, M., et al., *Determination of the Size of Hiv Using Adenovirus Type-2 as an Internal Length Marker.* Journal of Virological Methods, 1994. 48(1): p. 43-52.

88. Saleh, O.A. and L.L. Sohn, *Quantitative sensing of nanoscale colloids using a microchip Coulter counter.* Review of Scientific Instruments, 2001. 72(12): p. 4449-4451.

89. Saleh, O.A. and L.L. Sohn, *Direct detection of antibody-antigen binding using an on-chip artificial pore.* Proc Natl Acad Sci U S A, 2003. 100(3): p. 820-4.

90. Saleh, O.A. and L.L. Sohn, *An artificial nanopore for molecular sensing.* Nano Letters, 2003. 3(1): p. 37-38.

91. Carbonaro, A. and L.L. Sohn, *A resistive-pulse sensor chip for multianalyte immunoassays.* Lab on a Chip, 2005. 5(10): p. 1155-1160.

92. Zhe, J., et al., *A micromachined high throughput Coulter counter for bioparticle detection and counting.* Journal of Micromechanics and Microengineering, 2007. 17(2): p. 304-313.

93. Balakrishnan, K.R.W., J. C.; Hwang, R.; Hack, J. H.; Godley, L. A.; Sohn, L. L., *Node-pore sensing enables surface-marker profiling of single leukemic cells.* In submission, 2014.

94. Lanotte, M., et al., *NB4, a maturation inducible cell line with t(15;17) marker isolated from a human acute promyelocytic leukemia (M3).* Blood, 1991. 77(5): p. 1080-6.

95. Sun, Y., et al., *Acute promyelocytic leukemia cell line AP-1060 established as a cytokine-dependent culture from a patient clinically resistant to all-trans retinoic acid and arsenic trioxide.* Leukemia, 2004. 18(7): p. 1258-69.

96. Minowada, J., et al., *A non-T, non-B human leukemia cell line (NALM-1): establishment of the cell line and presence of leukemia-associated antigens.* J Natl Cancer Inst, 1977. 59(1): p. 83-7.

97. Boss, M.A., et al., *Differentiation-linked expression of cell surface markers on HL-60 leukemic cells.* Blood, 1980. 56(5): p. 910-6.

98. Launiere, C., et al., *Channel Surface Patterning of Alternating Biomimetic Protein Combinations for Enhanced Microfluidic Tumor Cell Isolation.* Analytical Chemistry, 2012. 84(9): p. 4022-4028.

99. Jabart, E.R., S.; Lieu, C.; Hack, J.; Conboy, I.; Sohn, L. L., *A microfluidic method for the selection of undifferentiated human embryonic stem cells and in situ analysis.* submitted.

100. Li, P., Y. Gao, and D. Pappas, *Multiparameter cell affinity chromatography: separation and analysis in a single microfluidic channel.* Anal Chem, 2012. 84(19): p. 8140-8.

101. Chapman, M.R. and L.L. Sohn, *Label-free resistive-pulse cytometry.* Methods Cell Biol, 2011. 102: p. 127-57.

102. Rego, E.M., et al., *Improving acute promyelocytic leukemia (APL) outcome in developing countries through networking, results of the International Consortium on APL.* Blood, 2013. 121(11): p. 1935-43.

103. Wallace, T.A., D.N. Martin, and S. Ambs, *Interactions among genes, tumor biology and the environment in cancer health disparities: examining the evidence on a national and global scale.* Carcinogenesis, 2011. 32(8): p. 1107-21.

104. Kanavos, P., et al., *The economics of blood: gift of life or a commodity?* Int J Technol Assess Health Care, 2006. 22(3): p. 338-43.

105. Organization, W.H., *Medical Devices: Managing the Mismatch: An Outcome of the Priority Medical Devices Project*, ed. W.H. Organization. 2010, Geneva, Switzerland: WHO Press.

106. Yager, P., G.J. Domingo, and J. Gerdes, *Point-of-care diagnostics for global health.* Annu Rev Biomed Eng, 2008. 10: p. 107-44.

107. Chin, C.D., V. Linder, and S.K. Sia, *Lab-on-a-chip devices for global health: past studies and future opportunities.* Lab Chip, 2007. 7(1): p. 41-57.

108. Cho, S.H., et al., *Mammalian Cell Sorting using muFACS.* Conf Lasers Electro Optics, 2010. 2010: p. CTuD1.

109. Su, H.W., J.L. Prieto, and J. Voldman, *Rapid dielectrophoretic characterization of single cells using the dielectrophoretic spring.* Lab Chip, 2013. 13(20): p. 4109-17.

110. Xu, Y., et al., *Aptamer-based microfluidic device for enrichment, sorting, and detection of multiple cancer cells.* Anal Chem, 2009. 81(17): p. 7436-42.

111. Dharmasiri, U., et al., *Highly efficient capture and enumeration of low abundance prostate cancer cells using prostate-specific membrane antigen aptamers immobilized to a polymeric microfluidic device.* Electrophoresis, 2009. 30(18): p. 3289-300.

112. Phillips, J.A., et al., *Enrichment of cancer cells using aptamers immobilized on a microfluidic channel.* Anal Chem, 2009. 81(3): p. 1033-9.

113. Du, Z., et al., *Microfluidic-based diagnostics for cervical cancer cells.* Biosens Bioelectron, 2006. 21(10): p. 1991-5.

114. Nagrath, S., et al., *Isolation of rare circulating tumour cells in cancer patients by microchip technology.* Nature, 2007. 450(7173): p. 1235-9.

115. Ozkumur, E., et al., *Inertial focusing for tumor antigen-dependent and -independent sorting of rare circulating tumor cells.* Sci Transl Med, 2013. 5(179): p. 179ra47.

116. Stott, S.L., et al., *Isolation and characterization of circulating tumor cells from patients with localized and metastatic prostate cancer.* Sci Transl Med, 2010. 2(25): p. 25ra23.

117. Du, Z., et al., *Recognition and capture of breast cancer cells using an antibody-based platform in a microelectromechanical systems device.* Biomed Microdevices, 2007. 9(1): p. 35-42.

118. Weng, X.Q., et al., *Prognostic significance of monitoring leukemia-associated immunophenotypes by eight-color flow cytometry in adult B-acute lymphoblastic leukemia.* Blood Cancer J, 2013. 3: p. e133.

119. Peters, J.M. and M.Q. Ansari, *Multiparameter flow cytometry in the diagnosis and management of acute leukemia.* Arch Pathol Lab Med, 2011. 135(1): p. 44-54.

120. Hristozova, T., et al., *A simple multicolor flow cytometry protocol for detection and molecular characterization of circulating tumor cells in epithelial cancers.* Cytometry A, 2012. 81(6): p. 489-95.

121. Glynn, M.T., D.J. Kinahan, and J. Ducree, *CD4 counting technologies for HIV therapy monitoring in resource-poor settings--state-of-the-art and emerging microtechnologies.* Lab Chip, 2013. 13(14): p. 2731-48.

122. Richards-Kortum, R. and M. Oden, *Engineering. Devices for low-resource health care.* Science, 2013. 342(6162): p. 1055-7.

123. Pui, C.H. and R.C. Ribeiro, *International collaboration on childhood leukemia.* Int J Hematol, 2003. 78(5): p. 383-9.

124. Dong, H.Y., et al., *Flow cytometry rapidly identifies all acute promyelocytic leukemias with high specificity independent of underlying cytogenetic abnormalities.* Am J Clin Pathol, 2011. 135(1): p. 76-84.

125. Maule, M.M., et al., *High incidence of acute promyelocytic leukemia in children in northwest Italy, 1980-2003: a report from the Childhood Cancer Registry of Piedmont.* Leukemia, 2008. 22(2): p. 439-41.

126. Tallman, M.S.A., J. K., *How I treat acute promyelocytic leukemia.* Blood, 2009. 114(25): p. 5126-5135.

127. Rego, E.M. and R.H. Jacomo, *Epidemiology and treatment of acute promyelocytic leukemia in latin america.* Mediterr J Hematol Infect Dis, 2011. 3(1): p. e2011049.

128. Tallman, M.S., et al., *All-trans-retinoic acid in acute promyelocytic leukemia.* N Engl J Med, 1997. 337(15): p. 1021-8.

129. Park, J.H., et al., *Early death rate in acute promyelocytic leukemia remains high despite all-trans retinoic acid.* Blood, 2011. 118(5): p. 1248-54.

130. McClellan, J.S., et al., *Treatment advances have not improved the early death rate in acute promyelocytic leukemia.* Haematologica, 2012. 97(1): p. 133-6.

131. Loffler, H.R., J.; Haferlach, T.; Begemann, H., *Atlas of Clinical Hematology*, 2005, Springer Science & Business Media: Germany.

132. Brahimi, M., et al., *The Use of CD45/SSC Dot Plots in the Classification of Acute Leukemias.* J Hematol Thromb Dis, 2014. 2(2).

133. Lacombe, F., et al., *Flow cytometry CD45 gating for immunophenotyping of acute myeloid leukemia.* Leukemia, 1997. 11(11): p. 1878-86.

134. Handin, R.I.L., S. E.; Stossel, T. P., *Blood: Principles and Practice of Hematology*. Vol. 1. 2003, Philadelphia, PA 19106 USA: Lippincott Williams and Wilkins. 2304.

135. Henrikson, R.C.M., J. E., *NMS Histiology*. Vol. 518. 1997, Baltimore, USA: Lippincott Williams & Wilkins.

136. Conboy, M.J., et al., *Immuno-analysis and FACS sorting of adult muscle fiber-associated stem/precursor cells.* Methods Mol Biol. 621: p. 165-73.

137. Conboy, M.J., et al., *Immuno-analysis and FACS sorting of adult muscle fiber-associated stem/precursor cells.* Methods Mol Biol, 2010. 621: p. 165-73.

Appendix

Table A.1. Antibody details for stem cell testing.

Cell-Surface Marker (reactivity)	Antibody	Control Antibody	Source
Sca-1 (mouse)	Anti-Sca-1 (Ly-6A/E) 108102 (0.5 mg/mL)	Rat IgG$_{2a}$, κ (0.5 mg/mL)	Biolegend
CXCR4 (human/mouse/rat)	Anti-CD184 (CXCR4) ab2074 (1 mg/mL)	Rabbit polyclonal IgG (10 mg/mL)	Abcam
M-Cadherin (mouse)	Anti-M-Cadherin (12G4) ab78090 (1 mg/mL)	Mouse monoclonal IgG$_1$ κ (10 mg/ml)	Abcam
β1-Integrin (mouse/rat)	Anti-CD29 (β1-integrin) 102202 (0.5 mg/mL)	Armenian Hamster IgG (0.5 mg/mL)	Biolegend
Notch (mouse/rat)	Anti-Notch1 (8G10) sc-32756 (0.2 mg/mL)	Syrian hamster IgG (0.2 mg/mL)	Santa Cruz Biotechnology
Syndecan-4 (rabbit)	Anti-Syndecan-4 Ab24511 (0.5 mg/mL)	Rabbit polyclonal IgG (10 mg/ML)	Abcam

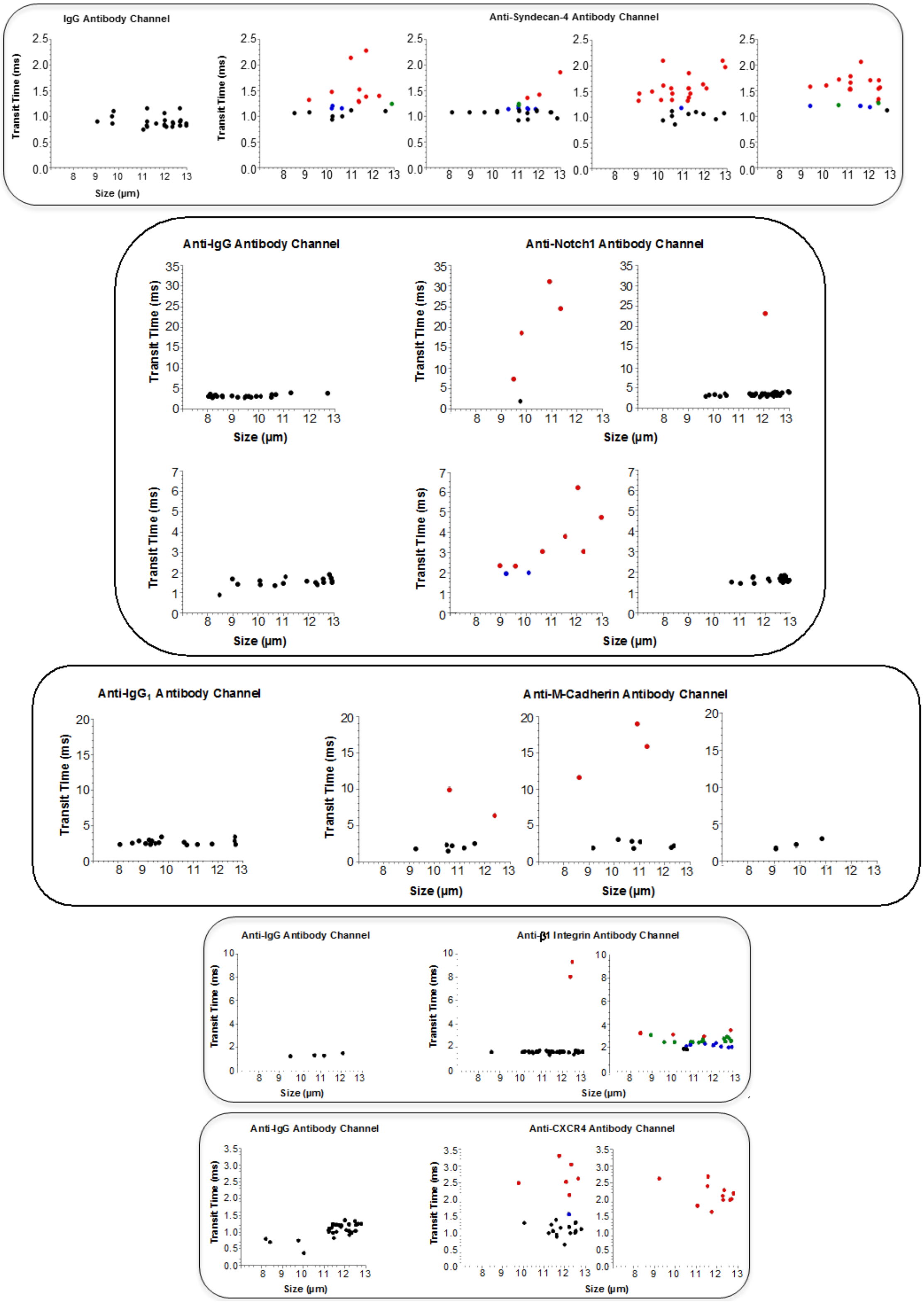

Fig. A.1: Screening analysis of satellite cells freshly derived from single muscle fibers. Transit times of freshly isolated satellite cells for different experiments. Syndecan-4⁺, Notch-1⁺ , M-cadherin⁺ , β1-Integrin⁺, and CXCR4⁺ cells were identified by statistically assessing whether a particular cell had an outlying slow transit time as compared to those cells passing through the isotype control microchannel (p-values were calculated). Under different p-value cutoffs, cells can be considered as having a high expression (red), medium expression (green), low expression (blue), or no expression (black). Each experiment consisted of cells collected from three single muscle fibers and screened with a different anti-Syndecan-4 antibody microchannel. Based on an FDR analysis, cells were determined to have high (red), medium (green), low (blue), or no (black) Syndecan-4 expression. [28]

Table A.2. Antibody details for FCM and NPS of NB4 and AP-1060 cell lines.

Antibody (Abcam)	**Clone**	**Stock Concentration**	**Flow Cytometry Concentration**	**Node-pore Substrate Concentration**
Anti-CD13	WM15	1 mg/mL	10 µg/mL	1 mg/mL
Anti-CD14	2Q1233	1 mg/mL	10 µg/mL	1 mg/mL
Anti-CD15	4E10	1 mg/mL	10 µg/mL	1 mg/mL
Anti-CD33	WM53	1 mg/mL	10 µg/mL	1 mg/mL
Anti-HLA DR	TAL 1B5	1 mg/mL	10 µg/mL	1 mg/mL
Mouse IgG1 Monoclonal	NCG01	1 mg/mL	10 µg/mL	1 mg/mL
Goat Anti-Mouse IgG H&L (Alexa Fluor 488)	N/A	2 mg/mL	2 µg/mL	N/A

Table A.3. Antibody details for FCM and NPS of AML patient samples.

Antibody (Biolegend)	Clone	Stock Concentration	Flow Cytometry Concentration	Node-pore Substrate Concentration
Anti-CD13	WM15	0.5 mg/mL	N/A	0.5 mg/mL
Anti-HLA DR	L243	0.5 mg/mL	N/A	0.5 mg/mL
Anti-CD34	581	0.5 mg/mL	N/A	0.5 mg/mL
Anti-CD45	HI30	0.5 mg/mL	N/A	0.5 mg/mL
Mouse IgG1, κ	MOPC-21	0.5 mg/mL	N/A	0.5 mg/mL
Mouse IgG2a, κ	MOPC-173	0.5 mg/mL	N/A	0.5 mg/mL
PE Anti-CD13	WM15	0.2 mg/mL	4 µg/mL	N/A
PE Anti-HLA DR	L243	0.02 mg/mL	4 µg/mL	N/A
Alexa Fluor 488 Anti-CD34	581	0.2 mg/mL	4 µg/mL	N/A
PerCP Anti-CD45	HI30	0.2 mg/mL	4 µg/mL	N/A
PE Mouse IgG1, κ	MOPC-21	0.2 mg/mL	4 µg/mL	N/A
PerCP Mouse IgG1, κ	MOPC-21	0.2 mg/mL	4 µg/mL	N/A
Alexa Fluor 488 Mouse IgG1, κ	MOPC-21	0.2 mg/mL	4 µg/mL	N/A
PE Mouse IgG2a, κ	MOPC-173	0.2 mg/mL	4 µg/mL	N/A